Reduced Order Modeling with Variable Spatial Fidelity for the Linear and Nonlinear Dynamics of Multi-Bay Structures

by

Yuting Wang

A Dissertation Presented in Partial Fulfillment
of the Requirements for the Degree
Doctor of Philosophy

Approved March 2017 by the
Graduate Supervisory Committee:

Marc Mignolet, Chair
Hanqing Jiang
Yongming Liu
Jay Oswald
Subramaniam Rajan
Stephen Spottswood

ARIZONA STATE UNIVERSITY

May 2017

ABSTRACT

This investigation develops small-size reduced order models (ROMs) that provide an accurate prediction of the response of only part of a structure, referred to as component-centric ROMs. Four strategies to construct such ROMs are presented, the first two of which are based on the Craig-Bampton Method and start with a set of modes for the component of interest (the β component). The response in the rest of the structure (the α component) induced by these modes is then determined and optimally represented by applying a Proper Orthogonal Decomposition strategy using Singular Value Decomposition. These first two methods are effectively basis reductions techniques of the CB basis. An approach based on the "Global - Local" Method generates the "global" modes by "averaging" the mass property over α and β comp., respectively (to extract a "coarse" model of α and β) and the "local" modes orthogonal to the "global" modes to add back necessary "information" for β. The last approach adopts as basis for the entire structure its linear modes which are dominant in the β component response. Then, the contributions of other modes in this part of the structure are approximated in terms of those of the dominant modes with close natural frequencies and similar mode shapes in the β component. In this manner, the non-dominant modal contributions are "lumped" onto the dominant ones, to reduce the number of modes for a prescribed accuracy. The four approaches are critically assessed on the structural finite element model of a 9-bay panel with the modal lumping-based method leading to the smallest sized ROMs. Therefore, it is extended to the nonlinear geometric situation and first recast as a rotation of the modal basis to achieve unobservable modes. In the linear case, these modes completely disappear from the formulation owing to orthogonality. In the nonlinear case, however, the generalized coordinates of these modes are still present in

the nonlinear terms of the observable modes. A closure-type algorithm is then proposed to eliminate the unobserved generalized coordinates. This approach, its accuracy and computational savings, was demonstrated on a simple beam model and the 9-bay panel model.

ACKNOWLEDGMENTS

I would like to express my sincere gratitude to my advisor, Dr. Mignolet, for the continuous support throughout my Ph.D.' program, for his patience, motivation, enthusiasm, immense knowledge and the opportunity to work in the group. I would like to thank Dr. Jiang, Dr. Liu, Dr. Oswald, Dr. Rajan and Dr. Spottswood, for serving on my committee.

I gratefully acknowledge the support of this work by the AFRL-University Collaborative Center in Structural Sciences (Cooperative Agreement FA8650-13-2-2347), with Dr. Benjamin Smarslok as program manager. In addition, I wish to express my appreciation to Dr. S.A. Rizzi and Dr. A. Przekop for the use of the 9-bay finite element model. Finally, I would like to thank Dr. R.A. Perez for generating some of the data on Fig. 63.

Last but not the least, I would like to thank my parents and my fellow mates for their support.

TABLE OF CONTENTS

Page

LIST OF TABLES vi

LIST OF FIGURES vii

CHAPTER

1 INTRODUCTION 1

1.1 Context and Motivation 1

1.2 Objective 6

1.3 Overview 6

2 BACKGROUND LITERATURE 9

2.1 Introduction 9

2.2 Linear Reduced Order Models 9

2.3 Geometric Nonlinear Reduced Order Models 11

2.4 Identification of ROM Parameters 12

2.5 ROM Basis Selection 14

2.6 Component Mode Synthesis 17

3 VALIDATION MODELS 19

3.1 A Middle Complexity Multi-Bay Structure 19

3.2 Nonlinear ROM Construction for the Multi-Bay Structure 21

3.3 A Simple Clamped-Clamped Beam Supported by Springs 50

3.4 Nonlinear ROM Construction for the Beam 51

3.5 Comparison of Different FE models with the ROM for the Beam 54

4 LINEAR COMPONENT-CENTRIC ROM 57

4.1 Craig-Bampton Based Approaches 57

4.1.1 ROMs Based on β-Fixed Interface and α-POD Modes 61

CHAPTER Page

4.1.2 ROMs Based on β-POD and α-POD Modes 65
4.2 "Global-Local" Based Method 68
4.3 Linear Modes Based, Modal Lumping Approach 73
4.3.1 Linear Modal Selection 74
4.3.2 Linear Modal Lumping 76
4.3.3 Linear Modal Lumping with Optimization 81
4.3.4 Robustness Assessment 91
4.3.5 Computational Benefits 93
4.4 Validation on the Beam Model 94
4.5 Validation on the Multi-Bay Structure with Identical Bays 96
5 NONLINEAR COMPONENT-CENTRIC ROM 98
5.1 Extension of Modal Lumping Method 98
5.1.1 Another Aspect of Modal Lumping: Modal Rotation 98
5.1.2 A "Closure" Type Scheme 100
5.2 Validation on the Beam Model 101
5.3 Validation on the Multi-Bay Structure 108
5.4 Computational Benefits 129
6 SUMMARY 131
REFERENCES 134

LIST OF TABLES

Table Page

1. Natural Frequencies of the 9-bay Panel (Hz) 21

2. Natural Frequencies of the Beam (Hz) 21

3. Selected Mode Numbers (by Decreasing Order of Importance) and Corresponding Natural Frequencies (Hz) for Bay 4, Recursive Algorithm 75

4. Selected Mode Numbers (by Decreasing Order of Importance) and Corresponding Natural Frequencies (Hz) for Bay 4, Predicted from Eq. (60) 76

5. Mean Representation Errors (in) of the Three Modal Lumping Approaches 90

6. Computational Cost Estimates for Linear ROMs of the Various Bays 94

7. Comparison of Modal Reduction for the Multi-Bay Structures 97

8. Coefficients of the Linear Relation of Eq. (85), for Bay 1 109

9. Computational Cost Estimates for Nonlinear Geometric ROMs of the Various Bays 130

LIST OF FIGURES

Figure Page

1. Finite Element Model of the 9-bay Fuselage Sidewall Panel, (a) Isometric View, (B) Top View From [23] 20

2. Magnitudes of the Frequency Responses at the Middle Point of Bay 4, Transverse Displacement..... 21

3. Normalized Mean Modal Projections on a Sample of "Snapshots".....22

4. Power Spectral Densities of the Transverse Responses of Panel 1 Center Obtained with Nastran SOL400 (Red), the 74-mode Full ROM (Black) for OASPL of 136dB 23

5. Power Spectral Densities of the In-plane (T1) Responses of Panel 1 Center Obtained with Nastran SOL400 (Red), the 74-mode Full ROM (Black) for OASPL of 136dB ...24

6. Power Spectral Densities of the In-plane (T2) Responses of Panel 1 Center Obtained with Nastran SOL400 (Red), the 74-mode Full ROM (Black) for OASPL of 136dB ...24

7. Power Spectral Densities of the Transverse Responses of Panel 2 Center Obtained with Nastran SOL400 (Red), the 74-mode Full ROM (Black) for OASPL of 136dB 25

8. Power Spectral Densities of the In-plane (T1) Responses of Panel 2 Center Obtained with Nastran SOL400 (Red), the 74-mode Full ROM (Black) for OASPL of 136dB ...25

9. Power Spectral Densities of the In-plane (T2) Responses of Panel 2 Center Obtained with Nastran SOL400 (Red), the 74-mode Full ROM (Black) for OASPL of 136dB ...26

10. Power Spectral Densities of the Transverse Responses of Panel 3 Center Obtained with Nastran SOL400 (Red), the 74-mode Full ROM (Black) for OASPL of 136dB ...26

11. Power Spectral Densities of the In-plane (T1) Responses of Panel 3 Center Obtained with Nastran SOL400 (Red), the 74-mode Full ROM (Black) for OASPL of 136dB ...27

12. Power Spectral Densities of the In-plane (T2) Responses of Panel 3 Center Obtained with Nastran SOL400 (Red), the 74-mode Full ROM (Black) for OASPL of 136dB ...27

Figure Page

13. Power Spectral Densities of the Transverse Responses of Panel 4 Center Obtained with Nastran SOL400 (Red), the 74-mode Full ROM (Black) for OASPL of 136dB .. 28
14. Power Spectral Densities of the In-plane (T1) Responses of Panel 4 Center Obtained with Nastran SOL400 (Red), the 74-mode Full ROM (Black) for OASPL of 136dB .. 28
15. Power Spectral Densities of the In-plane (T2) Responses of Panel 4 Center Obtained with Nastran SOL400 (Red), the 74-mode Full ROM (Black) for OASPL of 136dB ...29
16. Power Spectral Densities of the Transverse Responses of Panel 5 Center Obtained with Nastran SOL400 (Red), the 74-mode Full ROM (Black) for OASPL of 136dB ...29
17. Power Spectral Densities of the In-plane (T1) Responses of Panel 5 Center Obtained with Nastran SOL400 (Red), the 74-mode Full ROM (Black) for OASPL of 136dB .. 30
18. Power Spectral Densities of the In-plane (T2) Responses of Panel 5 Center Obtained with Nastran SOL400 (Red), the 74-mode Full ROM (Black) for OASPL of 136dB .. 30
19. Power Spectral Densities of the Transverse Responses of Panel 6 Center Obtained with Nastran SOL400 (Red), the 74-mode Full ROM (Black) for OASPL of 136dB ... 31
20. Power Spectral Densities of the In-plane (T1) Responses of Panel 6 Center Obtained with Nastran SOL400 (Red), the 74-mode Full ROM (Black) for OASPL of 136dB ... 31
21. Power Spectral Densities of the In-plane (T2) Responses of Panel 6 Center Obtained with Nastran SOL400 (Red), the 74-mode Full ROM (Black) for OASPL of 136dB ...32
22. Power Spectral Densities of the Transverse Responses of Panel 7 Center Obtained with Nastran SOL400 (Red), the 74-mode Full ROM (Black) for OASPL of 136dB ...32
23. Power Spectral Densities of the In-plane (T1) Responses of Panel 7 Center Obtained with Nastran SOL400 (Red), the 74-mode Full ROM (Black) for OASPL of 136dB ...33
24. Power Spectral Densities of the In-plane (T2) Responses of Panel 7 Center Obtained with Nastran SOL400 (Red), the 74-mode Full ROM (Black) for OASPL of 136dB ...33

Figure Page

25. Power Spectral Densities of the Transverse Responses of Panel 8 Center Obtained with Nastran SOL400 (Red), the 74-mode Full ROM (Black) for OASPL of 136dB ...34
26. Power Spectral Densities of the In-plane (T1) Responses of Panel 8 Center Obtained with Nastran SOL400 (Red), the 74-mode Full ROM (Black) for OASPL of 136dB ...34
27. Power Spectral Densities of the In-plane (T2) Responses of Panel 8 Center Obtained with Nastran SOL400 (Red), the 74-mode Full ROM (Black) for OASPL of 136dB ...35
28. Power Spectral Densities of the Transverse Responses of Panel 9 Center Obtained with Nastran SOL400 (Red), the 74-mode Full ROM (Black) for OASPL of 136dB ...35
29. Power Spectral Densities of the In-plane (T1) Responses of Panel 9 Center Obtained with Nastran SOL400 (Red), the 74-mode Full ROM (Black) for OASPL of 136dB ...36
30. Power Spectral Densities of the In-plane (T2) Responses of Panel 9 Center Obtained with Nastran SOL400 (Red), the 74-mode Full ROM (Black) for OASPL of 136dB ...36
31. Power Spectral Densities of the Transverse Responses of Panel 1 Center Obtained with Nastran SOL400 (Red), the 74-mode Full ROM (Black) for OASPL of 144dB ...37
32. Power Spectral Densities of the In-plane (T1) Responses of Panel 1 Center Obtained with Nastran SOL400 (Red), the 74-mode Full ROM (Black) for OASPL of 144dB ...37
33. Power Spectral Densities of the In-plane (T2) Responses of Panel 1 Center Obtained with Nastran SOL400 (Red), the 74-mode Full ROM (Black) for OASPL of 144dB .. 38
34. Power Spectral Densities of the Transverse Responses of Panel 2 Center Obtained with Nastran SOL400 (Red), the 74-mode Full ROM (Black) for OASPL of 144dB .. 38
35. Power Spectral Densities of the In-plane (T1) Responses of Panel 2 Center Obtained with Nastran SOL400 (Red), the 74-mode Full ROM (Black) for OASPL of 144dB ...39
36. Power Spectral Densities of the In-plane (T2) Responses of Panel 2 Center Obtained with Nastran SOL400 (Red), the 74-mode Full ROM (Black) for OASPL of 144dB ...39

Figure Page

37. Power Spectral Densities of the Transverse Responses of Panel 3 Center Obtained with Nastran SOL400 (Red), the 74-mode Full ROM (Black) for OASPL of 144dB .. 40

38. Power Spectral Densities of the In-plane (T1) Responses of Panel 3 Center Obtained with Nastran SOL400 (Red), the 74-mode Full ROM (Black) for OASPL of 144dB .. 40

39. Power Spectral Densities of the In-plane (T2) Responses of Panel 3 Center Obtained with Nastran SOL400 (Red), the 74-mode Full ROM (Black) for OASPL of 144dB ... 41

40. Power Spectral Densities of the Transverse Responses of Panel 4 Center Obtained with Nastran SOL400 (Red), the 74-mode Full ROM (Black) for OASPL of 144dB ... 41

41. Power Spectral Densities of the In-plane (T1) Responses of Panel 4 Center Obtained with Nastran SOL400 (Red), the 74-mode Full ROM (Black) for OASPL of 144dB ...42

42. Power Spectral Densities of the In-plane (T2) Responses of Panel 4 Center Obtained with Nastran SOL400 (Red), the 74-mode Full ROM (Black) for OASPL of 144dB ...42

43. Power Spectral Densities of the Transverse Responses of Panel 5 Center Obtained with Nastran SOL400 (Red), the 74-mode Full ROM (Black) for OASPL of 144dB ...43

44. Power Spectral Densities of the In-plane (T1) Responses of Panel 5 Center Obtained with Nastran SOL400 (Red), the 74-mode Full ROM (Black) for OASPL of 144dB ...43

45. Power Spectral Densities of the In-plane (T2) Responses of Panel 5 Center Obtained with Nastran SOL400 (Red), the 74-mode Full ROM (Black) for OASPL of 144dB ...44

46. Power Spectral Densities of the Transverse Responses of Panel 6 Center Obtained with Nastran SOL400 (Red), the 74-mode Full ROM (Black) for OASPL of 144dB ...44

47. Power Spectral Densities of the In-plane (T1) Responses of Panel 6 Center Obtained with Nastran SOL400 (Red), the 74-mode Full ROM (Black) for OASPL of 144dB ...45

48. Power Spectral Densities of the In-plane (T2) Responses of Panel 6 Center Obtained with Nastran SOL400 (Red), the 74-mode Full ROM (Black) for OASPL of 144dB ...45

Figure Page

49. Power Spectral Densities of the Transverse Responses of Panel 7 Center Obtained with Nastran SOL400 (Red), the 74-mode Full ROM (Black) for OASPL of 144dB ...46
50. Power Spectral Densities of the In-plane (T1) Responses of Panel 7 Center Obtained with Nastran SOL400 (Red), the 74-mode Full ROM (Black) for OASPL of 144dB ...46
51. Power Spectral Densities of the In-plane (T2) Responses of Panel 7 Center Obtained with Nastran SOL400 (Red), the 74-mode Full ROM (Black) for OASPL of 144dB ...47
52. Power Spectral Densities of the Transverse Responses of Panel 8 Center Obtained with Nastran SOL400 (Red), the 74-mode Full ROM (Black) for OASPL of 144dB ...47
53. Power Spectral Densities of the In-plane (T1) Responses of Panel 8 Center Obtained with Nastran SOL400 (Red), the 74-mode Full ROM (Black) for OASPL of 144dB .. 48
54. Power Spectral Densities of the In-plane (T2) Responses of Panel 8 Center Obtained with Nastran SOL400 (Red), the 74-mode Full ROM (Black) for OASPL of 144dB .. 48
55. Power Spectral Densities of the Transverse Responses of Panel 9 Center Obtained with Nastran SOL400 (Red), the 74-mode Full ROM (Black) for OASPL of 144dB ...49
56. Power Spectral Densities of the In-plane (T1) Responses of Panel 9 Center Obtained with Nastran SOL400 (Red), the 74-mode Full ROM (Black) for OASPL of 144dB ...49
57. Power Spectral Densities of the In-plane (T2) Responses of Panel 9 Center Obtained with Nastran SOL400 (Red), the 74-mode Full ROM (Black) for OASPL of 144dB .. 50
58. A Simple Clamped-Clamped Beam Model Supported by Linear Springs..... 51
59. Lowest 4 Linear Modes of the Beam Model 51
60. Averaged Values of the Modal Coordinates for the Linear Modes.....52
61. Power Spectral Density of the Transverse (a) and In-plane (b) Deflections at the Node with Max. Disp. in the First Bay 54

Figure Page

62. Power Spectral Density of the Transverse Deflections at the Node with Max. Disp. in the First Bay 54

63. Power Spectral Density of the Transverse (a) and In-plane (b) Deflections at the Node with Max. Disp. in the First Bay with Different FE Models and the ROM 56

64. Magnitudes of the Frequency Responses at the Middle Point of Bay 4, Transverse Displacement..... 60

65. Convergence Studies for the β-fixed Interface Modes (a), Characteristic Constraint Modes (b) and α-fixed Interface Modes (c)..... 61

66. Comparison of the Magnitudes of the Frequency Responses at the Middle Point of Bay 4, 6 β-fixed and 30 α-POD Modes and Baseline Model 63

67. Comparison of the Representation Errors in α and β Components, 6 β-fixed and 30 α-POD Modes.....64

68. Comparison of the Magnitudes of the Frequency Responses at the Middle Point of Bay 4, 6 β-fixed and 20 α-POD Modes and Baseline Model 64

69. Representation Errors of the Magnitudes of Frequency Responses in β Versus the Number of α-POD Modes 65

70. Comparison of the Magnitudes of the Frequency Responses at the Middle Point of Bay 4, 30 α-POD and 10 β-POD Modes and Baseline Model.....66

71. Comparison of the Representation Errors in α and β Components, 30 α-POD and 10 β-POD Modes 67

72. Comparison of the Magnitudes of the Frequency Responses at the Middle Point of Bay 4, 30 α-POD and 5 β-POD Modes and Baseline Model.....67

73. Comparison of the Magnitudes of the Frequency Responses at the Middle Point of Bay 4, 20 α-POD and 10 β-POD Modes and Baseline Model..... 68

Figure Page

74. Representation Errors of the Magnitudes of Frequency Responses in β Versus the Number of β-POD Modes 68

75. Mode Shapes of Two Global Modes (a), (b) and Two Local Modes (c), (d) 72

76. Ratios of Kinetic Energy in β Over That in α.....72

77. Relative Norm Dynamic Errors in % of the Magnitudes of the Linear Frequency Responses in α (right column) and β (left column) 73

78. Comparison of the Magnitudes of the Frequency Responses at the Middle Point of Bay 4, Baseline Model and 21 Selected Modes from (a) the Recursive Algorithm (Table 3), (b) Eq. (60) (Table 4) 76

79. Contour Plots of the Norm of Displacements for Linear Modes 8-12 (in Order (a)-(e)) in the Band [127,136] Hz. Dark Blue/Red Zones Correspond to the Lowest/Highest Values 79

80. Contour Plots of the Norm of Displacements for the Linear Modes of Fig. 79 but Each Mode Is Normalized in Each Bay 80

81. Comparison of the Magnitudes of Frequency Responses of the Middle Point of Bay 4 Obtained with 17 Selected Linear Modes and the 17 Modes Model Resulting from a Direct and Optimized Lumping of Modes 8, 9, 10, and 12 on Mode 11. 81

82. Comparison of the Magnitudes of Frequency Responses of the Middle Point of Bay 1 Obtained with 20 Selected Linear Modes and the 19 Modes Model Resulting from Direct Lumping and Optimized Lumping. Frequency Band: (a) [127,136] Hz, (b) [140,145] Hz, (c) [191,196] Hz, (d) [280,300] Hz. 81

83. Comparison of the Magnitudes of Frequency Responses of the Middle Point of Bay 2 Obtained with 18 Selected Linear Modes and the 18 Modes Model Resulting from Direct Lumping 82

Figure Page

84. Comparison of the Magnitudes of Frequency Responses of the Middle Point of Bay 3 Obtained with 19 Selected Linear Modes and the 19 Modes Model Resulting from Direct Lumping 82

85. Comparison of the Magnitudes of Frequency Responses of the Middle Point of Bay 5 Obtained with 17 Selected Linear Modes and the 17 Modes Model Resulting from Direct Lumping 83

86. Comparison of the Magnitudes of Frequency Responses of the Middle Point of Bay 6 Obtained with 17 Selected Linear Modes and the 17 Modes Model Resulting from Direct Lumping 83

87. Comparison of the Magnitudes of Frequency Responses of the Middle Point of Bay 7 Obtained with 16 Selected Linear Modes and the 16 Modes Model Resulting from Direct Lumping 84

88. Comparison of the Magnitudes of Frequency Responses of the Middle Point of Bay 8 Obtained with 15 Selected Linear Modes and the 15 Modes Model Resulting from Direct Lumping 84

89. Comparison of the Magnitudes of Frequency Responses of the Middle Point of Bay 9 Obtained with 18 Selected Linear Modes and the 18 Modes Model Resulting from Direct Lumping 85

90. Illustration of the Optimization Process Using the AR Modeling.....87

91. Simulation Data for the Identification Based Lumping of the Linear Modes 8 to 12; Bay 4 91

92. Data Used for the Identification Based Lumping of the Linear Modes 8 to 12; Bay 4 91

Figure Page

93. Comparison of the Magnitudes of the Frequency Responses at the Middle of Bay 4 Obtained with the Component-centric ROM and with the Appropriate Baseline Model for (a) Nominal Thickness/ Uniform Pressure, (b) 80% of the Nominal Thickness/Uniform Pressure, (c) 120% of the Nominal Thickness and Uniform Pressure, (d) Nominal Thickness and Triangular Pressure Distribution, (e) Same as (d) but ROM Includes Mode 3 93

94. Comparison of the Magnitudes of the Frequency Responses at the Node with Max. Disp. in the First Bay of the Beam 95

95. Comparison of the Magnitudes of the Frequency Responses at the Node with Max. Disp. in the Second Bay of the Beam 95

96. Comparison of the Magnitudes of the Frequency Responses at the Node with Max. Disp. in the Third Bay of the Beam.....96

97. Comparison of the Magnitudes of the Frequency Responses at the Node with Max. Disp. in the Forth Bay of the Beam.....96

98. Magnitude of the Frequency Response at the Middle Point of Bay 4 (the Original 9-bay Panel and the New 9-bay Panel), Transverse Displacement 97

99. Lowest 4 Linear Modes of the Beam in Bay 1 (a) Before Rotation, (b) after Rotation 102

100. Estimated Relation Between Modal Responses of the Rotated Modes 3 and 4 from (a) a Very Short Time Dynamic Simulation (b) a Set of Nonlinear Static Solutions 104

101. Power Spectral Densities of the (a) Transverse and (b) In-plane Deflections at the Node with Max. Disp. in the First Bay (β).....105

102. Power Spectral Densities of the (a) Transverse and (B) In-plane Deflections at the Node with Max. Disp. in the Second Bay (β).....106

103. Power Spectral Densities of the (a) Transverse and (B) In-plane Deflections at the Node with Max. Disp. in the Third Bay (β) 107

104. Power Spectral Densities of the (a) Transverse and (B) In-plane Deflections at the Node with Max. Disp. in the Forth Bay (β) 108

105. Power spectral densities of the second Piola-Kirchhoff stress Sxx for the (a) linear and (b) nonlinear dynamic cases at the Node with Max. Disp. in the First Bay 108

106. Mode Shapes before, $\underline{U}^i$ and $\underline{U}^j$ - left column, and after Rotation, $\underline{\widetilde{U}}^i$ and $\underline{\widetilde{U}}^j$ - right column. (row 1, 2) Entire Structure and (row 3, 4) β-Component (Bay 4) Only 110

107. Power Spectral Densities of the Transverse Responses of Panel 1 Center for OASPL of 136dB Obtained with the 74-mode Mono-ROM (Red), the Component-centric 46-mode ROM with 7 Linear Modes Lumped (Black), the 46-Mode ROM with the Same Linear Modes Eliminated (Blue) 111

108. Power Spectral Densities of the In-plane (T2) Responses of Panel 1 Center for OASPL of 136dB Obtained with the 74-mode Mono-ROM (Red), the Component-centric 46-mode ROM with 7 Linear Modes Lumped (Black), the 46-Mode ROM with the Same Linear Modes Eliminated (Blue) 112

109. Power Spectral Densities of the Transverse Responses of Panel 2 Center for OASPL of 136dB Obtained with the 74-mode Mono-ROM (Red), the Component-centric 46-mode ROM with 6 Linear Modes Lumped (Black), the 46-Mode ROM with the Same Linear Modes Eliminated (Blue) 112

110. Power Spectral Densities of the In-plane (T2) Responses of Panel 2 Center for OASPL of 136dB Obtained with the 74-mode Mono-ROM (Red), the Component-centric 46-mode ROM with 6 Linear Modes Lumped (Black), the 46-Mode ROM with the Same Linear Modes Eliminated (Blue) 113

Figure Page

111. Power Spectral Densities of the Transverse Responses of Panel 3 Center for OASPL of 136dB Obtained with the 74-mode Mono-ROM (Red), the Component-centric 46-mode ROM with 12 Linear Modes Lumped (Black), the 46-Mode ROM with the Same Linear Modes Eliminated (Blue) 113

112. Power Spectral Densities of the In-plane (T2) Responses of Panel 3 Center for OASPL of 136dB Obtained with the 74-mode Mono-ROM (Red), the Component-centric 46-mode ROM with 12 Linear Modes Lumped (Black), the 46-Mode ROM with the Same Linear Modes Eliminated (Blue) 114

113. Power Spectral Densities of the Transverse Responses of Panel 4 Center for OASPL of 136dB Obtained with the 74-mode Mono-ROM (Red), the Component-centric 46-mode ROM with 4 Linear Modes Lumped (Black), the 46-Mode ROM with the Same Linear Modes Eliminated (Blue) 114

114. Power Spectral Densities of the In-plane (T2) Responses of Panel 4 Center for OASPL of 136dB Obtained with the 74-mode Mono-ROM (Red), the Component-centric 46-mode ROM with 4 Linear Modes Lumped (Black), the 46-Mode ROM with the Same Linear Modes Eliminated (Blue) 115

115. Power Spectral Densities of the Transverse Responses of Panel 5 Center for OASPL of 136dB Obtained with the 74-mode Mono-ROM (Red), the Component-centric 46-mode ROM with 13 Linear Modes Lumped (Black), the 46-Mode ROM with the Same Linear Modes Eliminated (Blue) 115

116. Power Spectral Densities of the In-plane (T2) Responses of Panel 5 Center for OASPL of 136dB Obtained with the 74-mode Mono-ROM (Red), the Component-centric 46-mode ROM with 13 Linear Modes Lumped (Black), the 46-Mode ROM with the Same Linear Modes Eliminated (Blue) 116

117. Power Spectral Densities of the Transverse Responses of Panel 6 Center for OASPL of 136dB Obtained with the 74-mode Mono-ROM (Red), the Component-centric 46-mode ROM with 17 Linear Modes Lumped (Black), the 46-Mode ROM with the Same Linear Modes Eliminated (Blue) 116

118. Power Spectral Densities of the In-plane (T2) Responses of Panel 6 Center for OASPL of 136dB Obtained with the 74-mode Mono-ROM (Red), the Component-centric 46-mode ROM with 17 Linear Modes Lumped (Black), the 46-Mode ROM with the Same Linear Modes Eliminated (Blue) 117

119. Power Spectral Densities of the Transverse Responses of Panel 7 Center for OASPL of 136dB Obtained with the 74-mode Mono-ROM (Red), the Component-centric 46-mode ROM with 10 Linear Modes Lumped (Black), the 46-Mode ROM with the Same Linear Modes Eliminated (Blue) 117

120. Power Spectral Densities of the In-plane (T2) Responses of Panel 7 Center for OASPL of 136dB Obtained with the 74-mode Mono-ROM (Red), the Component-centric 46-mode ROM with 10 Linear Modes Lumped (Black), the 46-Mode ROM with the Same Linear Modes Eliminated (Blue) 118

121. Power Spectral Densities of the Transverse Responses of Panel 8 Center for OASPL of 136dB Obtained with the 74-mode Mono-ROM (Red), the Component-centric 46-mode ROM with 2 Linear Modes Lumped (Black), the 46-Mode ROM with the Same Linear Modes Eliminated (Blue) 118

122. Power Spectral Densities of the In-plane (T2) Responses of Panel 8 Center for OASPL of 136dB Obtained with the 74-mode Mono-ROM (Red), the Component-centric 46-mode ROM with 2 Linear Modes Lumped (Black), the 46-Mode ROM with the Same Linear Modes Eliminated (Blue) 119

123. Power Spectral Densities of the Transverse Responses of Panel 9 Center for OASPL of 136dB Obtained with the 74-mode Mono-ROM (Red), the Component-centric 46-mode ROM with 11 Linear Modes Lumped (Black), the 46-Mode ROM with the Same Linear Modes Eliminated (Blue) 119

124. Power Spectral Densities of the In-plane (T2) Responses of Panel 9 Center for OASPL of 136dB Obtained with the 74-mode Mono-ROM (Red), the Component-centric 46-mode ROM with 11 Linear Modes Lumped (Black), the 46-Mode ROM with the Same Linear Modes Eliminated (Blue) 120

125. Power Spectral Densities of the Transverse Responses of Panel 1 Center for OASPL of 144dB Obtained with the 74-mode Mono-ROM (Red), the Component-centric 46-mode ROM with 7 Linear Modes Lumped (Black), the 46-Mode ROM with the Same Linear Modes Eliminated (Blue) 120

126. Power Spectral Densities of the In-plane (T2) Responses of Panel 1 Center for OASPL of 144dB Obtained with the 74-mode Mono-ROM (Red), the Component-centric 46-mode ROM with 7 Linear Modes Lumped (Black), the 46-Mode ROM with the Same Linear Modes Eliminated (Blue) 121

127. Power Spectral Densities of the Transverse Responses of Panel 2 Center for OASPL of 144dB Obtained with the 74-mode Mono-ROM (Red), the Component-centric 46-mode ROM with 6 Linear Modes Lumped (Black), the 46-Mode ROM with the Same Linear Modes Eliminated (Blue) 121

128. Power Spectral Densities of the In-plane (T2) Responses of Panel 2 Center for OASPL of 144dB Obtained with the 74-mode Mono-ROM (Red), the Component-centric 46-mode ROM with 6 Linear Modes Lumped (Black), the 46-Mode ROM with the Same Linear Modes Eliminated (Blue) 122

Figure Page

129. Power Spectral Densities of the Transverse Responses of Panel 3 Center for OASPL of 144dB Obtained with the 74-mode Mono-ROM (Red), the Component-centric 46-mode ROM with 12 Linear Modes Lumped (Black), the 46-Mode ROM with the Same Linear Modes Eliminated (Blue) 122

130. Power Spectral Densities of the In-plane (T2) Responses of Panel 3 Center for OASPL of 144dB Obtained with the 74-mode Mono-ROM (Red), the Component-centric 46-mode ROM with 12 Linear Modes Lumped (Black), the 46-Mode ROM with the Same Linear Modes Eliminated (Blue) 123

131. Power Spectral Densities of the Transverse Responses of Panel 4 Center for OASPL of 144dB Obtained with the 74-mode Mono-ROM (Red), the Component-centric 46-mode ROM with 4 Linear Modes Lumped (Black), the 46-Mode ROM with the Same Linear Modes Eliminated (Blue) 123

132. Power Spectral Densities of the In-plane (T2) Responses of Panel 4 Center for OASPL of 144dB Obtained with the 74-mode Mono-ROM (Red), the Component-centric 46-mode ROM with 4 Linear Modes Lumped (Black), the 46-Mode ROM with the Same Linear Modes Eliminated (Blue) 124

133. Power Spectral Densities of the Transverse Responses of Panel 5 Center for OASPL of 144dB Obtained with the 74-mode Mono-ROM (Red), the Component-centric 46-mode ROM with 13 Linear Modes Lumped (Black), the 46-Mode ROM with the Same Linear Modes Eliminated (Blue) 124

134. Power Spectral Densities of the In-plane (T2) Responses of Panel 5 Center for OASPL of 144dB Obtained with the 74-mode Mono-ROM (Red), the Component-centric 46-mode ROM with 13 Linear Modes Lumped (Black), the 46-Mode ROM with the Same Linear Modes Eliminated (Blue) 125

135. Power Spectral Densities of the Transverse Responses of Panel 6 Center for OASPL of 144dB Obtained with the 74-mode Mono-ROM (Red), the Component-centric 46-mode ROM with 17 Linear Modes Lumped (Black), the 46-Mode ROM with the Same Linear Modes Eliminated (Blue) 125

136. Power Spectral Densities of the In-plane (T2) Responses of Panel 6 Center for OASPL of 144dB Obtained with the 74-mode Mono-ROM (Red), the Component-centric 46-mode ROM with 17 Linear Modes Lumped (Black), the 46-Mode ROM with the Same Linear Modes Eliminated (Blue) 126

137. Power Spectral Densities of the Transverse Responses of Panel 7 Center for OASPL of 144dB Obtained with the 74-mode Mono-ROM (Red), the Component-centric 46-mode ROM with 10 Linear Modes Lumped (Black), the 46-Mode ROM with the Same Linear Modes Eliminated (Blue) 126

138. Power Spectral Densities of the In-plane (T2) Responses of Panel 7 Center for OASPL of 144dB Obtained with the 74-mode Mono-ROM (Red), the Component-centric 46-mode ROM with 10 Linear Modes Lumped (Black), the 46-Mode ROM with the Same Linear Modes Eliminated (Blue) 127

139. Power Spectral Densities of the Transverse Responses of Panel 8 Center for OASPL of 144dB Obtained with the 74-mode Mono-ROM (Red), the Component-centric 46-mode ROM with 2 Linear Modes Lumped (Black), the 46-Mode ROM with the Same Linear Modes Eliminated (Blue) 127

140. Power Spectral Densities of the In-plane (T2) Responses of Panel 8 Center for OASPL of 144dB Obtained with the 74-mode Mono-ROM (Red), the Component-centric 46-mode ROM with 2 Linear Modes Lumped (Black), the 46-Mode ROM with the Same Linear Modes Eliminated (Blue) 128

141. Power Spectral Densities of the Transverse Responses of Panel 9 Center for OASPL of 144dB Obtained with the 74-mode Mono-ROM (Red), the Component-centric 46-mode ROM with 11 Linear Modes Lumped (Black), the 46-Mode ROM with the Same Linear Modes Eliminated (Blue) 128

142. Power Spectral Densities of the In-plane (T2) Responses of Panel 9 Center for OASPL of 144dB Obtained with the 74-mode Mono-ROM (Red), the Component-centric 46-mode ROM with 11 Linear Modes Lumped (Black), the 46-Mode ROM with the Same Linear Modes Eliminated (Blue) 129

CHAPTER 1

INTRODUCTION

1.1 Context and Motivation

The pursuit for durable, reusable hypersonic vehicles has been ongoing for years since the first flight of the X-15. Since then, considerable progress has been made to address the challenges within disciplines including aerodynamics, structural dynamics, heat transfer, material science, guidance and control, and propulsion, yet much effort is still needed to field such an aircraft. In the first phase of a project headed by, the Air Force Research Lab (AFRL) Structural Sciences Center, with partners in industry, previous plans for the fielding of reusable hypersonic vehicles, including the National Aerospace Plane (NASP) and the X-33, were assessed and the knowledge gaps relating to structural design that inhibit the development of such a vehicle [1, 2] were outlined. The second phase of the program confirmed the knowledge gaps identified in Phase I, with a few more knowledge gaps identified [3].

Many of the knowledge gaps identified suggest the necessity to account for nonlinear geometric effects when the deformations of the structure become “large”. Such deformations typically happen to very flexible structures and/or those subjected to very large mechanical and/or thermal loading. Recent examples of the former situation include the large aspect ratio wings of several proposed aircraft such as HALE (“High Altitude Long Endurance”) aircraft and the “sensor-craft”, see [4, 5] and references therein for discussion. Hypersonic vehicles are good examples of the latter category with the large aerodynamic forces and heating induced by the high flight speed, [6, 7].

The need to account for nonlinear geometric effects is in sharp contrast with current industry methods which use a variety of analytical and empirical models based on linear analyses. As the vehicle performance envelopes expand, these models will break down,

leading to overly-conservative designs. Such designs will add extra weight and cost, which will become even larger if/once uncertainties are introduced to reflect the lack of exact knowledge on the state of the vehicle. To exemplify these issues, linear and nonlinear analyses were performed in [8] on a NASP ramp panel with thermal and acoustic loads expected in the flight regime. While the linear analysis overpredicted the displacement response of the panel, translating into an overprediction of the stress which would lead to fatigue failure; the nonlinear analysis produced smaller deflections due to geometric nonlinearity and did not predict fatigue failure, well demonstrating the cost of adopting a linear approach to the problem.

In addition to the consideration of nonlinear geometric effects, the need for the accurate coupling of the disciplines (i.e., structural, thermal, and aerodynamic) present in hypersonic flight problems has been demonstrated. Early related work neglected the mutual coupling between the structural deflections and the aerodynamic heating assuming that the structural displacements were influenced by the temperature field but that the thermal problem was not influenced by the displacements [9, 10] and could be carried out on the undeformed structure. However, this assumption was shown to be significantly inadequate for at least one hypersonic panel [11, 12]. Therefore, considerable attention has been brought to bear on the multi-discipline issue [11, 13]. Providing further complexity is needed consideration of acoustic fatigue, a high-cycle fatigue mechanism induced by high frequency fluctuations of the pressure. Acoustic fatigue has consistently afflicted jet aircrafts for about half a century and is a key design concern for current and future aircrafts the stiffened structure of which exhibits, lightly damped modes in the frequency band of the excitation leading to sharp resonances [14, 15]. Accordingly, dynamic analyses long enough to estimate the fatigue life must also be carried out as part of the design process.

The above comments have demonstrated that the desired analyses for hypersonic vehicles design involve (i) large model size, (ii) long dynamic simulation time, and (iii) multi-physics (i.e., structural, aerodynamics and thermal) coupling requiring iterations of different disciplinary solvers. Furthermore, the random nature of the acoustic loading and uncertainties in the loads and in the model, would transform the problem into a random vibration one, which might require the consideration of multiple time histories in a Monte Carlo setting. Modern computational tools, such as finite element methods and computational fluid dynamics, can of course be used for such analyses, however, the associated computational cost will be extremely large. Accordingly, it has become a vital goal for hypersonic vehicles design that the required analyses be conducted in a very efficient way.

It is for such situations that reduced order models (ROMs) are particularly useful. In linear analyses, the fully coupled systems of 2nd order differential equations obtained for example from finite element models are classically reduced to a smaller (typically much smaller) set of independent ones [16] via a transformation involving the “modes”. Physically, these modes are characteristic deformations of the structure observed when it vibrates freely at certain frequencies (the natural frequencies) while mathematically they are the eigenvectors of a generalized eigenvalue problem. Because of their uncoupling, the equations in the modal space are easily solved. They can then be recombined through the reverse transformation to yield the complete solution of the structural response problem. The large computational cost associated with geometrical nonlinearity calls for the extension of the ROM formulation of linear problems. Recent work has been carried out by approximating the system dynamics under a set of input(s)–output(s), i.e., nonmodal techniques [17, 18]. Their performance highly depends on the selection of the expansion points and the marching-moment order, which is not straightforward and

therefore, inaccurate estimations may occur [19]. Of interest here are so called projection based reduced order models where the response of interest involving a very large number of degrees of freedom is represented as an expansion on a much smaller set of basis functions.

Within this framework, two very different perspectives exist to generate such ROMs; they will be referred to as intrusive and non-intrusive ROMs and differentiate from each other as follows. Intrusive ROM formulations are carried out within the finite element solver with full access to all output variables (e.g., displacements, velocities, stresses at different nodes and different time steps), but also internal variables (e.g., tangent stiffness matrix at each time step), as well as elemental level information on the exact modeling assumptions. They could be qualified of computational reduction methods as the ROM/projection on the basis is an integral part of the solution process. They are well exemplified by the works of [20, 21] and references therein.

Non-intrusive ROM formulations on the other hand are constructed without any access to the core of the finite element solver, e.g., as occurs when using a commercial finite element code. That is, only output variables are available, there is no access to the internal variables, elemental information, and moreover, the exact modeling assumptions may not be fully known because of proprietary limitations. Then, the construction of a non-intrusive ROM could be described as a modeling and identification effort. It would typically involve: (i) the selection of a model which relates the input (forces) to the output (displacement) which involves unknown parameters, and (ii) a strategy to identify these parameters using only input-output information.

As described above, these two complementary classes of reduced order methods are very different and likely focus as well on different segments of engineering. Intrusive ROMs are used/developed by researchers at the forefront of computational mechanics to

develop tomorrow's tools while non-intrusive ROMs would be employed by engineers in companies focused on the design of today's structures using a given, black box finite element code.

The focus of the present effort is on non-intrusive ROMs and more specifically on those based on a physically justified model which generalizes the modal methods of linear structural dynamics. The capabilities of these nonlinear ROMs, referred to as NLROMs, have progressed significantly during the past decade, with the developments focusing primarily on the fundamental issues of selection of the ROM basis, the identification of the ROM coefficients, and the validation of the methodology to structures of growing complexity. While these issues are not fully settled, they are advanced enough that successful ROMs of medium scale structures, e.g., a complex 9-bay panel in [22], the wing of the Predator in [23],have been constructed paving the way for more complex applications, potentially entire aircraft. Even though, NLROMs are much more expedient than full order finite element methods for long simulation times, see [24] for some comparisons, the computational effort to construct and run them does grow rapidly with the number of basis functions ("modes") used in the representation, or equivalently, with the complexity of the structural model. The NLROMs share with the linear modal analysis method the dramatic reduction in the number of equations to be solved but not the decoupling property. This is primarily due to the nonlinear terms in the stiffness operator, which are quadratic and cubic in the modal coordinates. Owing to the full set of coupling terms, the NLROM is much more computationally intensive than its linear counterpart, with $O(M^4)$ operations per solution vs. $O(M^2)$ in the linear case - $O(M)$ considering the decoupling – where M is the number of modes retained. One remedy proposed in [24] involves eliminating the nonlinear terms in the ROM that are expected to have small contributions to the nonlinear restoring forces.

Looking ahead to large scale problems, it is desirable to develop methods to "split" the structure in a manner that the number of modes is reduced to maintain the ROM computational efficiency. In fact, such a decomposition into substructures may be quite natural given the stiffened panel make up of aircraft structures. Moreover, the design of aircraft frames for example is not accomplished monolithically but rather by considering separate components (e.g., panels) and modeling their interactions. Component Mode Synthesis (CMS) strategies are very efficient substructuring techniques that use different types of modes to represent the dynamic behavior of the subsystems, yet they appear to be ill-suited for the present nonlinear geometric ROM setting because of the large number of boundary degrees of freedom that they typically induce, even after appropriate reduction.

1.2 Objective

Considering the above discussion, it is desirable to develop "compact" (i.e., with a small number of basis functions) ROMs, referred as "component-centric ROMs" here. Such ROMs are designed to provide an accurate prediction of the linear response of a part of structure (referred to as the "β" component) while allowing a lower accuracy in the rest of the structure (referred to as the "α" component). The advantage of component-centric ROMs over the standard ones is a significant reduction of the number of generalized coordinates needed for stiffened structures. Moreover, the component-centric ROMs corresponding to different parts of the structure are uncoupled and thus can be run in parallel to provide an accurate prediction of the response of the structure in a smaller wall time.

1.3 Overview

In Chapter 2, the key background on linear and nonlinear reduced order modeling is presented. The elements that collectively form the ROMs, i.e., the strategies to select the

basis functions and the determination of the parametric form of the governing equations, are reviewed. Finally, a short review of some Component Mode Synthesis methods is provided and published efforts toward extending substructuring techniques to nonlinear analysis are discussed.

Chapter 3 introduces the structural models used for the assessment of the component-centric ROMs. They are (i) a modified version of the NASA 9-bay panel [24] already studied from the standpoint of nonlinear ROM [25] and a simple clamped-clamped beam supported with linear springs. The beam model was created to mimic the features of the 9-bay panel and used to provide a first validation of the method in the nonlinear case. Their nonlinear ROMs are constructed to establish a baseline against which component-centric ROMs will be compared.

Chapter 4 focuses on the development of component-centric ROMs for the linear case. Two strategies based on the Craig-Bampton Method are first presented. They both start with a set of modes for the β component. The response in the α component induced by these modes is then determined and optimally represented using a Singular Value Decomposition (SVD) strategy. Next, a third approach based on the "Global-Local" Method is also considered to generate first the "global" modes by "smoothing"/ "averaging" the mass property over α and β comp., respectively, to extract a "coarse" model of α and β. Then "local" modes orthogonal to the "global" ones are determined and added to the basis to enrich the modeling of the β component. The last approach described in the linear case is based on the linear modes of the structure, reducing first this set to those dominant in the β component and then "lumping" discarded modes onto some of the dominant ones with close frequencies and similar mode shapes in the β component for increased accuracy. The validation and assessment of these methods will be carried out on the modified version of the NASA 9-bay panel [25].

With the modal lumping method leading to the most “compact” (i.e., smallest number of modes) ROM, its formulation is extended to the nonlinear geometric problem in Chapter 5. The applicability and accuracy of this approach is then verified first on the clamped-clamped beam and then on the modified 9-bay panel model.

A summary of this work is presented in Chapter 6 together with a plan for potential future research.

CHAPTER 2

BACKGROUND

2.1 Introduction

The current state of computational capabilities already allows the consideration of very complex structural models and in principle of their analysis by commercial finite element software. Yet, the computational time that is required for these analyses is often very significant rendering them inadequate as design tools. This issue calls for the development of reduction techniques which approximate the finite element solutions with much shorter simulation time. Modal reduction techniques based on a small set of "modes" or basis functions that representing the physical displacement field have been well-documented in the literature. They are quite efficient to predict the linear response of complex structures, especially in the low-frequency band (characterized by a typically small modal density and relatively well-isolated resonances). Despite differences between the existing techniques, their overall objective is to transform the large scale finite element models, into much lower order systems. Such reductions can be achieved via a mapping of the physical displacement field into a small number of generalized coordinates with an appropriate transformation matrix, $\boldsymbol{V} \in \mathbb{R}^{N\times M}$, where N and M, ($M \ll N$) are the number of degrees of freedom of the original finite element model and the reduced-order models, respectively. The columns of $\boldsymbol{V}$ will be referred to as basis functions. In the linear modal reduction techniques, the transformation matrix typically includes as basis functions the "modes", reviewed briefly in the ensuing section.

2.2 Linear Reduced Order Models

Consider a linear discrete system with N degrees of freedom (DOFs) of equations of motion:

$$\widetilde{\boldsymbol{M}}\underline{\ddot{u}} + \widetilde{\boldsymbol{D}}\underline{\dot{u}} + \widetilde{\boldsymbol{K}}\underline{u} = \underline{\widetilde{\boldsymbol{F}}} \tag{1}$$

where $\widetilde{\boldsymbol{M}}$, $\widetilde{\boldsymbol{D}}$, and $\widetilde{\boldsymbol{K}}$ are the mass, damping, and stiffness matrices of the system and are $N \times N$ matrices. The modes $\underline{\psi_i}$ are then defined as the eigenvectors of the generalized eigenvalue problem:

$$\widetilde{\boldsymbol{K}}\underline{\psi_i} = \omega_i^2 \widetilde{\boldsymbol{M}}\underline{\psi_i} \tag{2}$$

where ω_i is the corresponding natural frequency. Owing to the symmetry of the mass and stiffness matrices, the modes are known to satisfy the orthogonality properties:

$$\begin{aligned} \underline{\psi_i}^T \widetilde{\boldsymbol{M}}\underline{\psi_j} &= 0 \\ \underline{\psi_i}^T \widetilde{\boldsymbol{K}}\underline{\psi_j} &= 0 \end{aligned} \tag{3}$$

for $i \neq j$, and to form a basis for the N-dimension space. Therefore, the physical displacement of the structure can also be represented as:

$$\underline{u}(t) = \sum_{i=1}^{N} q_i(t)\underline{\psi_i} \tag{4}$$

where the variables $q_i(t)$ are called the generalized coordinates. It is convenient in the sequel to normalize the modes with respect to the mass matrix, that is

$$\begin{aligned} \underline{\psi_i}^T \widetilde{\boldsymbol{M}}\underline{\psi_i} &= 1 \\ \underline{\psi_i}^T \widetilde{\boldsymbol{K}}\underline{\psi_i} &= \omega_i^2 \end{aligned} \tag{5}$$

Substituting Eq. (4) into Eq. (3), and then pre-multiplying the result by the transpose of the mode shapes, yields the set of uncoupled differential equations:

$$\ddot{q}_i + 2\zeta_i\omega_i\dot{q}_i + \omega_i^2 q_i = \tilde{F}_i \tag{6}$$

assuming the damping to be "classical". Then, ζ_i is the damping ratio in the i^{th} mode and F_i is the modal force. Typically, only the modes in the low frequency range contribute significantly to the response, thus, the solution for Eq. (1) can be approximated by truncating Eq. (4) to M modes, $M \ll N$.

2.3 Non-intrusive Nonlinear Geometric Reduced Order Models

The linear formulation considered in the previous section is typically valid only for "small" deformations of the structure. When they get larger, nonlinear geometric effects due to large translations and rotations can be observed and their neglect can lead to large errors in the response predictions. Accordingly, it is desired to extend the modal modeling strategies to the formulation of Nonlinear Geometric Reduced Order Models (NLROMs) with basis functions that are time invariant and satisfy the geometric boundary conditions. Since the structure is continuously changing in the deformed configuration with possible changes in location of the boundary conditions, one would expect the basis functions to be similarly varying in that configuration. To avoid this pitfall, the ROM development is conducted in the undeformed configuration Ω_o. The equation of motion is then given by:

$$\frac{\partial}{\partial X_k}\left(F_{ij}S_{jk}\right) + \rho_0 b_i^0 = \rho_0 \ddot{u}_i \tag{7}$$

where $\boldsymbol{S}$ is the second Piola-Kirchhoff stress tensor, ρ_0 is the density and b_i^0 is the vector of body forces, all of which are assumed to depend on the position $X \in \Omega_o$. Further, $\boldsymbol{F}$ denotes the deformation gradient tensor:

$$F_{ij} = \frac{\partial x_i}{\partial X_j} = \delta_{ij} + \frac{\partial u_i}{\partial X_j} \tag{8}$$

where δ_{ij} is the Kronecker delta and $\underline{u} = \underline{x} - \underline{X}$ is the displacement vector, $\underline{x}$ being the position vector in the deformed configuration.

For linear elastic material, the constitutive relation:

$$S_{ij} = C_{ijkl}E_{kl} \tag{9}$$

is adopted here where $\boldsymbol{C}$ is the fourth order elasticity tensor, in general dependent on the undeformed coordinates $\underline{X}$, and $\boldsymbol{E}$ is the Green strain tensor.

$$E_{ij} = \frac{1}{2}\left(F_{ki}F_{kj} - \delta_{ij}\right) \tag{10}$$

Note in Eqs. (7-10) and in the sequel that summation is implied over repeated indices. In parallel to Eq. (4), a nonlinear ROM can be developed by expressing the displacement field as

$$u_i(\underline{X}, t) = \sum_{n=1}^{M} q_n(t)\psi_i^{(n)}(\underline{X}) \tag{11}$$

where $\boldsymbol{\psi}$ are constant basis functions that satisfy the geometric boundary conditions in the undeformed configuration. Introducing Eq. (11) in Eqs. (7) - (10) and enforcing the condition that the error be orthogonal to the basis (i.e., a Galerkin approach is selected), a set of nonlinear ordinary differential equations for the generalized coordinates $q_n(t)$ can be obtained. They are the reduced order model equations and take the form:

$$M_{ij}\ddot{q}_j + D_{ij}\dot{q}_j + K_{ij}^{(1)}q_j + K_{ijl}^{(2)}q_j q_l + K_{ijlp}^{(3)}q_j q_l q_p = F_i \tag{12}$$

where M_{ij} denotes the elements of the mass matrix, $K_{ij}^{(1)}$, $K_{ijl}^{(2)}$, $K_{ijlp}^{(3)}$ are the linear, quadratic, and cubic stiffness coefficients and F_i are the modal forces. Furthermore, a linear damping term $D_{ij}\dot{q}_j$ has been added to collectively represent various dissipation mechanisms. The determination of the stiffness coefficients is described in the ensuing section.

2.4 Identification of ROM Parameters

To determine the stiffness coefficients, $K_{ijl}^{(2)}$, $K_{ijlp}^{(3)}$ in Eq. (12), one direct thought would be to express the nonlinear stiffness coefficients "explicitly" from the finite element formulation. Such an approach would be possible in an intrusive format based on a total Lagrangian formulation as described above; it is presented here only for completeness. Given the availability of all the finite element tensors, a direct computation of reduced order model parameters would be easily performed.

To this end, assume that the nonlinear governing equations of motion for the full finite element model can be derived following the same format as Eq. (12), with the generalized coordinates $q_n(t)$ replaced with the finite element degree of freedom, u_j:

$$\widetilde{M}_{ij}\ddot{u}_j + \widetilde{D}_{ij}\dot{u}_j + \widetilde{K}_{ij}^{(1)}u_j + \widetilde{K}_{ijl}^{(2)}u_j u_l + \widetilde{K}_{ijlp}^{(3)}u_j u_l u_p = \widetilde{F}_i \tag{13}$$

Given Eq. (11), the nonlinear stiffness matrices in the modal coordinates could then be written as:

$$\begin{aligned} K_{ijl}^{(2)} &= \widetilde{K}_{prs}^{(2)}\psi_p^{(i)}\psi_r^{(j)}\psi_s^{(l)} \\ K_{ijlp}^{(3)} &= \widetilde{K}_{rsuv}^{(3)}\psi_r^{(i)}\psi_s^{(j)}\psi_u^{(l)}\psi_v^{(p)} \end{aligned} \tag{14}$$

In a non intrusive ROM formulation, one must proceed differently with the absence of $\widetilde{K}_{ijl}^{(2)}$ and $\widetilde{K}_{ijlp}^{(3)}$. More specifically, an *identification* of the reduced order model parameters must be performed. It relies on the imposition on the finite element model of specified displacement fields or prescribed static loads so that a system of equations can be developed and solved for the stiffness coefficients. In the displacement-based approach [26, 27], a specified displacement field in the form of Eq. (11) is imposed in the commercial finite element software and the nonlinear restoring forces from a nonlinear static analysis are outputted. These restoring forces can then be projected on the modal basis to obtain the nonlinear modal forces, $\underline{F_{NL}} \in \mathbb{R}^{M\times 1}$, which satisfy:

$$F_{NL,i} = K_{ij}^{(1)}q_j + K_{ijl}^{(2)}q_j q_l + K_{ijlp}^{(3)}q_j q_l q_p \tag{15}$$

As the modal forces $\underline{F_{NL}}$ and the generalied coordinates q_j are known, Eq. (15) constitutes a set of linear algebraic equations solved for the stiffness coefficients. A related version of this approach [22] utilizes the tangent stiffness matrix at the displaced configuration if this matrix can be extracted.

Alternatively, the coefficients can be evaluated from a set of nonlinear static solutions under a set of prescribed static loads [28, 29]. These loads are scaled, linear combination

of a few selected basis fuctions in the form of Eq. (11). Applying these loads to the nonlinear finite element model results in a set of displacement fields which are then projected on the ROM basis to obtain the corresponding generalized coordinated q_j. Finally, relating projected forces and displacements through Eq. (15) provides the equations necessary to identify the nonlinear stiffness coefficients. Note finally in both approaches that the set of equations for the stiffness coefficients is linear in these variables. Full details can be found in [22, 26, 29].

2.5 ROM Basis Selection

An important step in the construction of a ROM is the selection of the basis functions needed to represent the displacement field. If the structural response is not well represented within the basis, the corresponding prediction of the reduced order model will in general be poor. In linear problems, the displacement field is generally transverse dominated and thus, the basis consists of linear transverse modes (well separated or isolated) in the low frequency range. However, in nonlinear problems, a significant increase in the in-plane response is often observed resulting from the "membrane stretching" effect. This phenomenon is due to the nonlinear coupling of the transverse and in-plane motions, leading to a softening effect on the transverse motion.

Since the in-plane response is directly related to the transverse motion, a natural thought is to treat them as "companions" of the transverse response to model them implicitly to retain the "softening" effects with only bending modes considered in the basis.

Therefore, the concept of static condensation is applied with the following assumptions:

1) the modal forces associated with in-plane modes are zero.
2) the in-plane inertia and damping can be neglected.
3) there is no nonlinearity in the in-plane displacements.

The first step of condensation is to separate the governing equation Eq. (12) into those corresponding to transverse/bending modes and in-plane modes for symmetric structures:

$$M_{ij}^{(t)}\ddot{q}_j^{(t)} + D_{ij}^{(t)}\dot{q}_j^{(t)} + K_{ij}^{(1t)}q_j^{(t)} + K_{ijl}^{(2t)}q_j^{(t)}q_l^{(i)} + K_{ijlp}^{(3t)}q_j^{(t)}q_l^{(t)}q_p^{(t)} = F_i^{(t)} \tag{16}$$

$$M_{ij}^{(i)}\ddot{q}_j^{(i)} + D_{ij}^{(i)}\dot{q}_j^{(i)} + K_{ij}^{(1i)}q_j^{(i)} + K_{ijl}^{(2i)}q_j^{(t)}q_l^{(t)} = F_i^{(i)} \tag{17}$$

where $q_j^{(t)}$ and $q_j^{(i)}$ denote the generalied coordinates for transverse modes (superscript (t)) and in-plane modes (superscript (i)), respectively. Typically, the natural frequencies of in-plane modes are much higher than excitation bands, thus, a static condensation can be used. That is, the terms in $\ddot{q}_j^{(i)}$ and $\dot{q}_j^{(i)}$ are eliminated from Eq. (17) and the in-plane coordinates $q_j^{(i)}$ are then simply expressed in terms of their transverse counterparts as:

$$q_j^{(i)} = -[\boldsymbol{K}^{1i}]_{js}^{-1}K_{srl}^{(2i)}q_r^{(t)}q_l^{(t)} \tag{18}$$

Introducing Eq. (18) into Eq. (16),

$$M_{ij}^{(t)}\ddot{q}_j^{(t)} + D_{ij}^{(t)}\dot{q}_j^{(t)} + K_{ij}^{(1t)}q_j^{(t)} + \widehat{K}_{ijlp}^{(3t)}q_j^{(t)}q_l^{(t)}q_p^{(t)} = F_i^{(t)} \tag{19}$$

$$\widehat{K}_{ijlp}^{(3t)} = K_{ijlp}^{(3t)} - K_{ijl}^{(2t)}\,[\boldsymbol{K}^{1i}]_{js}^{-1}K_{slp}^{(2i)} \tag{20}$$

which are transverse only set of equations. For this type of bases, the "net stiffening" effect, $\widehat{\boldsymbol{K}}$, is directly estimated. Such condensed ROMs were introduced and have shown to be successful in a broad range of cases [30, 31].

To recover the full finite element displacement fields:

$$u_i(\underline{X},t) = \sum_{n=1}^{M_t} q_n^{(t)}(t)\psi_i^{(tn)}(\underline{X}) + \sum_{n=1}^{M_i} q_n^{(i)}(t)\psi_i^{(in)}(\underline{X}) \tag{21}$$

The transverse-dominant modes, $\boldsymbol{\psi}^{(t)}$, are typically retained from the linear problem, while the corresponding in-plane modes are identified from the residuals of a given set of

observed nonlinear static responses after projection on the transverse basis functions. This method is usually referred to the Implicit Condensation with Expansion (ICE) [28]. Other modal selection techniques have also been proposed that rely only partially on the linear modes. In this group of methods, the linear modes retained from the linear problems are enriched by other basis functions focused on capturing the membrane stretching effects. While higher order linear modes have been used, see [32], they are generally quite challenging to select. Another strategy has been formulated and well validated that is directly based on the nonlinear coupling of the transverse and in-plane motions. That is, the enrichment modes (referred to as "dual" modes) are contructed to be closely "associated" to the retained (transverse dominated) linear modes, somewhat similarly to the companion modes of [32], but to stand on their own as independent basis functions. Specifically, they are computed from the residuals of projection on the then current basis of a series of nonlinear static solutions to specific loadings. These loadings are determined so that the linear response of the structure to them would induce a response only in the retained linear modes. That is, the residuals would be zero for a linear structure and no dual could be constructed. So, the dual modes capture the effects of nonlinearity induced by the selected set of linear modes.

Turning to the details, the applied load vectors on the finite element models should be in the form of:

$$\underline{\hat{f}} = \sum_i \alpha_i \widehat{\boldsymbol{K}}^{(1)} \underline{\psi}^i \tag{22}$$

such that the corresponding linear static responses are:

$$\underline{\hat{u}} = \sum_i \alpha_i \underline{\psi}^i \tag{23}$$

where α_i are the scaling factor corresponding to mode i. Generally, it is sufficient to only consider the cases:

$$\underline{\hat{f}} = \alpha_i \widehat{\boldsymbol{K}}^{(1)} \underline{\psi}^i, i = dominant\ modes \tag{24}$$

and

$$\underline{\hat{f}} = \frac{\alpha_i}{2}\left(\widehat{\boldsymbol{K}}^{(1)} \underline{\psi}^i + \widehat{\boldsymbol{K}}^{(1)} \underline{\psi}^j\right), i = dominant\ modes, j \neq i \tag{25}$$

In the above equations, the dominant modes are loosely defined as the ones expected to provide large response components, much larger than the other modes, to the actual loading. The appropriate scaling factors α_i should lead to the displacement fields, $\underline{\hat{u}}$, ranging from near linear cases to some exihibiting a strong nonlinearity. The following step is the extraction of the "dual" modes from the obtained finite element displacement fields. A POD analysis using Singular Decomposition Value (SVD) is conducted on the set of residuals of projection of the finite element responses onto the existing basis. A more detailed description of the process can be found in [33, 34].

2.6 Component Mode Synthesis

Component Mode Synthesis is an ensemble of techniques for dynamic substructuring, i.e., for the decomposition of structures in subcomponents, the modeling of these substructures, and their recombination to satisfy continuity conditions and provide a global representation of the response. There are quite a few different possibilities to assemble the substructures which vary from each other in particular by the consideration of the interfaces displacements and forces. One of the classic methods is the Craig-Bampton (CB) Method [35, 36] which uses explicitly all of the degrees of freedom at the interface as generalized coordinates. Then, the representation of the response is achieved by the combination of fixed interface modes and constraint modes as the reduction basis. The fixed interface modes are defined for each substructure as their fully clamped linear modes. The constraint modes on the contrary are the static displacements induced by a unit displacement of each interface degree-of-freedom in turn, with all others set to zero, in the substructures it is connected to. Clearly, this method is inefficient when the

number of interface DOFs is large. Castanier et al. [37] proposed that a secondary general eigen-problem be performed on the interface DOFs to reduce the number of constraint modes, resulting in a more efficient basis, referred to as the characteristic constraint modes

Other methods use the interface forces as interface variables [38, 39], e.g., the Craig-Chang Method. In this method, the response is modeled using free-interface and rigid body modes, i.e., corresponding to the free-free substructure, as well as attachment modes which are the static responses to single loads applied on the structure.

Recent efforts have focused on extending substructuring methods to nonlinear analyses, e.g., [40, 41]. The studies of [42, 43] are particularly relevant to the current focus on non-intrusive NLROMs. Specifically, Perez [42] was the first to investigate the use of the Craig-Bampton methodology to develop a NLROM of a multi-bay panel. He found that a linear substructuring approach could reduce the linear model from 96,000 degrees of freedom to 232 generalized coordinates using fixed-interface and constraint modes reduced using proper orthogonal decomposition. However, the nonlinear modal substructuring was not actually pursued in his work as the reduction of the monolithic structure only required 89 DOFs. A similar substructuring approach was developed for coupling geometrically nonlinear structures, where each subcomponent was reduced to a low order set of nonlinear equations using a truncated set of fixed interface and characteristic constraint modes [43]. This approach reduced a 12,861 DOF finite element model down to 23 mode NLROM. No comparison was however made with a monolithic NLROM to assess the difference in number of generalized coordinates.

CHAPTER 3

VALIDATION MODELS

3.1 A Middle Complexity Multi-Bay Structure

The 9-bay fuselage sidewall panel of [25, 44], was considered for the validation of the component-centric ROMs. It is a representative example of the class of structures for which a component-centric ROM would be desirable as it exhibits well delineated components, i.e., the 9 different bays. As described in [25], the overall dimensions of the panel are 58.1" by 25.06" and it is subdivided into nine geometrically identical bays riveted by a frame and longeron substructure. Each bay measures 18.75" by 7.5" between rivet lines and is identified by its number, 1 to 9, as shown in Fig. 1. The Nastran finite element model consists of 4-node plate elements (CQUAD4) and beam (CBEAM) elements and has a total of 96,156 degrees of freedom. The selected material properties are: Young's modulus of 10.5×10^{6}psi, Poison's ratio equal to 0.33, and a density of $2.614\times10^{-4}lb_f\text{-}s^2/in^4$. Finally, the edges of the skin are simply supported. Further information regarding this model can be found in [25, 44]. In these references, the bays have equal thickness of 0.05" and thus the overall model is nearly symmetrical with the asymmetry arising only from the frame and the longeron configuration. This property implies that the response of the panel to a uniform pressure is dominated by only a limited set of modes vs. the entire set. To promote richer dynamics, the 9 bays were taken here to have different thicknesses selected as (in order of panel, from 1 to 9) 0.0554, 0.0683, 0.0274, 0.0586, 0.0532, 0.0369, 0.0457, 0.0534 and 0.0858 (unit: in). The thickness of the rest of the skin and the frame substructure was selected as in the original model, i.e., 0.05" and 0.04". The structure was assumed to be subjected to a uniform pressure of unit magnitude on its skin only and, a Rayleigh damping model was adopted, i.e.,

$$\boldsymbol{C} = r_1\boldsymbol{M} + r_2\boldsymbol{K} \tag{26}$$

where $\boldsymbol{C}$ denotes the damping matrix and r_1 = 7.55/s and r_2= 5.6×10^{-6}s. This model provides classical damping with damping ratios ranging from 0.65% to 1% of critical in the frequency band of interest, [0,350] Hz.

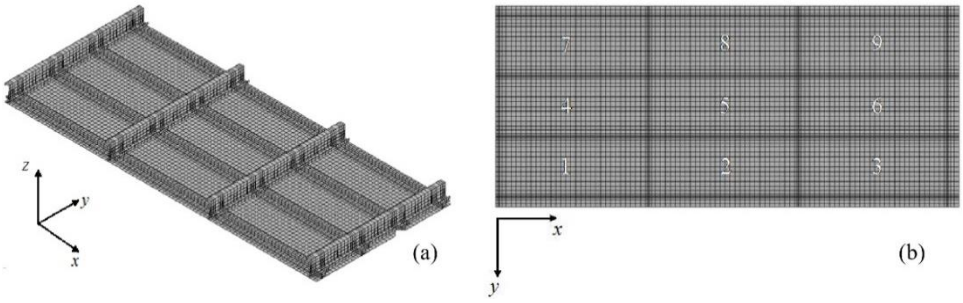

Figure 1 Finite Element Model of the 9-bay Fuselage Sidewall Panel, (a) Isometric View, (b) Top View from [22]

Figure 2 shows the magnitude of the transverse displacement frequency response function of the middle point of Bay 4. This curve was obtained using the first 85 linear modes of natural frequencies ranging from 68 to 500 Hz; it is nearly indistinguishable from the full finite element solution. The in-plane deflections were found much smaller than their transverse counterparts and thus the latter were selected as the primary quantities of interest. The curve of Fig. 2 will be referred to as the "baseline" against which the linear component-centric ROM predictions of the ensuing sections will be compared.

Several observations can be drawn from Fig. 2 and the list of natural frequencies of Table 1. First, while some natural frequencies are well separated from the others, there are several zones densely populated with frequencies. This occurrence is reflected by either tightly packed sharp peaks or broad peaks in Fig. 2. Second, there is a sharp drop of the response around 350Hz and thus the analysis will focus solely on the band [0,350] Hz.

Table 1

Natural Frequencies of the 9-bay Panel (Hz)

68.15	94.89	101.63	107.58	117.64	121.14	125.00	127.48	129.01	130.43
132.00	135.43	138.39	142.23	143.17	149.89	158.29	160.99	165.35	167.34
193.86	195.42	205.09	212.97	218.23	219.67	232.86	233.58	241.09	251.78
254.10	257.24	260.32	266.90	269.53	271.22	279.35	286.20	288.42	292.14
292.93	296.87	308.84	310.55	314.94	318.59	325.76	330.00	340.73	352.19

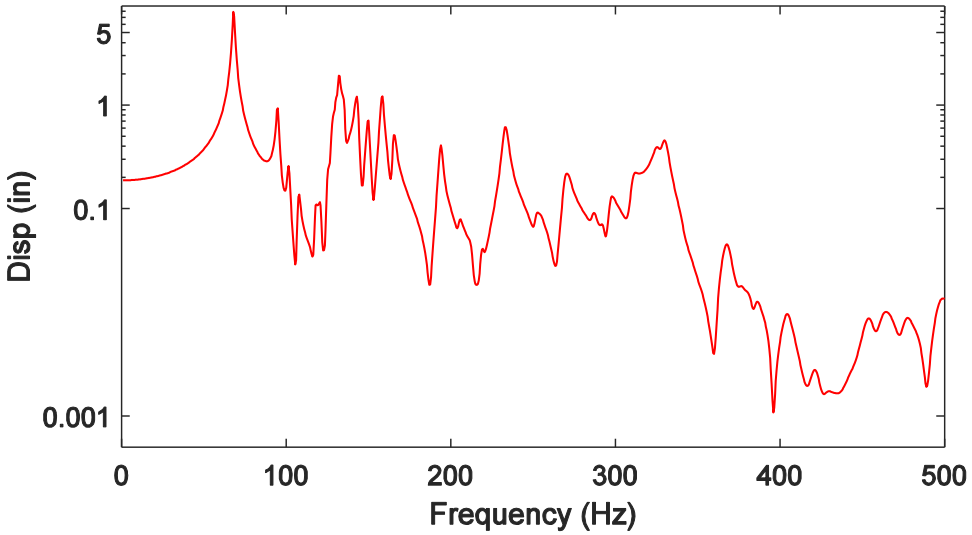

Figure 2 Magnitude of the frequency response at the middle point of Bay 4, transverse displacement

3.2 Nonlinear ROM Construction for the Multi-Bay Structure

The nonlinear ROM for the 9-bay panel started with the selection of the linear modes to be incorporated in the model. To gather data on this issue, a series of 10 uniform pressures were applied to the top (skin) of the panel, and the corresponding NX/Nastran nonlinear static responses (SOL 106) were obtained to provide a sample of "snapshots" for the reduced order model construction. The peak transverse deflections (direction normal to the skin panel) ranged from 0.1 to 5 skin panel thicknesses. These "snapshots" were used to assess the need to include particular linear modes in the model and as a result, all 50 linear modes in the band of interest [0,350] Hz were retained as they almost all affect the response of some bay(s), see Fig. 3. Next, dual modes were determined as described in section 2.5 using the 10 linear modes with the largest modal

components, i.e. modes 1, 2, 3, 4, 6, 7, 11, 16, 17 and 19. Since the modal component of mode 1 is much larger than the other ones for all static responses analyzed, it was considered as the only dominant mode in Eqs. (24) and (25).

The POD-based dual mode construction procedure highlighted in Chapter 2 was performed for the data obtained for mode 1 alone and each of the 9 combinations of mode 1 and another of the 10 largest responding modes (see Fig. 3). In each of these 10 situations, 22 different loading factors, α_i, (see Eqs. (24) and (25)) were used, half positive and half negative, and leading to peak deflections ranging from 0.1 to approximately 5 skin panel thicknesses. The remainders of these 220 deflections, after projection on the 50 linear modes identified above, were analyzed by POD. The POD eigenvectors with largest eigenvalues and significant linear strain energy were selected as dual modes. Each of them led to a reduction of the representation error of the T1 (i.e., x component) and T2 (i.e., y component) components. Then, 24 duals modes were identified in this manner and added to the 50 linear modes leading to a 74-mode nonlinear ROM.

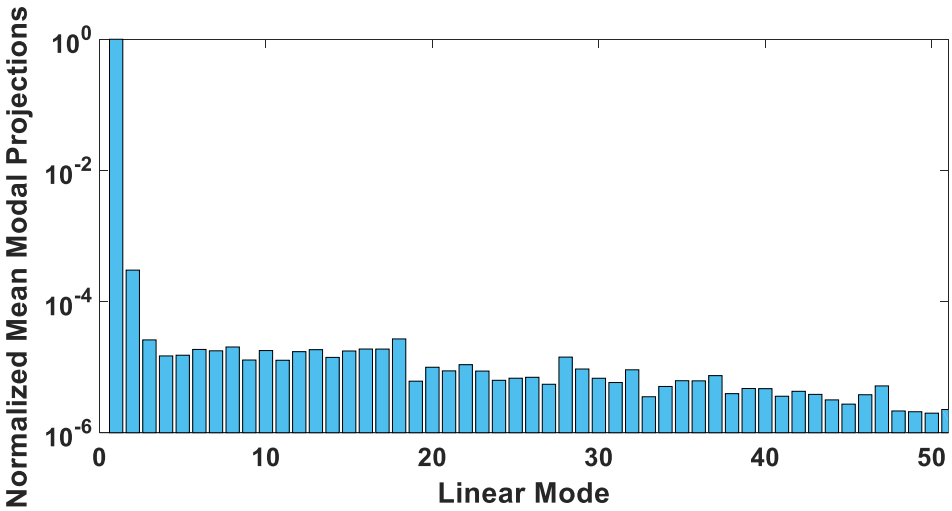

Figure 3 Normalized mean modal projection on a sample of "snapshots"

Two dynamic loading cases were tested, they both consisted of a uniform pressure on its top surface varying randomly in time as a white noise band-limited process in the

frequency range [0,350] Hz to simulate an acoustic loading. In the first case, the overall sound pressure level (OASPL) was 136dB while it was 144dB in the second case. The former leads to a peak transverse displacement of approximately 1 skin panel thicknesses which lies in the geometric nonlinear regime (as can be confirmed by comparison with a linear analysis), while the later results in a peak transverse displacement of approximately 2.6 skin panel thicknesses which is well in the geometric nonlinear regime. The damping assumption was the same as in the linear case. The validation results of the ROM comparing to Nastran SOL400 are plotted below (Fig. 4-57) and as shown, the ROM predictions match well with those from Nastran, for all bays and all loading levels.

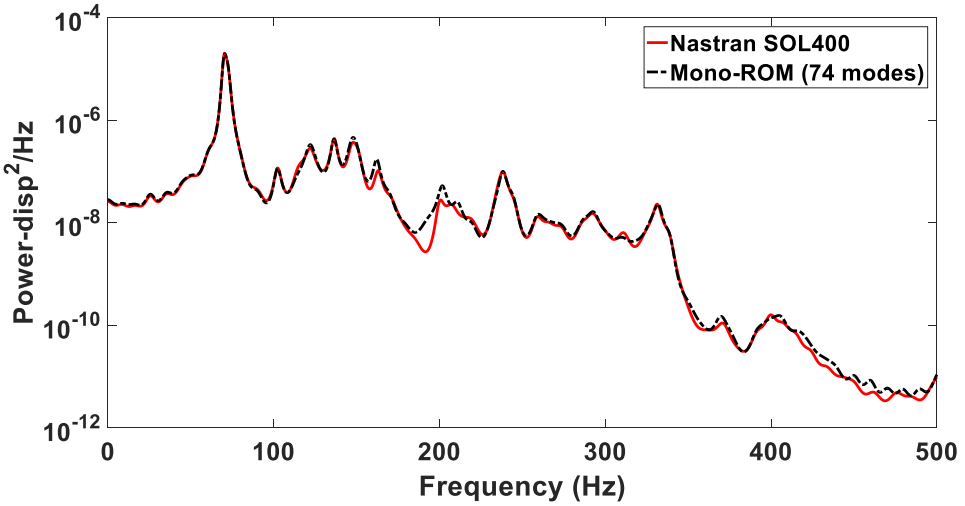

Figure 4 Power spectral densities of the transverse responses of Panel 1 center obtained with Nastran SOL400 (red), the 74-mode full ROM (black) for OASPL of 136dB

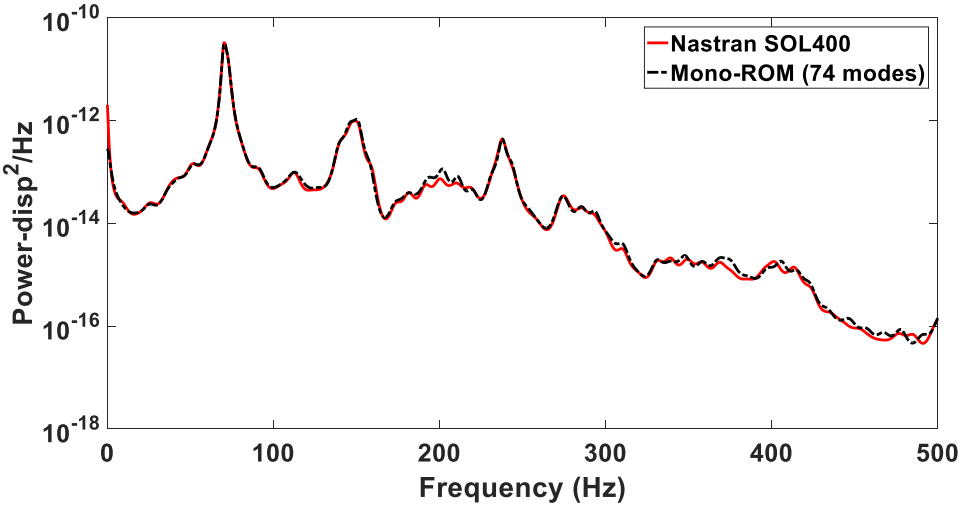

Figure 5 Power spectral densities of the in-plane (T1) responses of Panel 1 center obtained with Nastran SOL400 (red), the 74-mode full ROM (black) for OASPL of 136dB

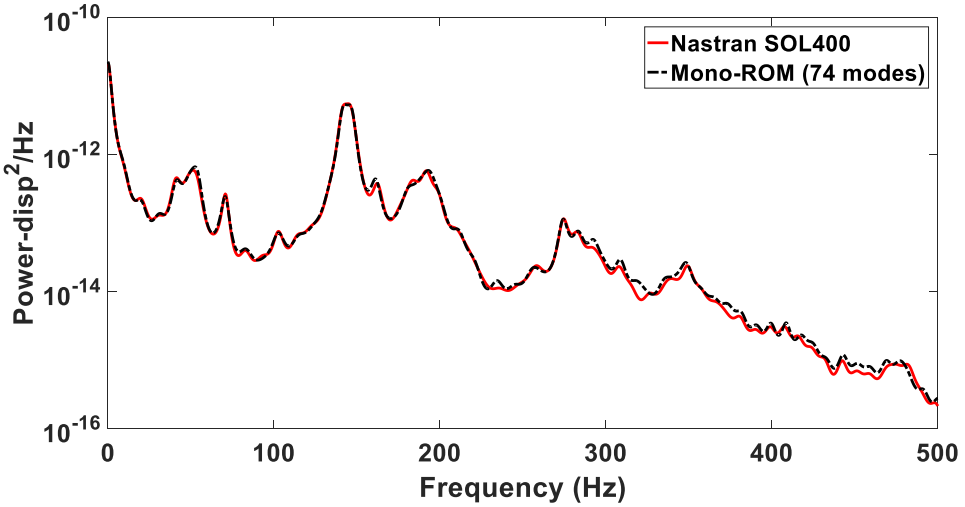

Figure 6 Power spectral densities of the in-plane (T2) responses of Panel 1 center obtained with Nastran SOL400 (red), the 74-mode full ROM (black) for OASPL of 136dB

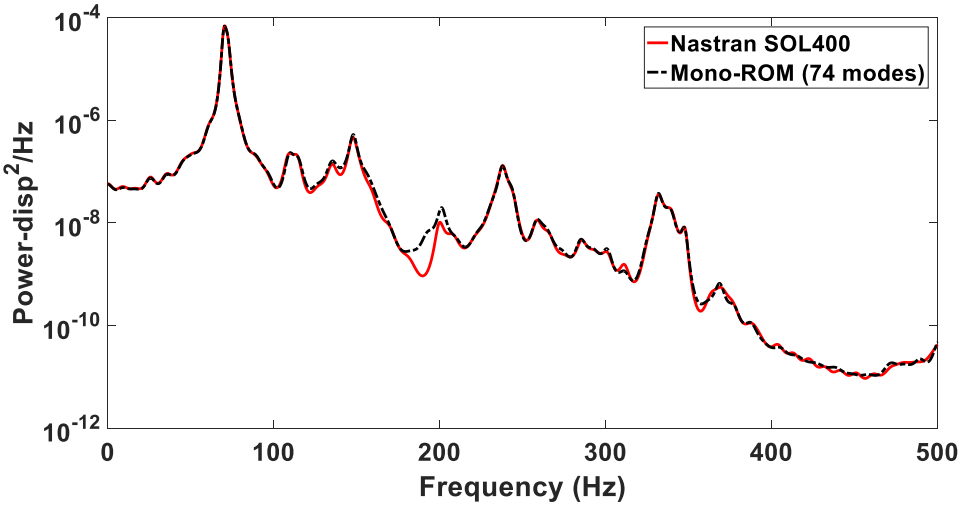

Figure 7 Power spectral densities of the transverse responses of Panel 2 center obtained with Nastran SOL400 (red), the 74-mode full ROM (black) for OASPL of 136dB

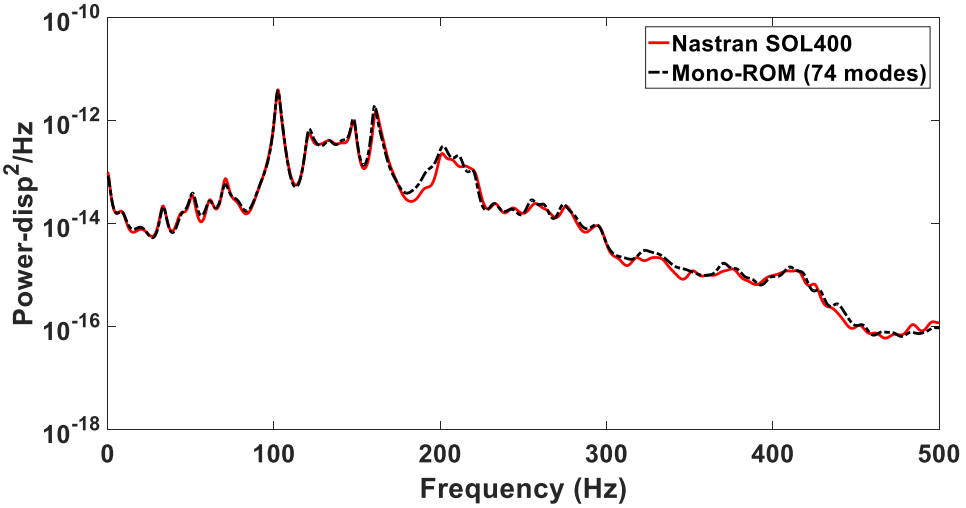

Figure 8 Power spectral densities of the in-plane (T1) responses of Panel 2 center obtained with Nastran SOL400 (red), the 74-mode full ROM (black) for OASPL of 136dB

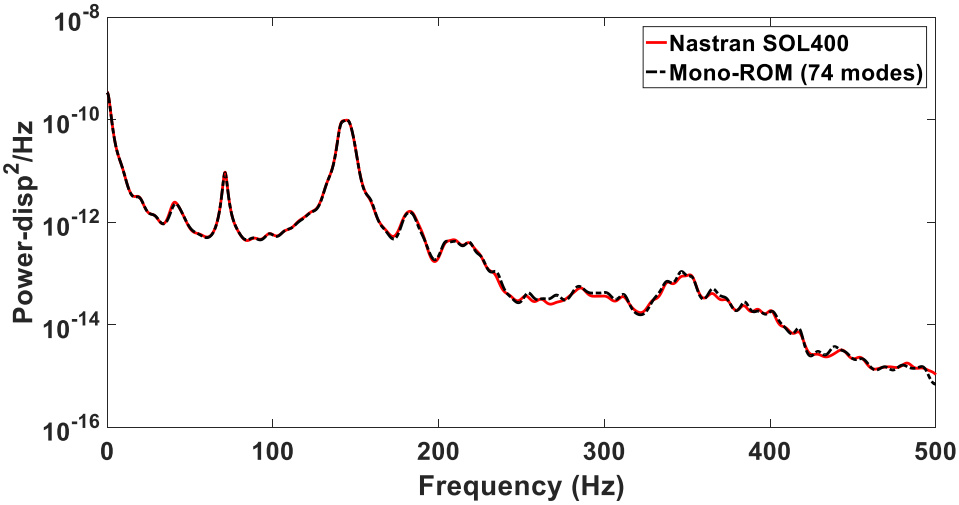

Figure 9 Power spectral densities of the in-plane (T2) responses of Panel 2 center obtained with Nastran SOL400 (red), the 74-mode full ROM (black) for OASPL of 136dB

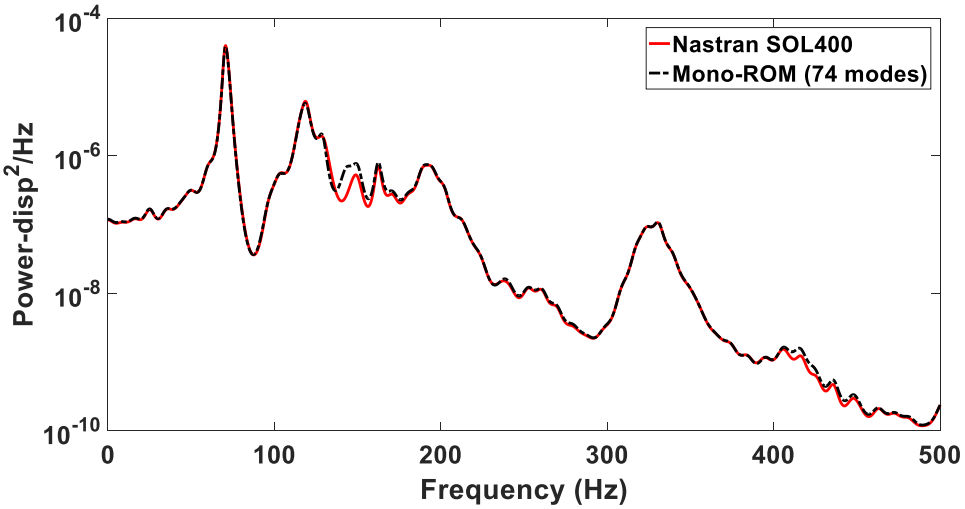

Figure 10 Power spectral densities of the transverse responses of Panel 3 center obtained with Nastran SOL400 (red), the 74-mode full ROM (black) for OASPL of 136dB

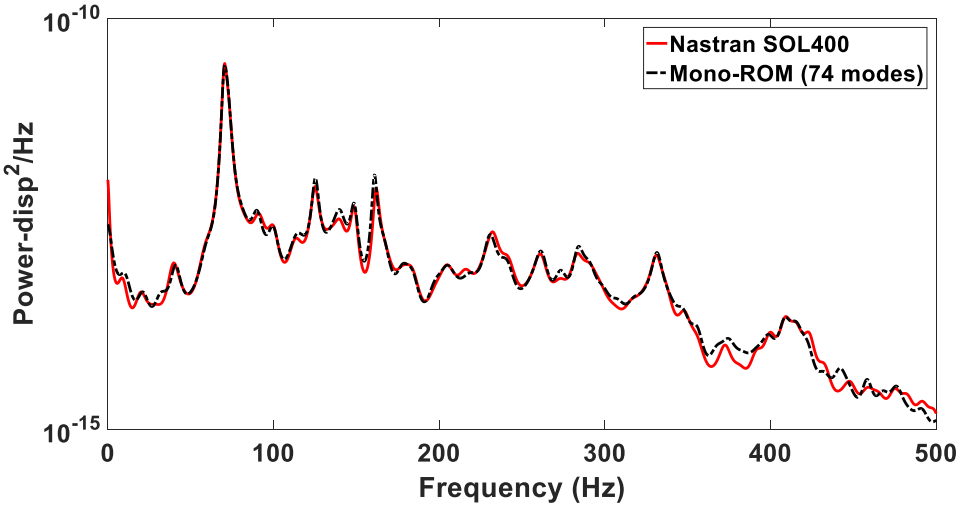

Figure 11 Power spectral densities of the in-plane (T1) responses of Panel 3 center obtained with Nastran SOL400 (red), the 74-mode full ROM (black) for OASPL of 136dB

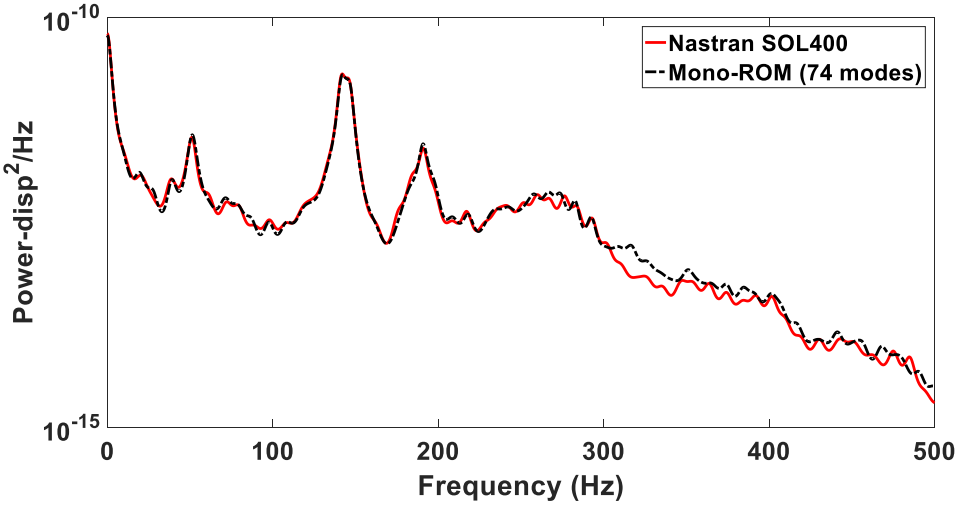

Figure 12 Power spectral densities of the in-plane (T2) responses of Panel 3 center obtained with Nastran SOL400 (red), the 74-mode full ROM (black) for OASPL of 136dB

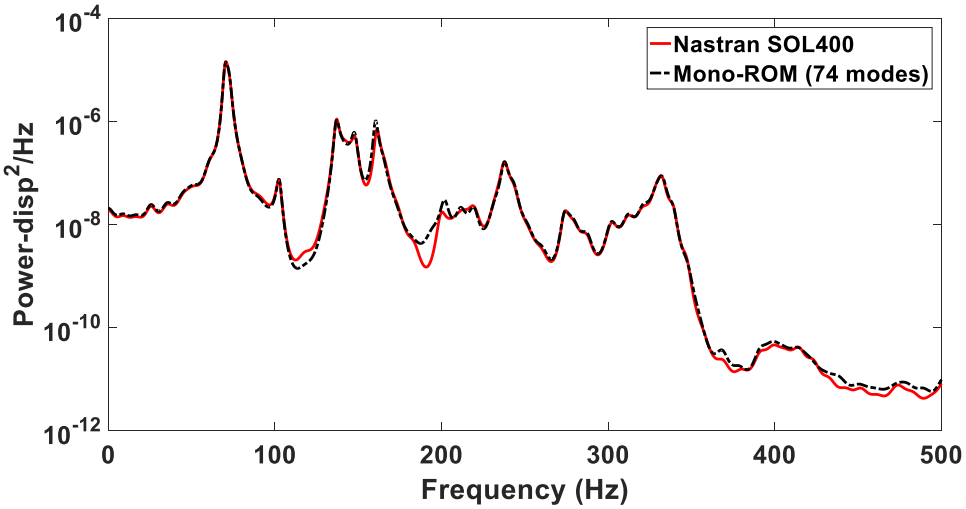

Figure 13 Power spectral densities of the transverse responses of Panel 4 center obtained with Nastran SOL400 (red), the 74-mode full ROM (black) for OASPL of 136dB

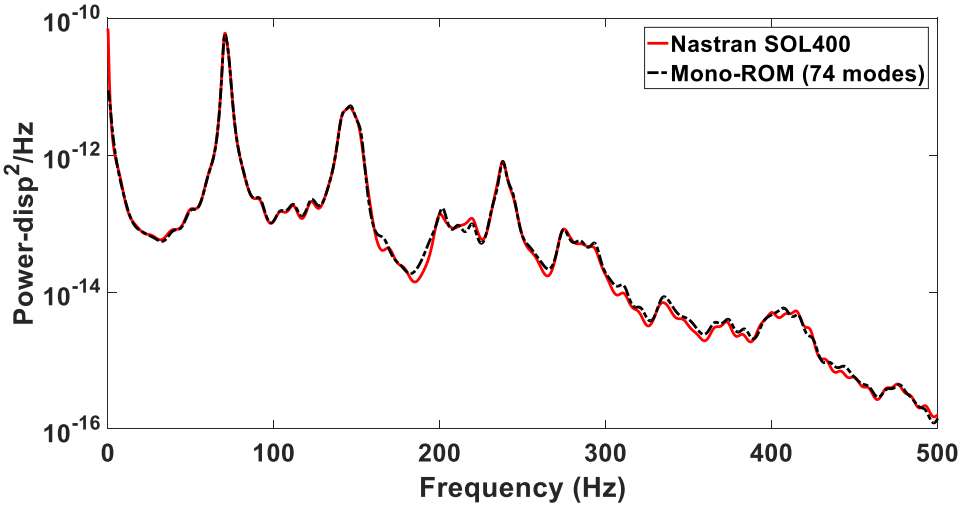

Figure 14 Power spectral densities of the in-plane (T1) responses of Panel 4 center obtained with Nastran SOL400 (red), the 74-mode full ROM (black) for OASPL of 136dB

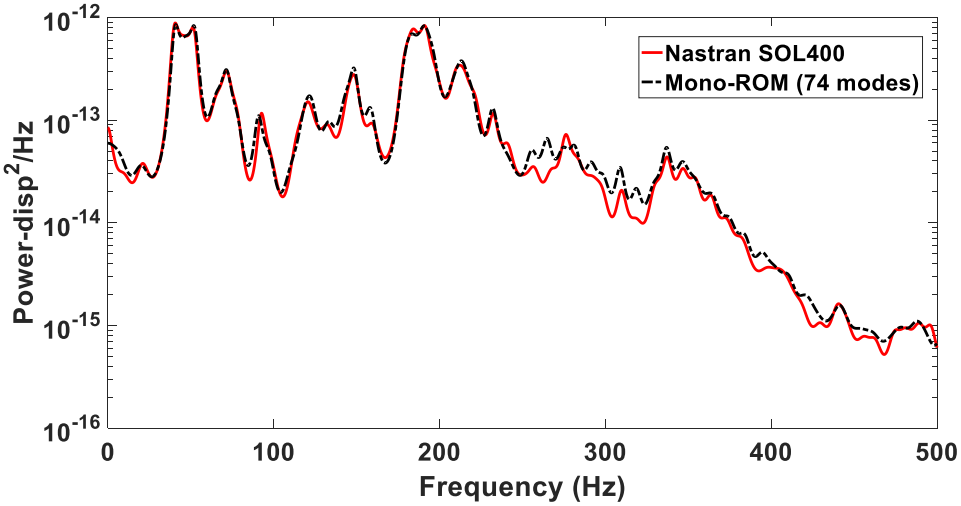

Figure 15 Power spectral densities of the in-plane (T2) responses of Panel 4 center obtained with Nastran SOL400 (red), the 74-mode full ROM (black) for OASPL of 136dB

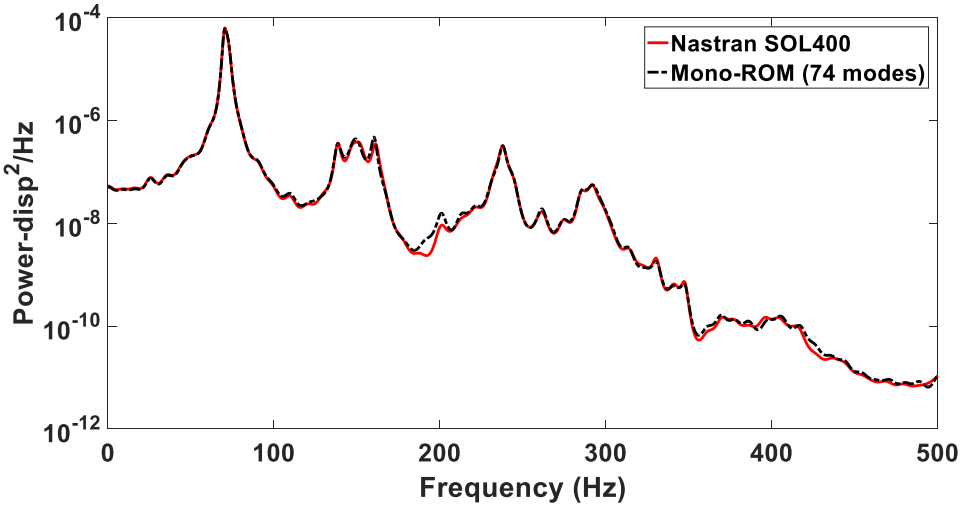

Figure 16 Power spectral densities of the transverse responses of Panel 5 center obtained with Nastran SOL400 (red), the 74-mode full ROM (black) for OASPL of 136dB

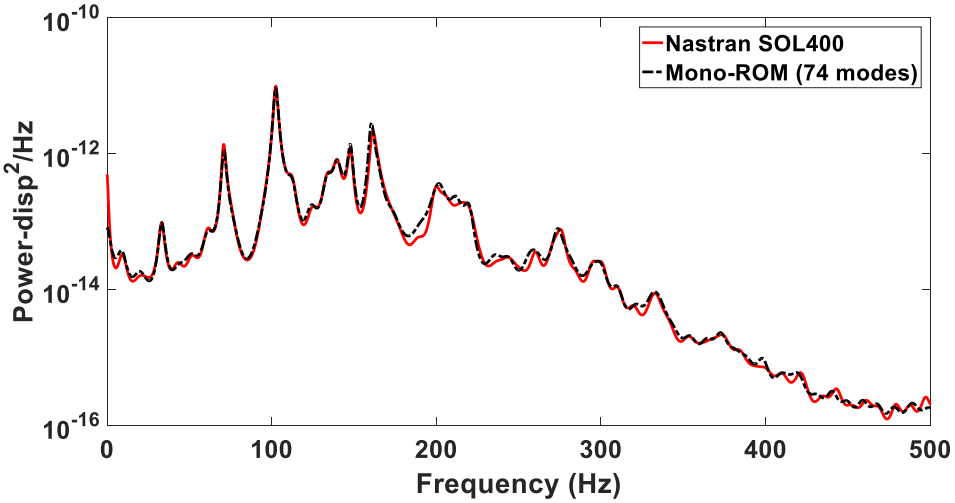

Figure 17 Power spectral densities of the in-plane (T1) responses of Panel 5 center obtained with Nastran SOL400 (red), the 74-mode full ROM (black) for OASPL of 136dB

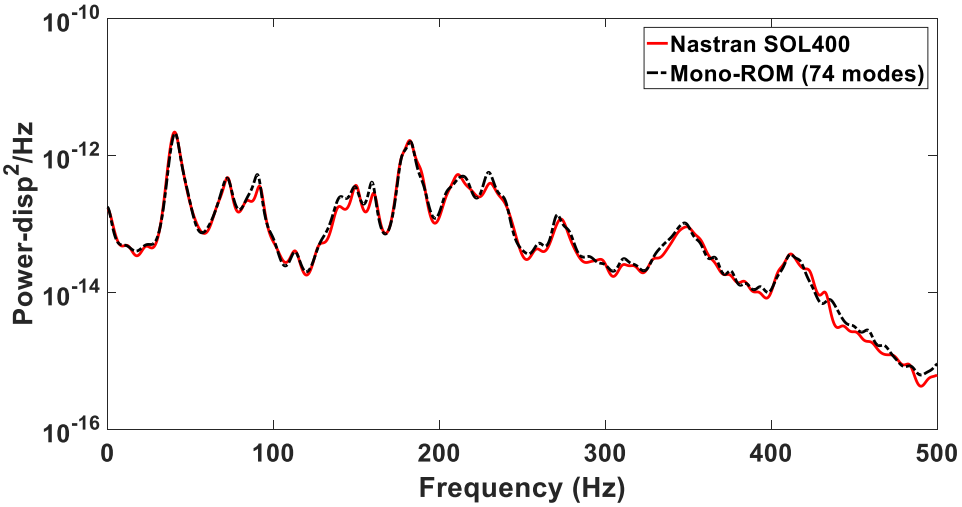

Figure 18 Power spectral densities of the in-plane (T2) responses of Panel 5 center obtained with Nastran SOL400 (red), the 74-mode full ROM (black) for OASPL of 136dB

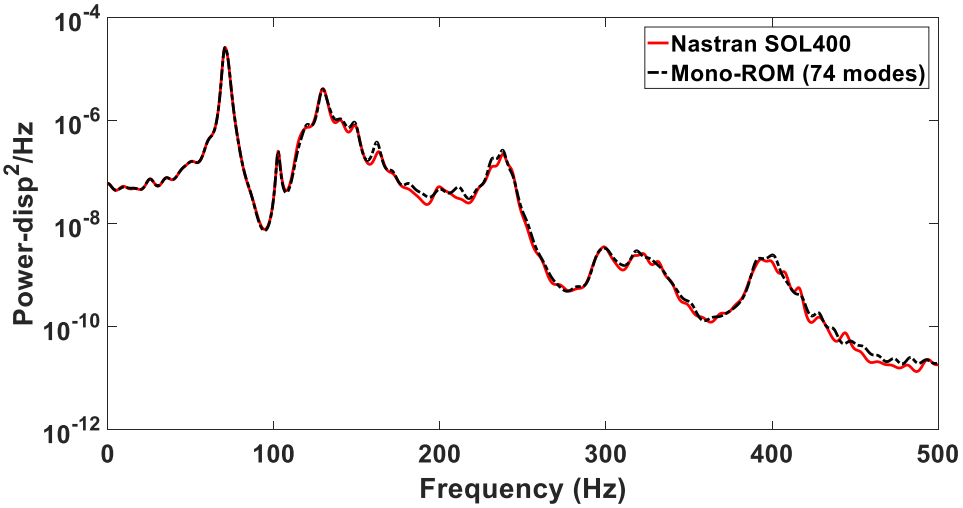

Figure 19 Power spectral densities of the transverse responses of Panel 6 center obtained with Nastran SOL400 (red), the 74-mode full ROM (black) for OASPL of 136dB

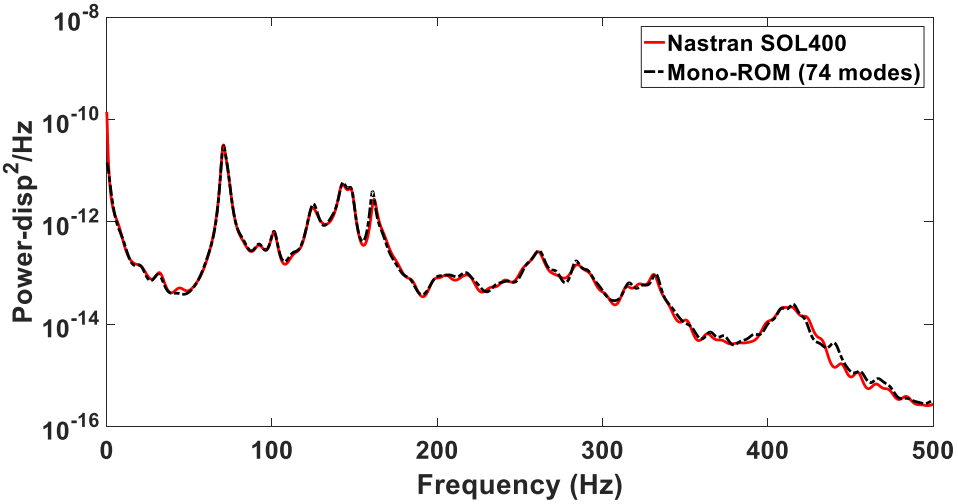

Figure 20 Power spectral densities of the in-plane (T1) responses of Panel 6 center obtained with Nastran SOL400 (red), the 74-mode full ROM (black) for OASPL of 136dB

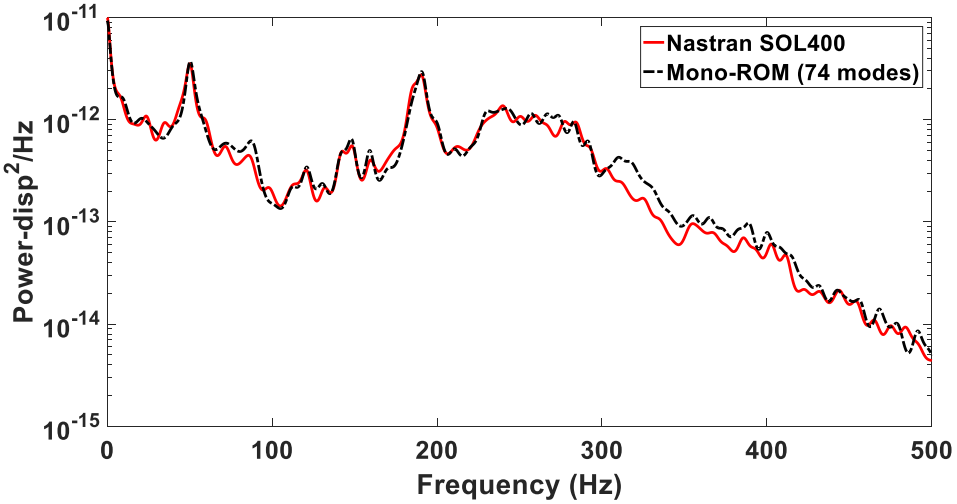

Figure 21 Power spectral densities of the in-plane (T2) responses of Panel 6 center obtained with Nastran SOL400 (red), the 74-mode full ROM (black) for OASPL of 136dB

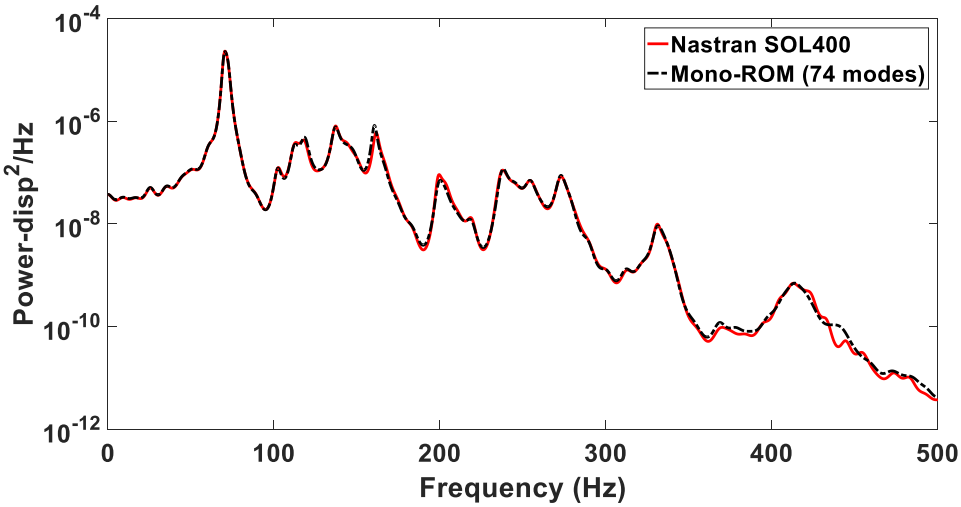

Figure 22 Power spectral densities of the transverse responses of Panel 7 center obtained with Nastran SOL400 (red), the 74-mode full ROM (black) for OASPL of 136dB

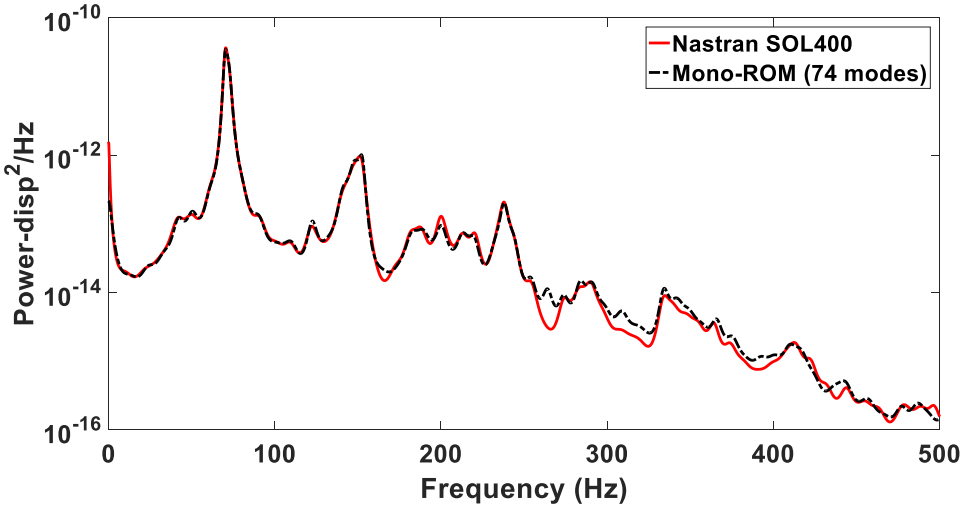

Figure 23 Power spectral densities of the in-plane (T1) responses of Panel 7 center obtained with Nastran SOL400 (red), the 74-mode full ROM (black) for OASPL of 136dB

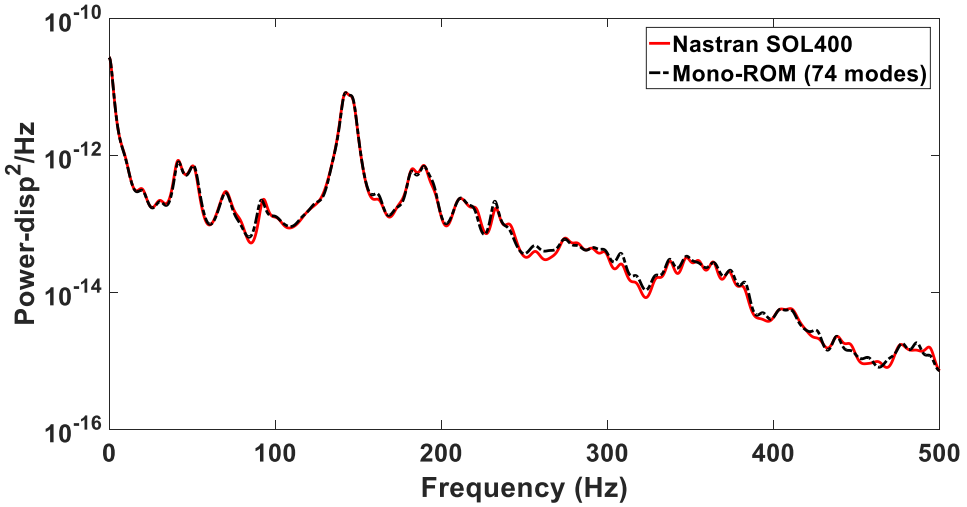

Figure 24 Power spectral densities of the in-plane (T2) responses of Panel 7 center obtained with Nastran SOL400 (red), the 74-mode full ROM (black) for OASPL of 136dB

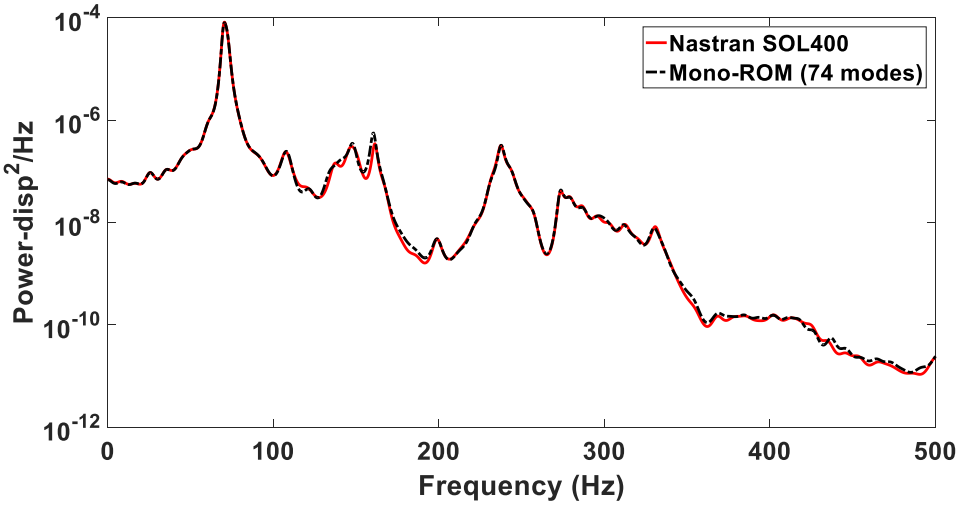

Figure 25 Power spectral densities of the transverse responses of Panel 8 center obtained with Nastran SOL400 (red), the 74-mode full ROM (black) for OASPL of 136dB

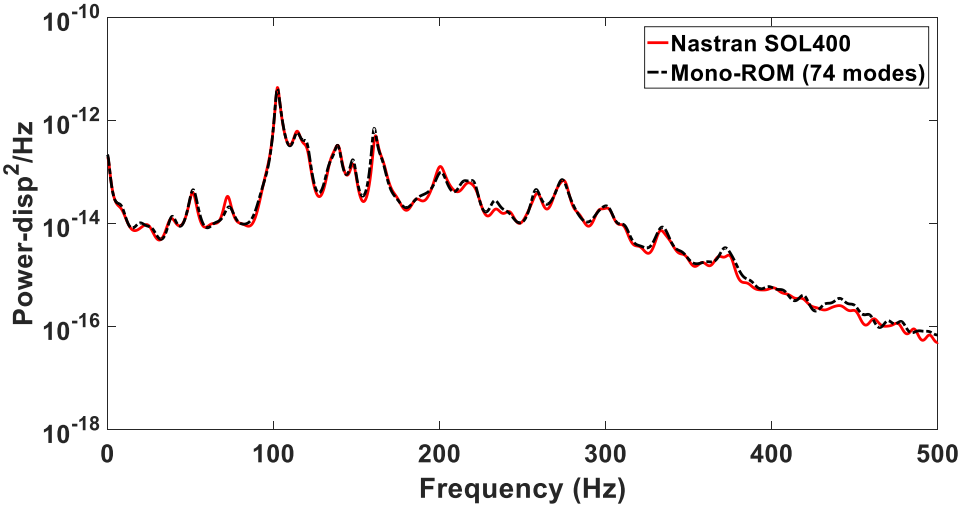

Figure 26 Power spectral densities of the in-plane (T1) responses of Panel 8 center obtained with Nastran SOL400 (red), the 74-mode full ROM (black) for OASPL of 136dB

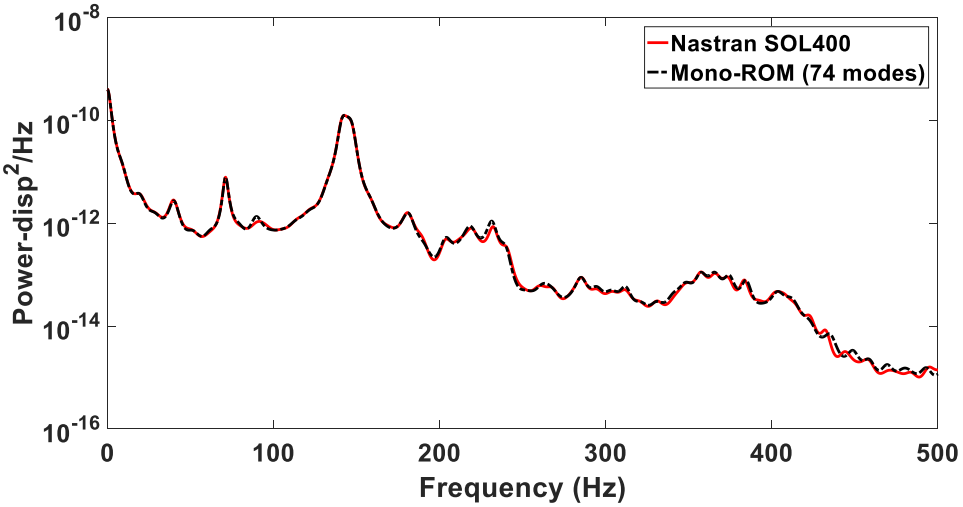

Figure 27 Power spectral densities of the in-plane (T2) responses of Panel 8 center obtained with Nastran SOL400 (red), the 74-mode full ROM (black) for OASPL of 136dB

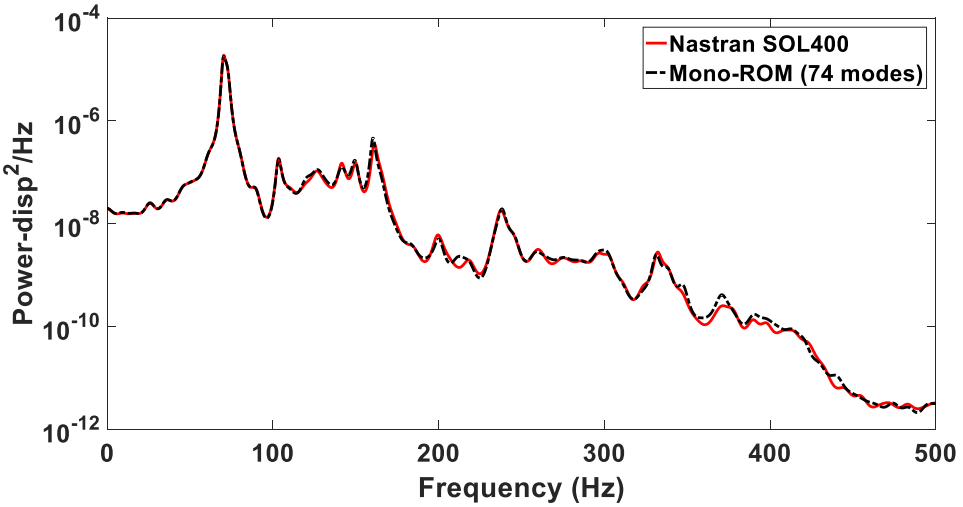

Figure 28 Power spectral densities of the transverse responses of Panel 9 center obtained with Nastran SOL400 (red), the 74-mode full ROM (black) for OASPL of 136dB

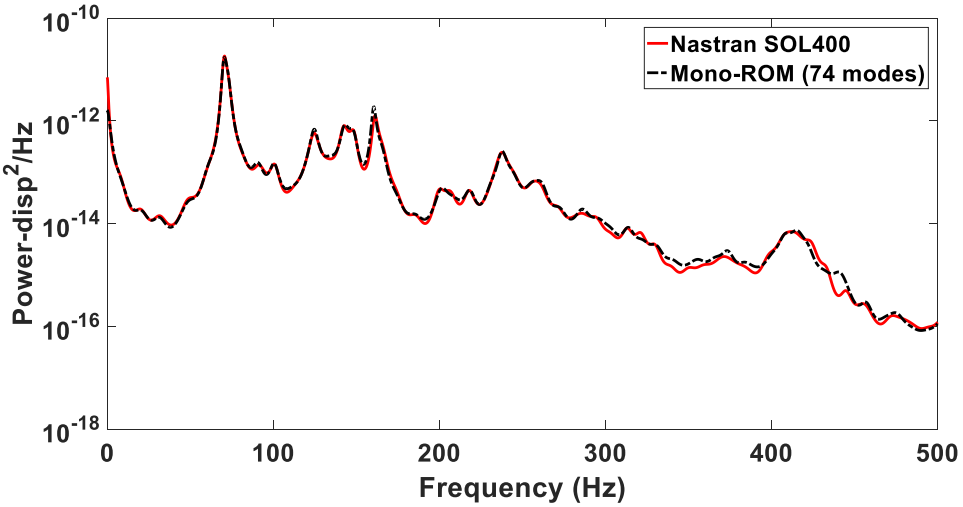

Figure 29 Power spectral densities of the in-plane (T1) responses of Panel 9 center obtained with Nastran SOL400 (red), the 74-mode full ROM (black) for OASPL of 136dB

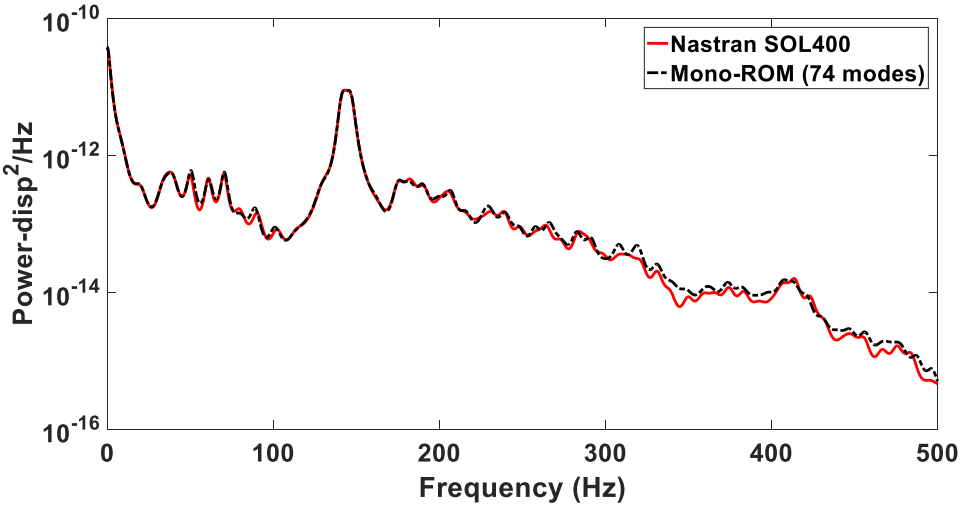

Figure 30 Power spectral densities of the in-plane (T2) responses of Panel 9 center obtained with Nastran SOL400 (red), the 74-mode full ROM (black) for OASPL of 136dB

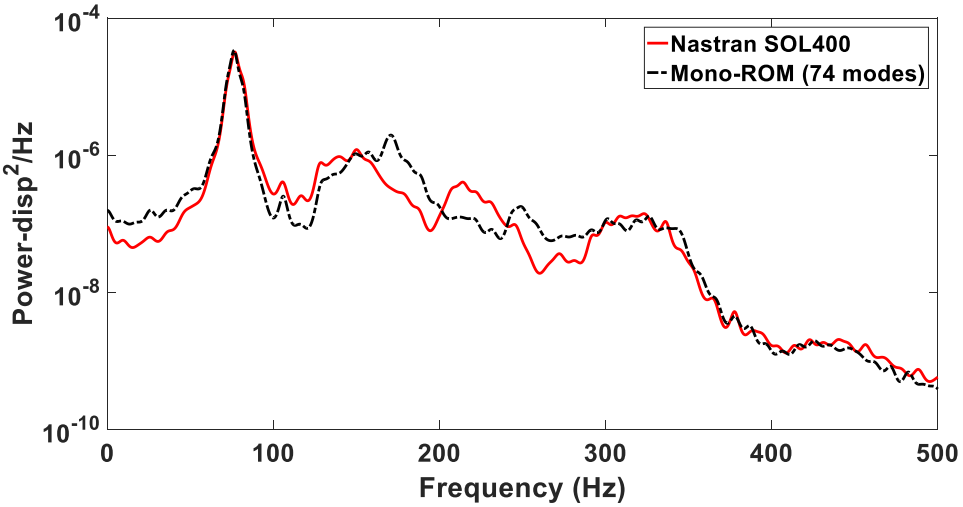

Figure 31 Power spectral densities of the transverse responses of Panel 1 center obtained with Nastran SOL400 (red), the 74-mode full ROM (black) for OASPL of 144dB

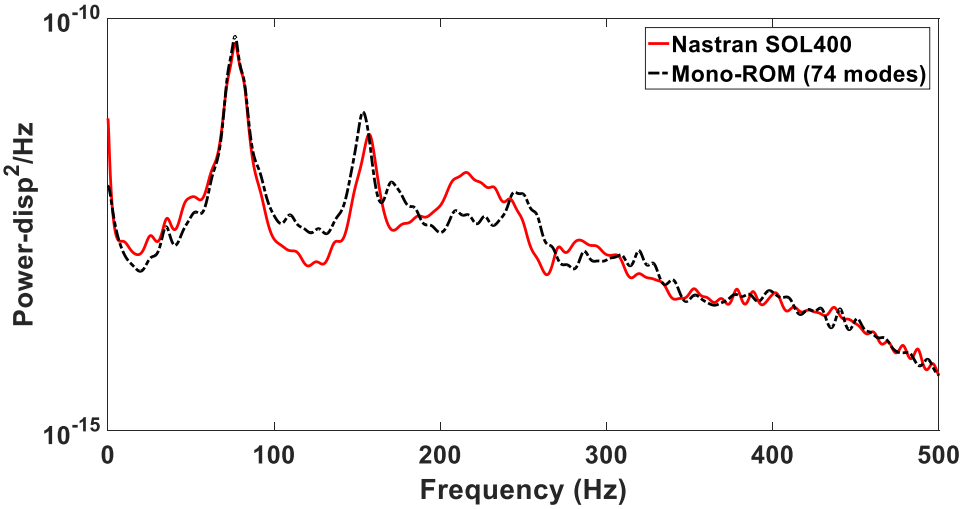

Figure 32 Power spectral densities of the in-plane (T1) responses of Panel 1 center obtained with Nastran SOL400 (red), the 74-mode full ROM (black) for OASPL of 144dB

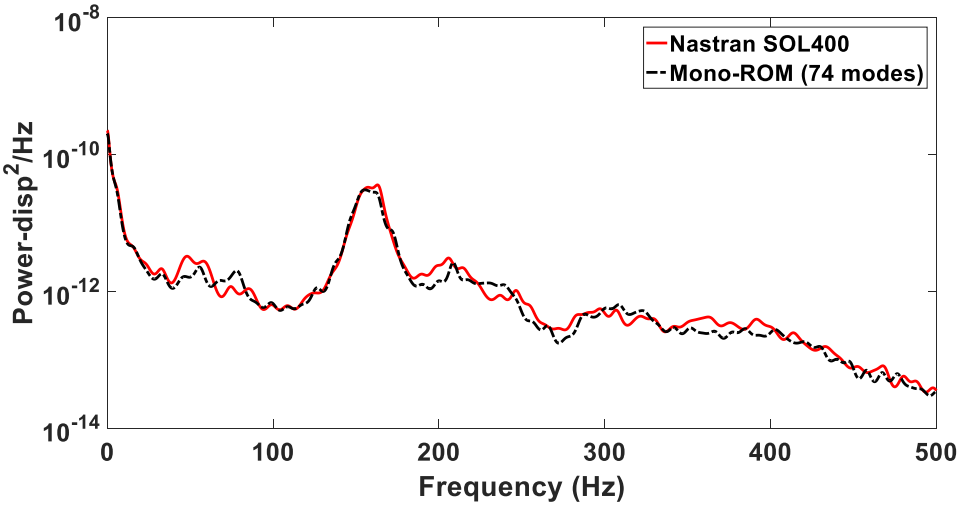

Figure 33 Power spectral densities of the in-plane (T2) responses of Panel 1 center obtained with Nastran SOL400 (red), the 74-mode full ROM (black) for OASPL of 144dB

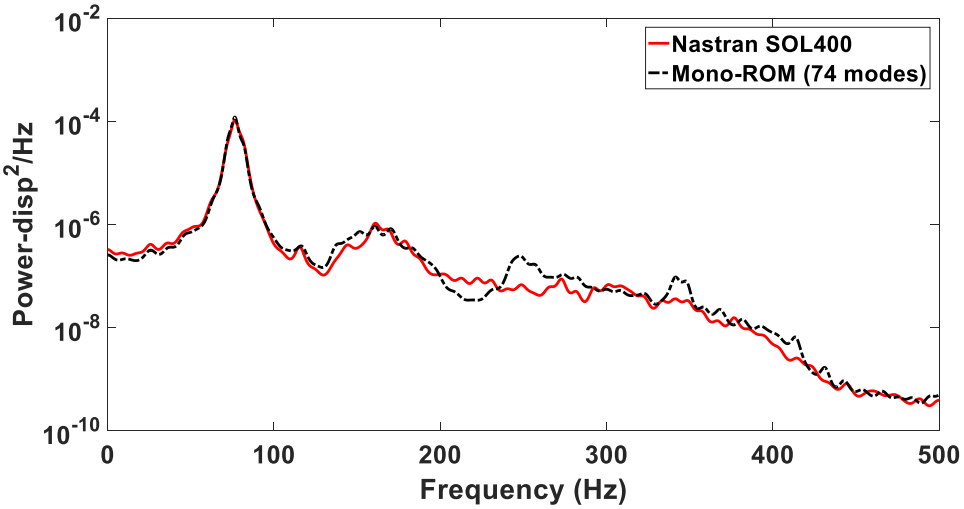

Figure 34 Power spectral densities of the transverse responses of Panel 2 center obtained with Nastran SOL400 (red), the 74-mode full ROM (black) for OASPL of 144dB

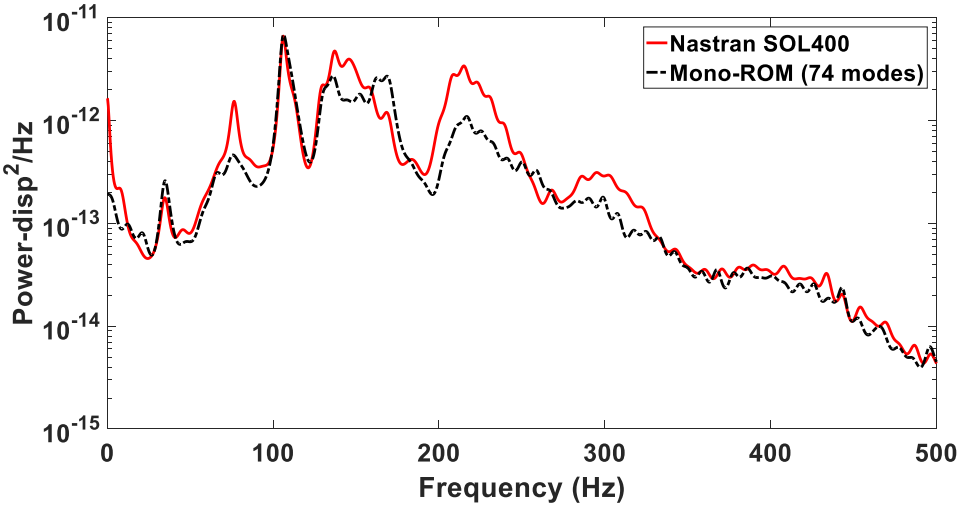

Figure 35 Power spectral densities of the in-plane (T1) responses of Panel 2 center obtained with Nastran SOL400 (red), the 74-mode full ROM (black) for OASPL of 144dB

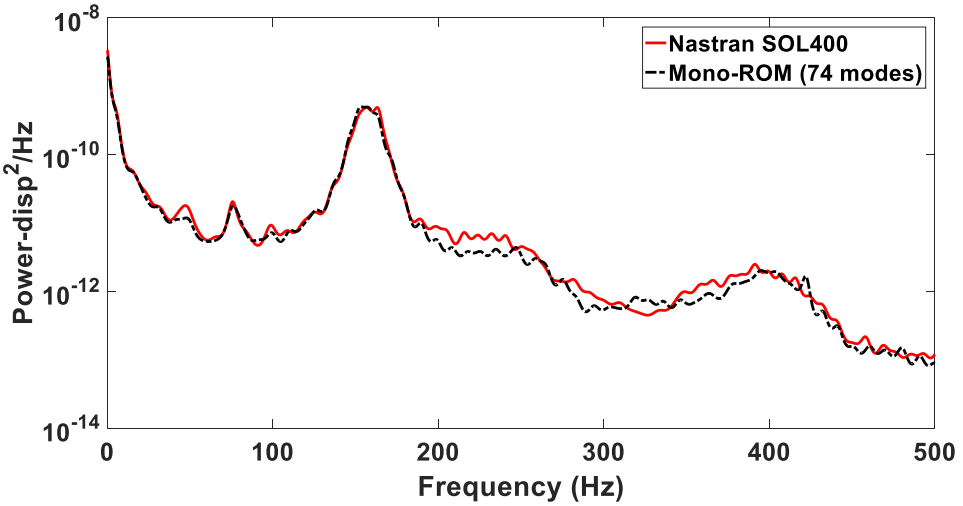

Figure 36 Power spectral densities of the in-plane (T2) responses of Panel 2 center obtained with Nastran SOL400 (red), the 74-mode full ROM (black) for OASPL of 144dB

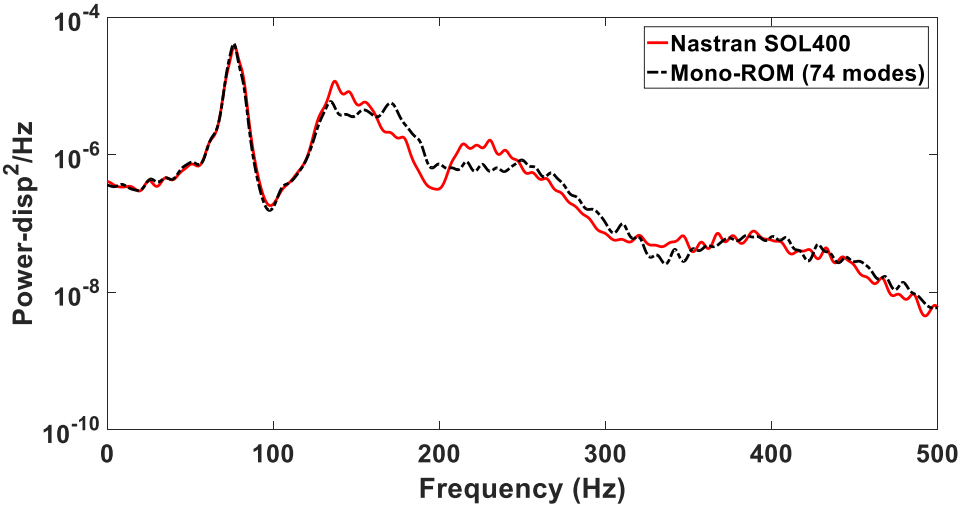

Figure 37 Power spectral densities of the transverse responses of Panel 3 center obtained with Nastran SOL400 (red), the 74-mode full ROM (black) for OASPL of 144dB

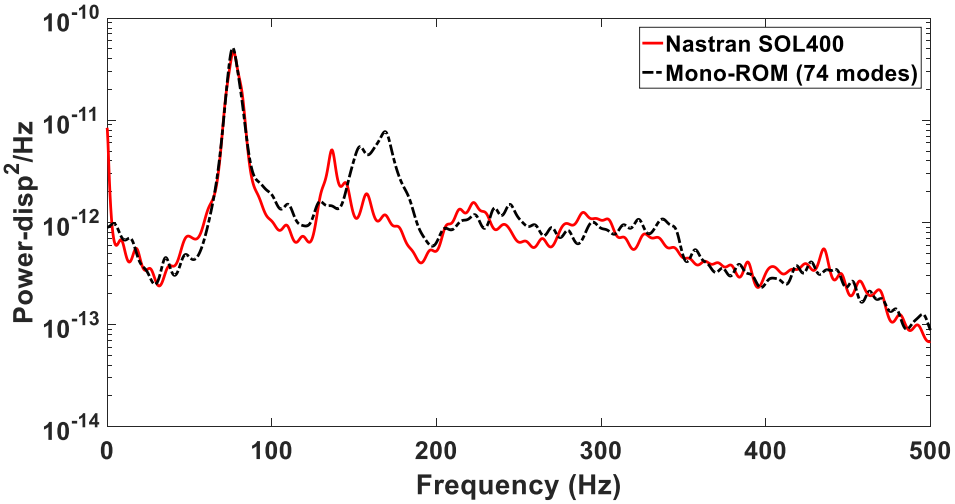

Figure 38 Power spectral densities of the in-plane (T1) responses of Panel 3 center obtained with Nastran SOL400 (red), the 74-mode full ROM (black) for OASPL of 144dB

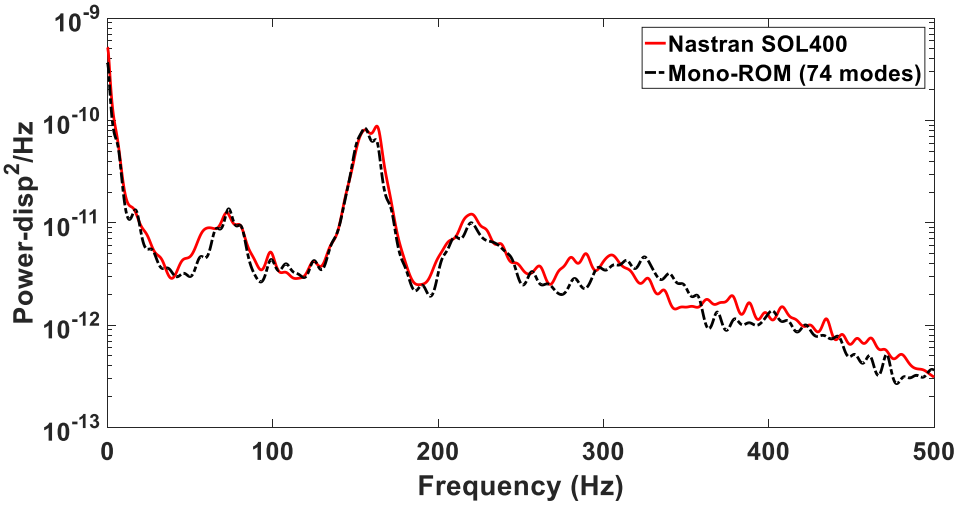

Figure 39 Power spectral densities of the in-plane (T2) responses of Panel 3 center obtained with Nastran SOL400 (red), the 74-mode full ROM (black) for OASPL of 144dB

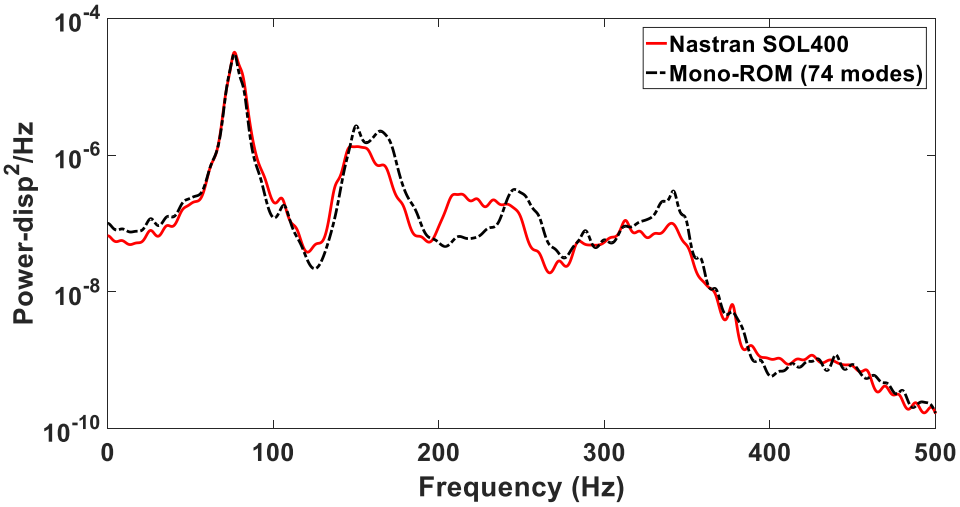

Figure 40 Power spectral densities of the transverse responses of Panel 4 center obtained with Nastran SOL400(red), the 74-mode full ROM (black) for OASPL of 144dB

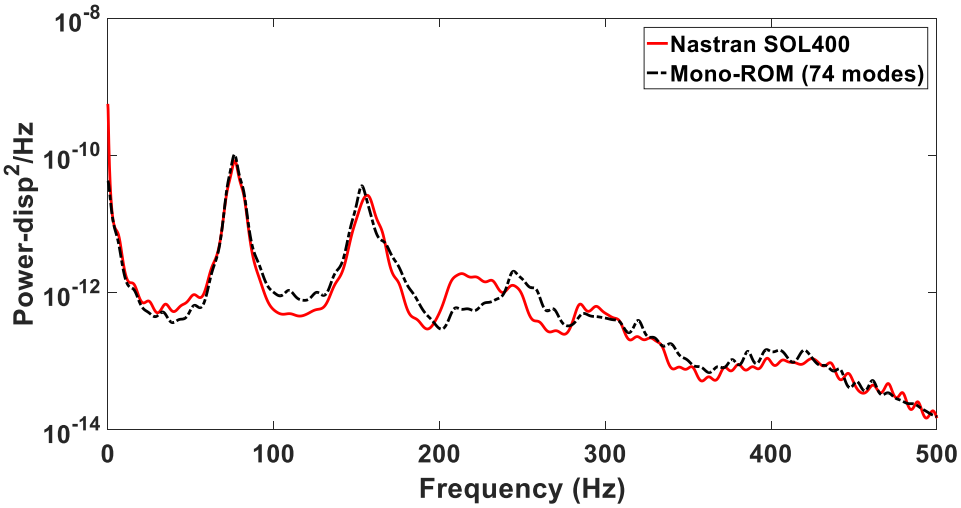

Figure 41 Power spectral densities of the in-plane (T1) responses of Panel 4 center obtained with Nastran SOL400 (red), the 74-mode full ROM (black) for OASPL of 144dB

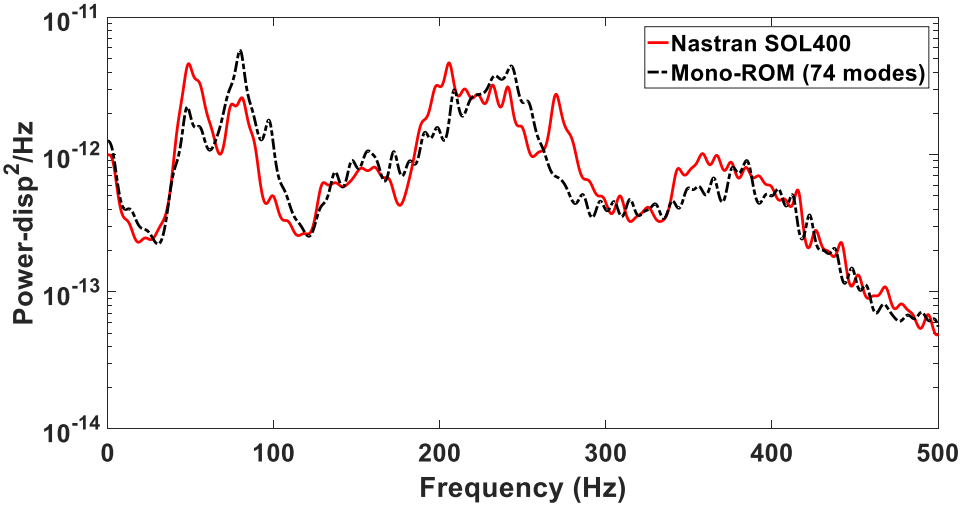

Figure 42 Power spectral densities of the in-plane (T2) responses of Panel 4 center obtained with Nastran SOL400 (red), the 74-mode full ROM (black) for OASPL of 144dB

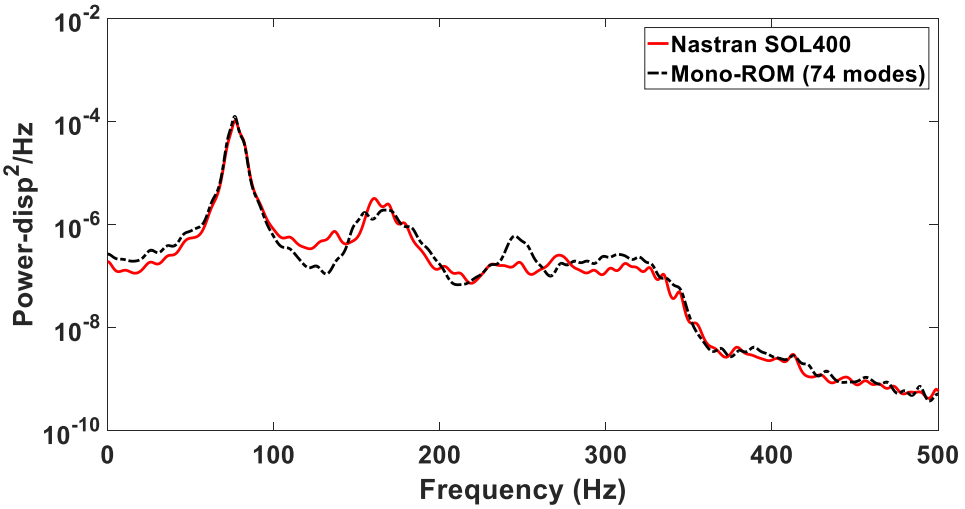

Figure 43 Power spectral densities of the transverse responses of Panel 5 center obtained with Nastran SOL400 (red), the 74-mode full ROM (black) for OASPL of 144dB

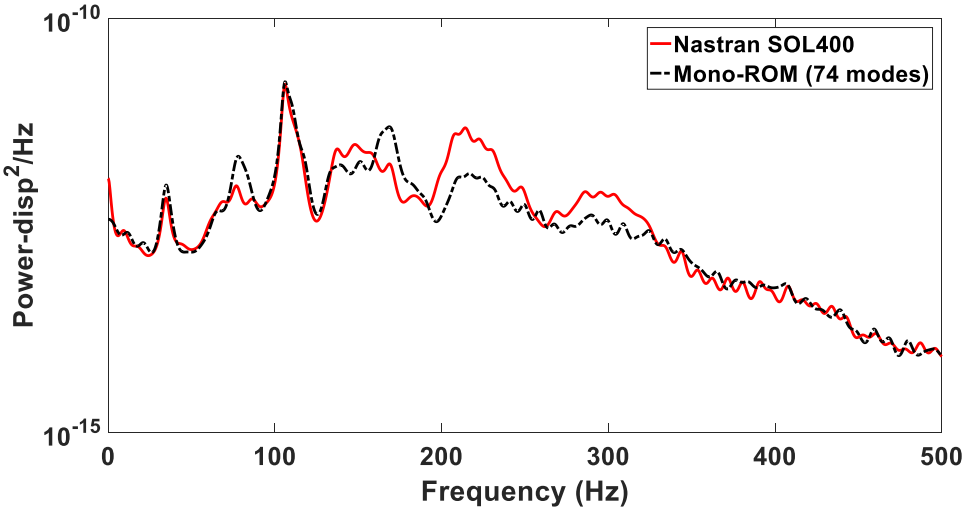

Figure 44 Power spectral densities of the in-plane (T1) responses of Panel 5 center obtained with Nastran SOL400 (red), the 74-mode full ROM (black) for OASPL of 144dB

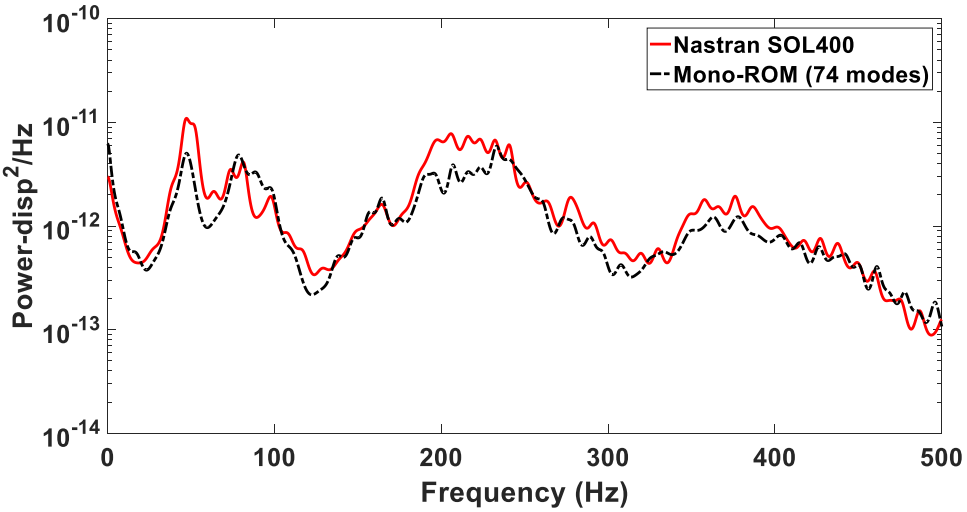

Figure 45 Power spectral densities of the in-plane (T2) responses of Panel 5 center obtained with Nastran SOL400 (red), the 74-mode full ROM (black) for OASPL of 144dB

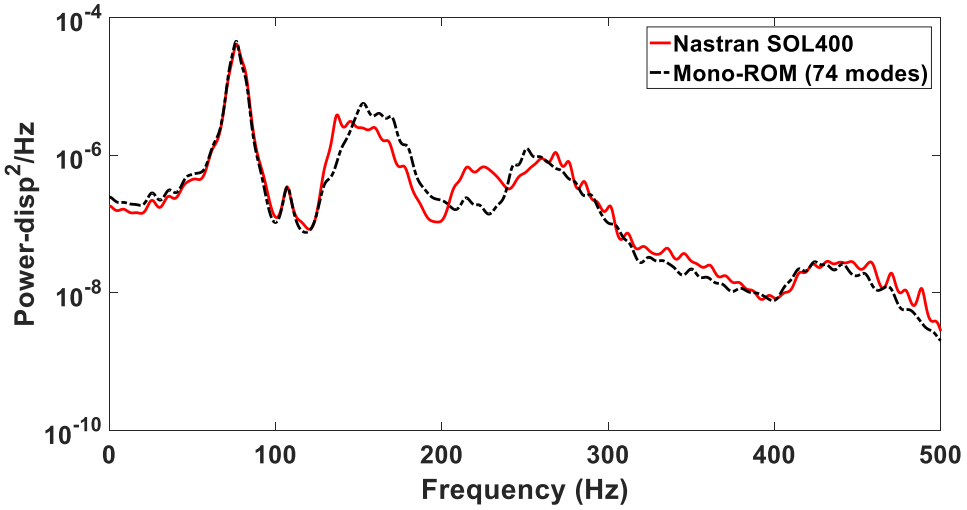

Figure 46 Power spectral densities of the transverse responses of Panel 6 center obtained with Nastran SOL400 (red), the 74-mode full ROM (black) for OASPL of 144dB

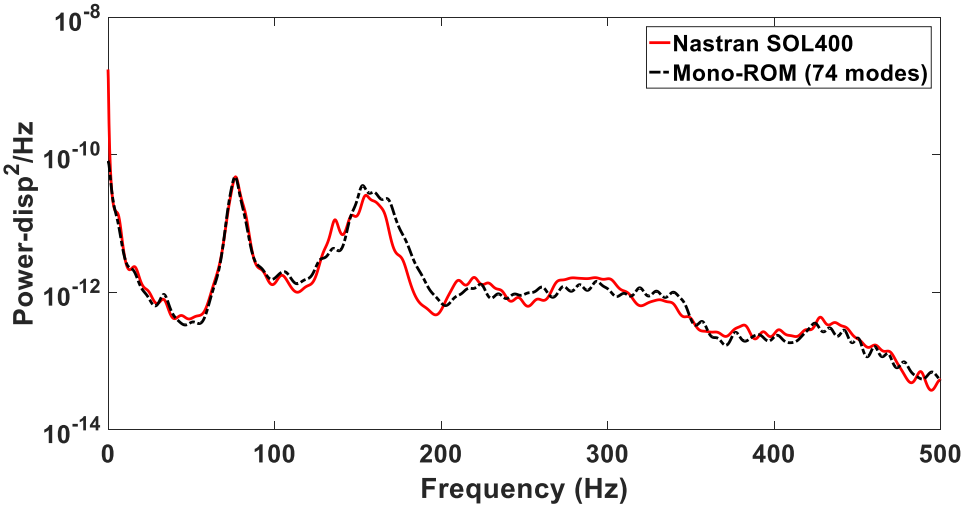

Figure 47 Power spectral densities of the in-plane (T1) responses of Panel 6 center obtained with Nastran SOL400 (red), the 74-mode full ROM (black) for OASPL of 144dB

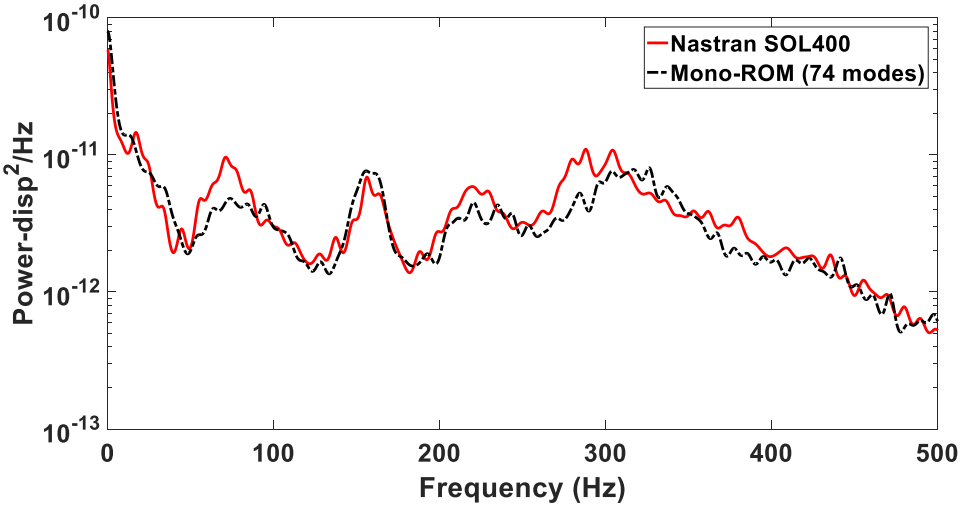

Figure 48 Power spectral densities of the in-plane (T2) responses of Panel 6 center obtained with Nastran SOL400 (red), the 74-mode full ROM (black) for OASPL of 144dB

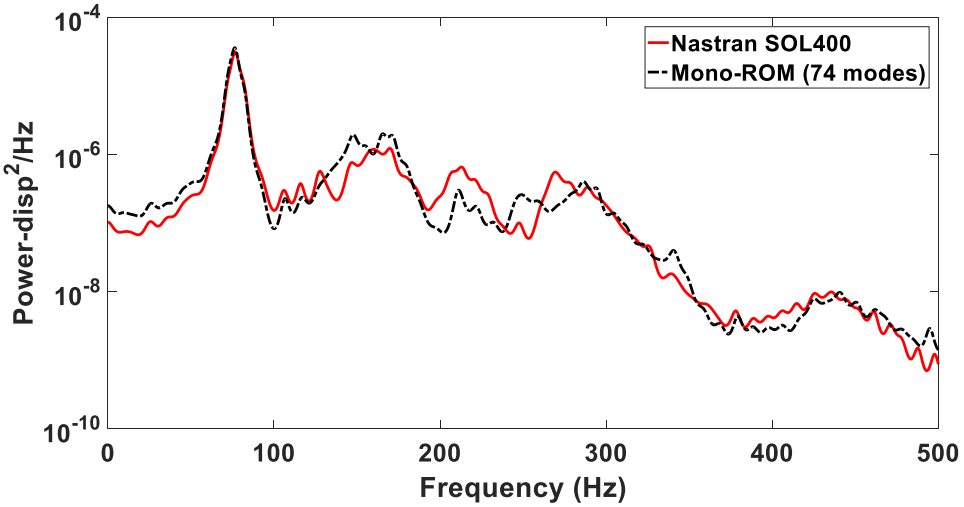

Figure 49 Power spectral densities of the transverse responses of Panel 7 center obtained with Nastran SOL400 (red), the 74-mode full ROM (black) for OASPL of 144dB

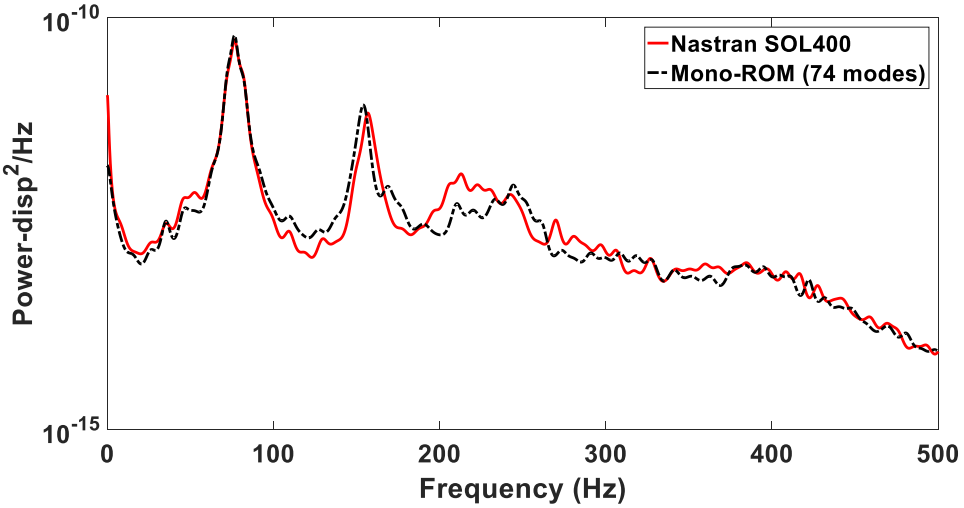

Figure 50 Power spectral densities of the in-plane (T1) responses of Panel 7 center obtained with Nastran SOL400 (red), the 74-mode full ROM (black) for OASPL of 144dB

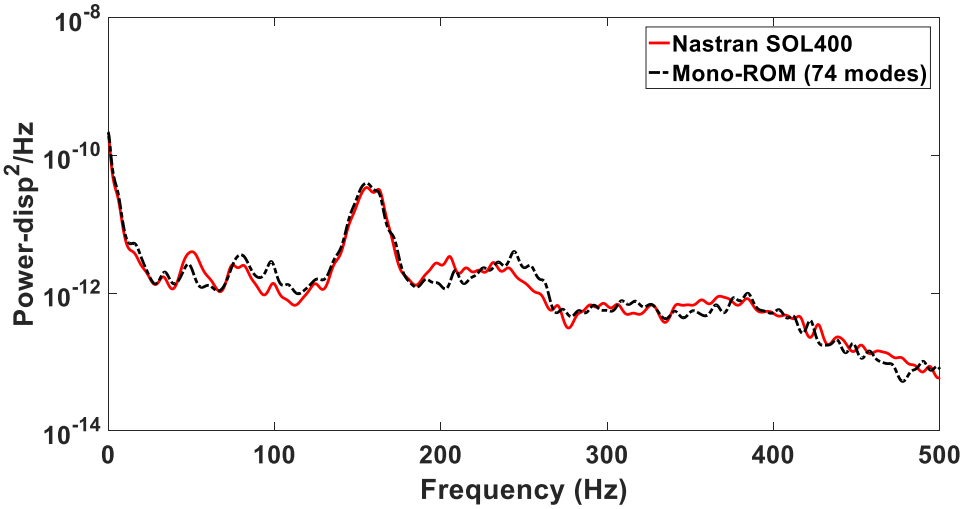

Figure 51 Power spectral densities of the in-plane (T2) responses of Panel 7 center obtained with Nastran SOL400 (red), the 74-mode full ROM (black) for OASPL of 144dB

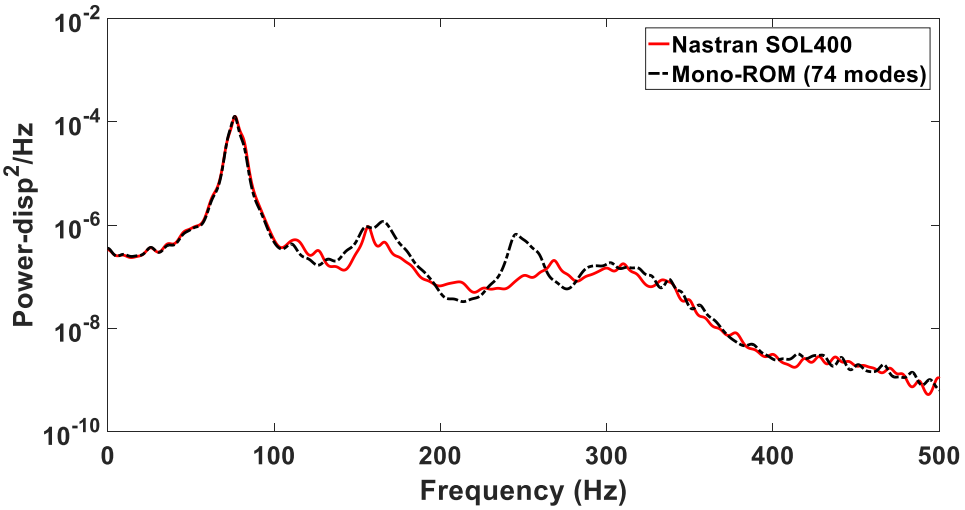

Figure 52 Power spectral densities of the transverse responses of Panel 8 center obtained with Nastran SOL400 (red), the 74-mode full ROM (black) for OASPL of 144dB

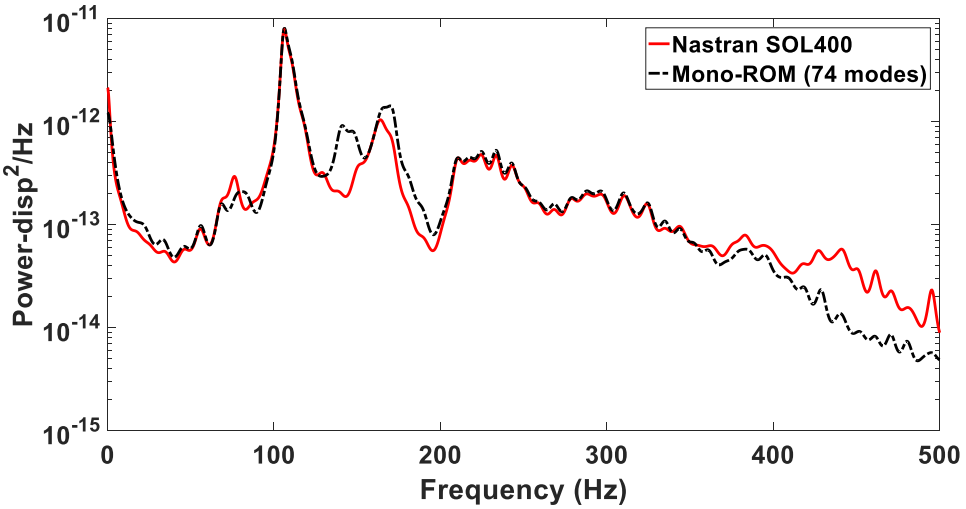

Figure 53 Power spectral densities of the in-plane (T1) responses of Panel 8 center obtained with Nastran SOL400 (red), the 74-mode full ROM (black) for OASPL of 144dB

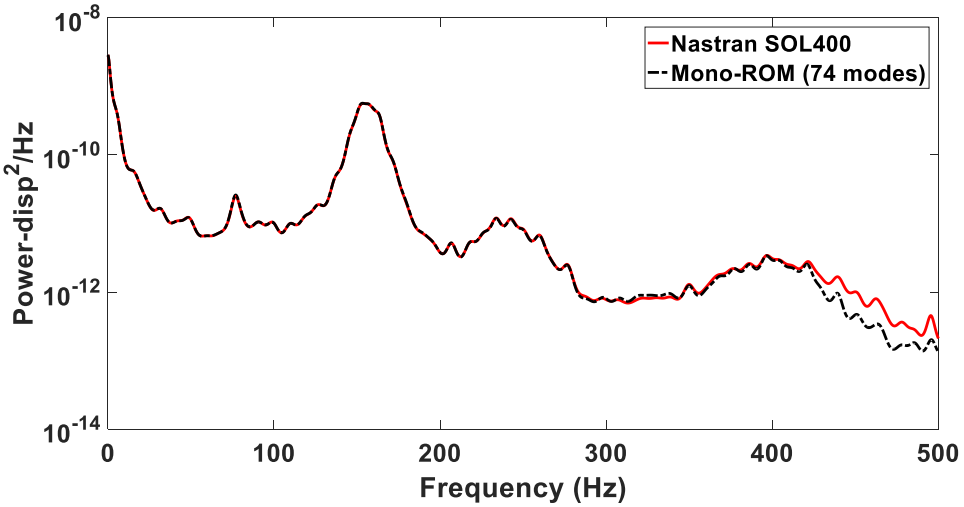

Figure 54 Power spectral densities of the in-plane (T2) responses of Panel 8 center obtained with Nastran SOL400 (red), the 74-mode full ROM (black) for OASPL of 144dB

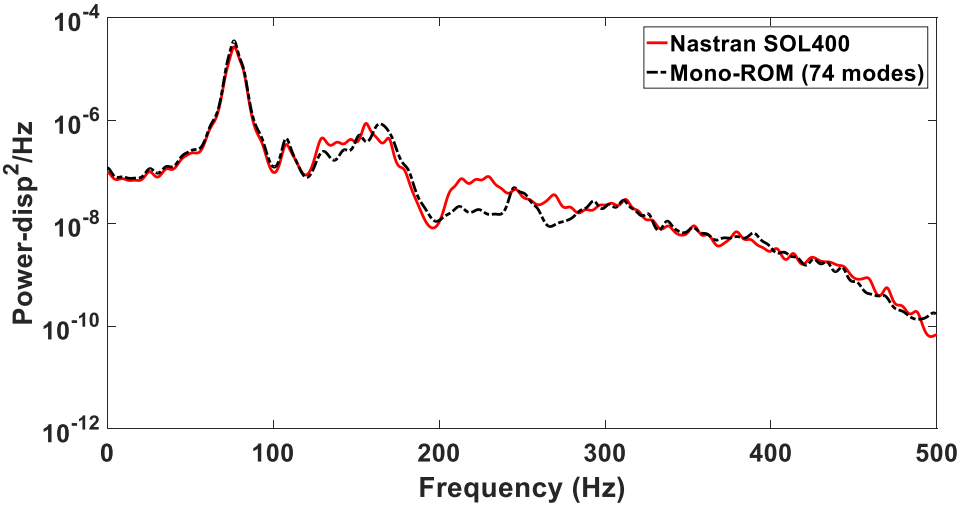

Figure 55 Power spectral densities of the transverse responses of Panel 9 center obtained with Nastran SOL400 (red), the 74-mode full ROM (black) for OASPL of 144dB

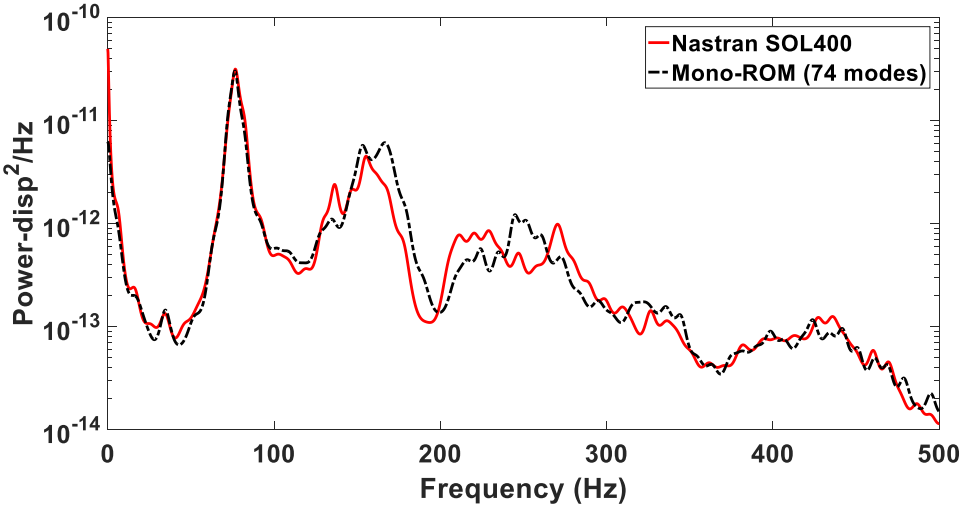

Figure 56 Power spectral densities of the in-plane (T1) responses of Panel 9 center obtained with Nastran SOL400 (red), the 74-mode full ROM (black) for OASPL of 144dB

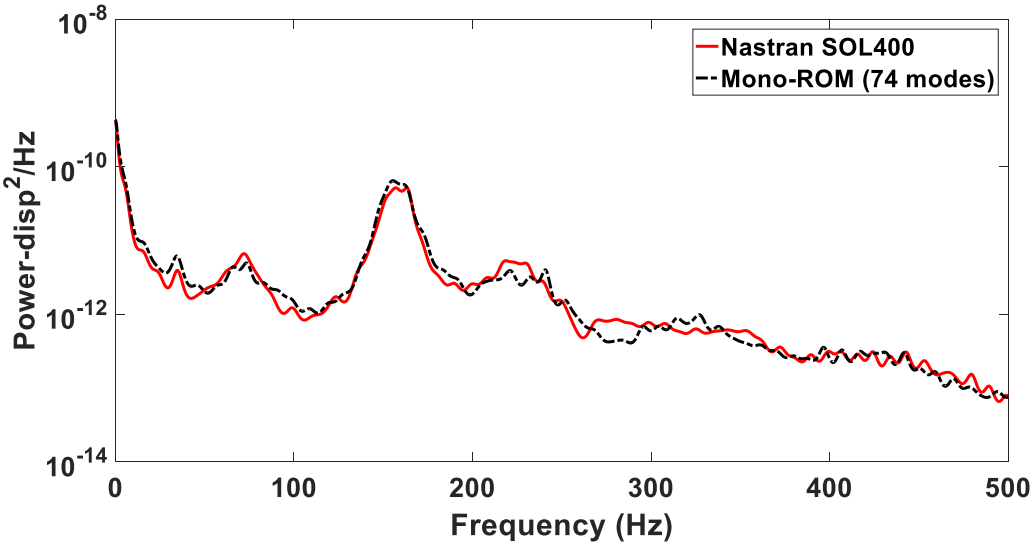

Figure 57 Power spectral densities of the in-plane (T2) responses of Panel 9 center obtained with Nastran SOL400 (red), the 74-mode full ROM (black) for OASPL of 144dB

3.3 A Simple Clamped-Clamped Beam Supported by Springs

A clamped-clamped beam supported by equal springs was also adopted as a simple validation case. The springs equally divide the beam into four bays (referred to as bay 1 to 4 from left to right) as shown in Fig. 58. In addition to the clamped-clamped boundary at both end, the out of plane translation and rotation degrees of freedom were also blocked for all nodes. The beam is made of isotropic elastic material with the following properties: Young's modulus (E) = 205MPa, Poisson's ratio (υ) = 0.3, density (ρ) = 1966.8 kg/m^3. The beam thickness is 7.75e-4 m and it is 0.2286 m long and 0.0127 m wide. The springs are identical with stiffness k = 200 N/m. The finite element model was developed in Nastran with the beam discretized with 40 identical CBEAM elements and 3 spring CELAS2 elements leading to 246 degrees of freedom. A Rayleigh damping model was adopted, i.e., $\boldsymbol{D} = a\boldsymbol{M} + b\boldsymbol{K}$, with a = 4.52/s and b = 1.71e-05s which leads to damping ratios of 1.12%, 1.00%, 0.93%, and 0.92% for the first 4 modes.

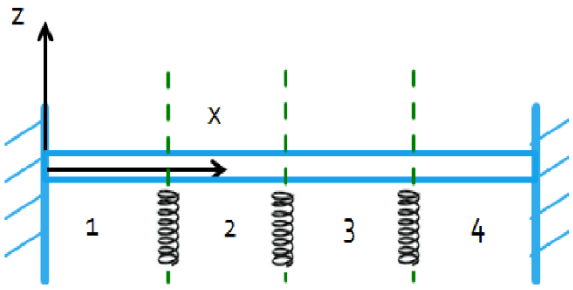

Figure 58 A simple clamped-clamped beam model supported by linear springs

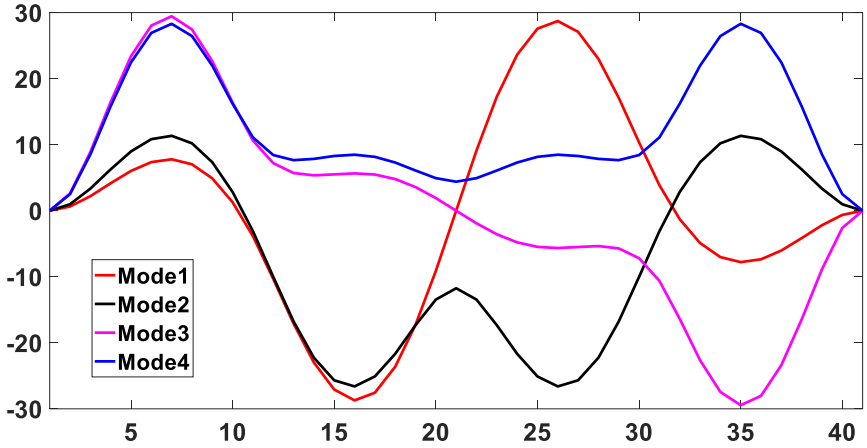

Figure 59 Lowest 4 linear modes of the beam model

The presence of the springs induces a partial localization of the linear modes to 1 or 2 of the bays, see Fig. 59, and the features of these modes are similar to those of the stiffened 9-bay panel. The natural frequencies of the linear modes are listed in Table 2 in increasing order.

Table 2

Natural Frequencies of the Beam (Hz)

39.659	48.454	59.480	59.829	101.507	116.772	147.569	162.198
170.136	208.846	252.104	302.704	340.535	345.951	406.402	468.658

3.4 Nonlinear ROM Construction for the Beam

The beam was assumed subjected to either static or dynamic loading, the latter varying with time as a white noise in the band [0,100] Hz. The spatial variation of the loading was selected as a linear combination of modes 1 to 4 leading to modal forces of 7.56e3,

0.89e3, 0.22e3, 0.22e3 on the mass normalized modes 1-4. This load distribution promotes a mode 1 response for simplicity.

Given the loading conditions and the natural frequencies, it would appear at first that the construction of the NLROM would be a straightforward task, based on 4 linear modes with mode 1 only dominant. However, the nonlinear response of the beam was found rather unexpectedly to exhibit two interesting features inherent of nonlinear problems which modified the basis selection. First, it was observed that mode 3 exhibits a much larger response for the nonlinear dynamic case than for its linear equivalent. Figure 60 compares the averaged values (from dynamic responses) of the modal responses of the linear modes for a peak response of 1 thickness from which it is clearly seen that the average modal response for the linear mode 3 almost equals that of the linear mode 1. Therefore, mode 3 needs also to be considered as a dominant mode in the dual mode computations. The second unexpected observation is that there exists a transfer energy from the excitation band [0,100] Hz band to the [200,300] Hz one (see Fig. 61, red solid curve) where higher order linear modes are excited. Thus, modes 5 - 8, 10 - 12, 14-16 and 21 were also added to the basis. Note that modes 9 and 13 are torsion dominant modes, thus, are not included in the basis.

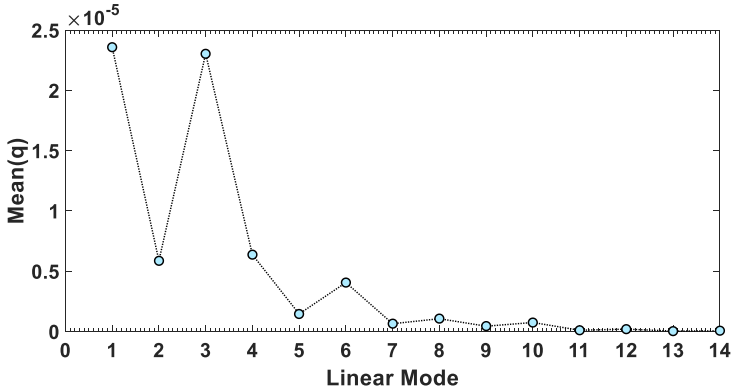

Figure 60 Averaged values of the modal coordinates for the linear modes

As a result, dual modes resulting from modes 1 and 3 alone and their combinations with other linear modes were added to the nonlinear ROM basis. In this light, 14 duals modes

were generated leading then to a 29-mode NLROM. This large number of modes is unusual for a structure of seemingly low complexity but it is a result of the nonlinear energy transfer mechanism. The final step of the 29-mode ROM construction is the identification of its linear, quadratic, and cubic stiffness coefficients which was achieved from the Nastran finite element model using the tangent stiffness imposed displacement approach (see [22]). In the sequel, this 29-mode ROM will be referred to as the full NLROM.

Its response will be used as the baseline for the assessment of the component-centric ROMs because some differences still exist at the high frequency ranges (i.e., [200,300] Hz for the transverse direction, [450,580] Hz for the in-plane direction) as shown in Fig. 61. Somewhat larger response in the high frequency range were obtained using the condensed ROM [31] as shown in Fig. 62. In fact, the condensed full ROM would provide the same results after setting the damping for the dual modes to zero. Therefore, the larger response was basically due to the "zero" damping on the in-plane motion.

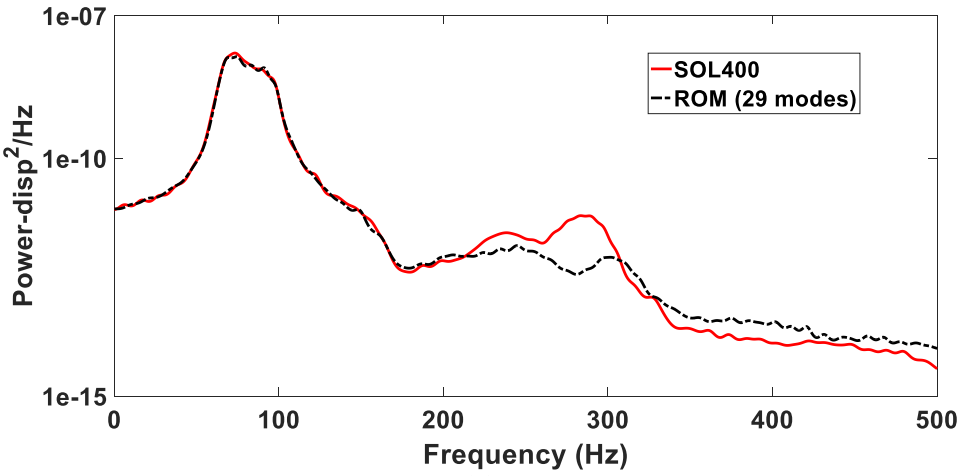

(a)

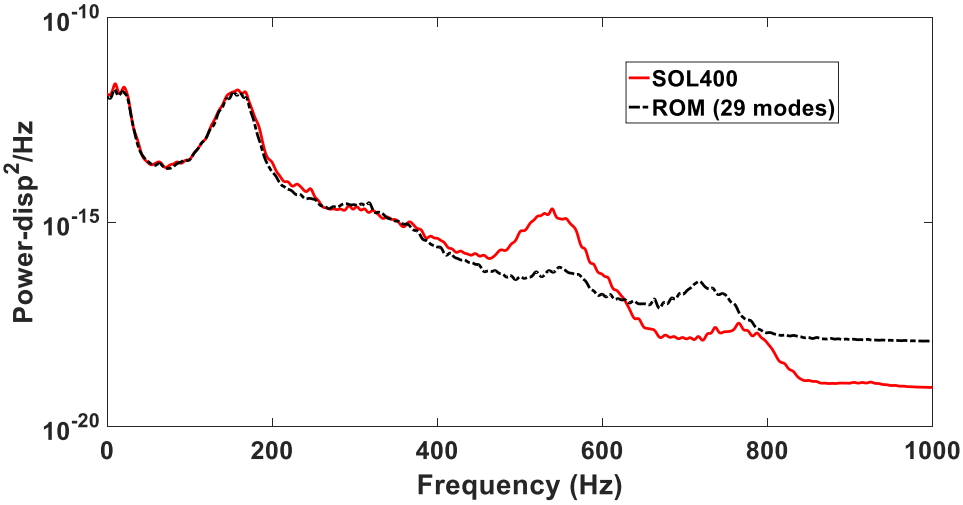

(b)

Figure 61 Power spectral density of the transverse (a) and in-plane (b) deflections at the node with max. disp. in the first bay

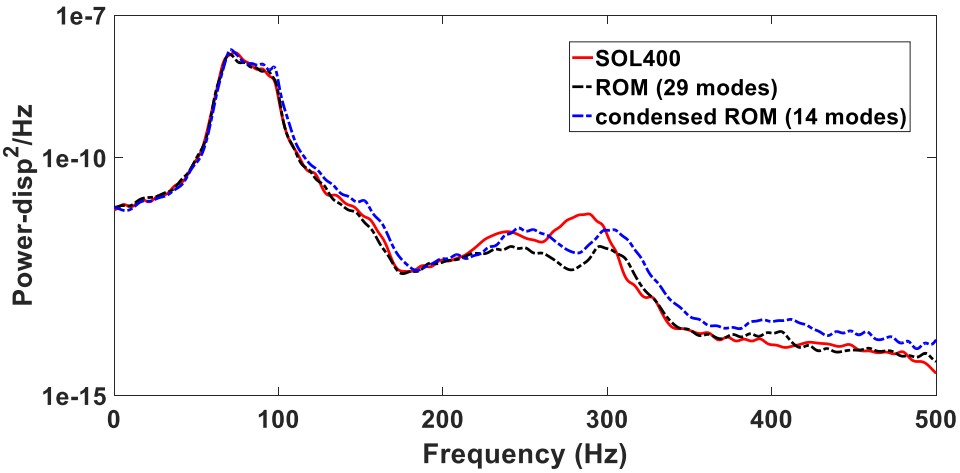

Figure 62 Power spectral density of the transverse deflection at the node with max. disp. in the first bay

3.5 Comparison of different FE Models and the ROM for the Beam

Since the observed out of band responses exhibited by the beam model could not be duplicated by the NLROM under any condition, it was questioned whether this issue could result from a difference in nonlinear modeling between NLROM and Nastran. To assess this possibility, finite element results were also obtained for this beam modeled in Abaqus, as well as in two in-house finite element codes from the US Air Force Research Lab. by Dr. Perez. Shown in Fig. 63 are the power spectral densities (PSD) of displacement responses at the node of maximum transverse in the first bay obtained

using the available finite element codes and the NLROM. It is seen that, the prediction obtained with the ROM matches well the FE code named "Gordon" [45], while those from Nastran SOL400, Abaqus and the corotational FE code [46] exhibit good agreements. The difference between the "Gordon" code and the corotational code is the use of the linear constitutive relation between the stress and the strain tensors. The "Gordon" code expresses the stress and strain tensors in the undeformed configurations:

$$S_{ij} = C_{ijkl} E_{kl} \tag{27}$$

as assumed in the NLROM formulation, Eq. (9). On the contrary, the corotational code assumes the formulation by assuming a similar relation between the corresponding deformed configuration tensors:

$$\sigma_{ij} = \hat{C}_{ijkl} e_{kl} \tag{28}$$

where $\boldsymbol{\sigma}$ and $\boldsymbol{e}$ are the Cauchy stress and Almansi strain tensors and $\widehat{\boldsymbol{C}}$ is also a fourth order elasticity tensor but dependent on the deformed coordinates $\underline{x}$. The undeformed stress and strain tensors are obtained from their deformed counterparts from the pull-back operations.

$$\begin{aligned} \boldsymbol{S} &= J\boldsymbol{F}^{-1}\boldsymbol{\sigma}\boldsymbol{F}^{-T} \\ \boldsymbol{E} &= \boldsymbol{F}^{T}\boldsymbol{e}\boldsymbol{F} \end{aligned} \tag{29}$$

where $\boldsymbol{F}$ is the deformation gradient tensor and J denotes the Jacobian of the transformation, i.e., J=det($\boldsymbol{F}$). Combining Eqs (27) -(29), it is readily seen that it is not possible for both Eqs (27) and (28) to hold independently of the deformations, i.e. of $\boldsymbol{F}$. Equivalently, the two linear elasticity definitions, Eqs. (27) and (28), are not compatible and different displacement fields will be obtained by assuming one or the other law. Since Eq. (27) is consistent with the derivation of the NLROM, the matching of the prediction from the NLROM with those from the "Gordon" code would be expected. The formulation for Abaqus is unknown so there is no conclusion drawn regarding its results.

The above discussion demonstrates that the differences between the Nastran results and their ROM counterpart could be attributed to the different assumptions made with regard to constitutive equation. Within the non-intrusive NLROM community focusing on panels and wings, this finding appears to be the first of its kind which is demonstrated.

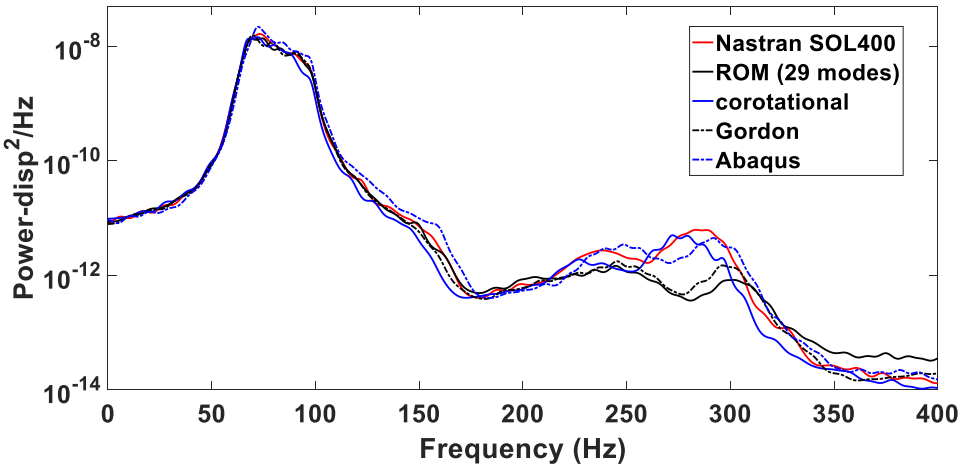

(a)

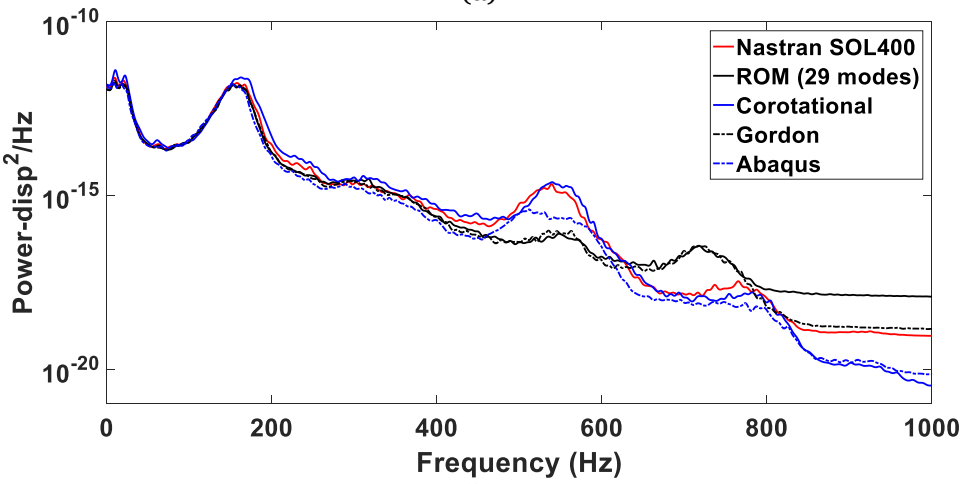

(b)

Figure 63 Power spectral density of the transverse (a) and in-plane (b) deflections at the node with max. disp. in the first bay with different FE models and the ROM

CHAPTER 4

LINEAR COMPONENT-CENTRIC ROM

This chapter focuses on the formulation and assessment of linear component-centric ROMs, i.e., those that provide a better approximation in the zone of interest (the β component) than the rest of it (the α component). Four different approaches will be presented. The validation, assessment, and comparison of these approaches will be carried out on the test structure, the modified NASA's 9-bay panel, the properties and response of which were described in Chapter 3.

4.1 Craig-Bampton Based Approaches

Since the structure will be decomposed into two parts, α and β, a Component Mode Synthesis framework seems appropriate as a way to emphasize the latter part over the former one. More specifically, the Craig-Bampton (CB) method is adopted here and, for completeness and notational convenience, is briefly reviewed below.

The equations of motion for the undamped substructure *s* (*s* representing either α or β) can be written as:

$$\widehat{\boldsymbol{M}}^s \underline{\ddot{u}}^s + \widehat{\boldsymbol{K}}^s \underline{u}^s = \underline{\hat{F}}^s \tag{30}$$

where $\widehat{\boldsymbol{M}}^{\boldsymbol{s}}$, $\widehat{\boldsymbol{K}}^{\boldsymbol{s}}$, $\underline{u}^{\boldsymbol{s}}$, and $\underline{\hat{F}}^s$ are, respectively, the mass and stiffness matrices and the displacement and force vector of the substructure in the physical coordinates. The mass and stiffness matrices can be partitioned as:

$$\widehat{\boldsymbol{M}}^s = \begin{bmatrix} \widehat{\boldsymbol{M}}_{ii} & \widehat{\boldsymbol{M}}_{ib} \\ \widehat{\boldsymbol{M}}_{bi} & \widehat{\boldsymbol{M}}_{bb} \end{bmatrix} \tag{31}$$

and

$$\widehat{\boldsymbol{K}}^s = \begin{bmatrix} \widehat{\boldsymbol{K}}_{ii} & \widehat{\boldsymbol{K}}_{ib} \\ \widehat{\boldsymbol{K}}_{bi} & \widehat{\boldsymbol{K}}_{bb} \end{bmatrix} \tag{32}$$

where the subscripts *i* and *b* correspond to the interior and boundary degrees of freedom of the substructure *s*. In the Craig-Bampton method, the internal ($\underline{u}_i^s$) and boundary ($\underline{u}_b$) displacement are represented as:

$$\underline{u_i^s} = \boldsymbol{\Phi}^s \underline{q_i^s} + \boldsymbol{\Xi}^s \underline{Y} \tag{33}$$

$$\underline{u_b} = \underline{Y} \tag{34}$$

where $\boldsymbol{\Phi}^s = \left[\underline{\phi}_1 \quad \underline{\phi}_2 \quad \cdots \quad \underline{\phi}_n\right]$ denotes a matrix of n selected *fixed interface* modes $\underline{\phi}_k$, i.e., with the boundary displacements set to zero. They are derived from the eigenvalue problem:

$$\widehat{\boldsymbol{K}}_{ii}^s \underline{\phi_j^s} = \lambda_j^s \widehat{\boldsymbol{M}}_{ii}^s \underline{\phi_j^s} \tag{35}$$

with λ_j^s representing the corresponding eigenvalue. Further, in Eq. (33), $\boldsymbol{\Xi}^s$ denotes the matrix of *constraint modes* which are determined as the static responses inside the substructure s corresponding to all boundary degrees of freedom set to zero except one of them in turn which is then set to a unit value. That is,

$$\boldsymbol{\Xi}^s = -\left(\widehat{\boldsymbol{K}}_{ii}^s\right)^{-1} \widehat{\boldsymbol{K}}_{ib}^s \tag{36}$$

Finally, the vector $\underline{q_i^s}$ of Eq. (33) contains the generalized coordinates of the fixed interface modes. Note in the above discussion that the boundary degrees of freedom are common to both substructures. The reduction of variables, from $(\underline{u_i^s}, \underline{u_b})$ to $(\underline{q_i^s}, \underline{Y})$, is accompanied by the transformation matrix:

$$\boldsymbol{T}^s = \begin{bmatrix} \boldsymbol{\Phi}^s & \boldsymbol{\Xi}^s \\ \boldsymbol{0} & \boldsymbol{I} \end{bmatrix} \tag{37}$$

where $\boldsymbol{I}$ denotes the identity matrix of appropriate dimensions. Then, the reduced CB mass and stiffness matrices can be obtained as:

$$\widetilde{\boldsymbol{M}}_{CB}^{s} = (\boldsymbol{T}^{s})^{T}\widehat{\boldsymbol{M}}^{s}\boldsymbol{T}^{s} = \begin{bmatrix} \widetilde{\boldsymbol{M}}_{qq} & \widetilde{\boldsymbol{M}}_{qY} \\ \widetilde{\boldsymbol{M}}_{Yq} & \widetilde{\boldsymbol{M}}_{YY} \end{bmatrix} \tag{38}$$

$$\widetilde{\boldsymbol{K}}_{CB}^{s} = (\boldsymbol{T}^{s})^{T}\widehat{\boldsymbol{K}}^{s}\boldsymbol{T}^{s} = \begin{bmatrix} \widetilde{\boldsymbol{K}}_{qq} & \boldsymbol{0} \\ \boldsymbol{0} & \widetilde{\boldsymbol{K}}_{YY} \end{bmatrix} \tag{39}$$

Note further that both $\widetilde{\boldsymbol{K}}_{qq}$ and $\widetilde{\boldsymbol{M}}_{qq}$ are diagonal and the ratios of their components are the eigenvalues of the fixed-interface problem. Considering the two substructures, the overall equations of motion of the undamped structure are

$$\begin{bmatrix} \widetilde{\boldsymbol{M}}_{qq}^{\alpha} & \widetilde{\boldsymbol{M}}_{qY}^{\alpha} & \boldsymbol{0} \\ \widetilde{\boldsymbol{M}}_{Yq}^{\alpha} & \widetilde{\boldsymbol{M}}_{YY} & \widetilde{\boldsymbol{M}}_{Yq}^{\beta} \\ \boldsymbol{0} & \widetilde{\boldsymbol{M}}_{qY}^{\beta} & \widetilde{\boldsymbol{M}}_{qq}^{\beta} \end{bmatrix} \begin{bmatrix} \ddot{\underline{q}}_{i}^{\alpha} \\ \ddot{\underline{Y}} \\ \ddot{\underline{q}}_{i}^{\beta} \end{bmatrix} + \begin{bmatrix} \widetilde{\boldsymbol{K}}_{qq}^{\alpha} & \boldsymbol{0} & \boldsymbol{0} \\ \boldsymbol{0} & \widetilde{\boldsymbol{K}}_{YY} & \boldsymbol{0} \\ \boldsymbol{0} & \boldsymbol{0} & \widetilde{\boldsymbol{K}}_{qq}^{\beta} \end{bmatrix} \begin{bmatrix} \underline{q}_{i}^{\alpha} \\ \underline{Y} \\ \underline{q}_{i}^{\beta} \end{bmatrix} = \begin{bmatrix} \underline{\tilde{F}}_{\boldsymbol{i}}^{\boldsymbol{\alpha}} \\ \underline{\tilde{F}}_{\boldsymbol{b}} \\ \underline{\tilde{F}}_{\boldsymbol{i}}^{\boldsymbol{\beta}} \end{bmatrix} \tag{40}$$

A more complete reduction can be performed by expressing the physical degrees of freedom at the interface in terms of a set of modes $\underline{\Psi}_{r}$ referred to as the characteristic constraint modes [37, 47] i.e.,:

$$\underline{Y} = \boldsymbol{\Psi}\underline{z} \tag{41}$$

where $\boldsymbol{\Psi} = [\underline{\Psi}_{1} \quad \underline{\Psi}_{2} \quad \cdots \quad \underline{\Psi}_{r}]$, with each column computed from the general eigen-value problems:

$$\widetilde{\boldsymbol{K}}_{YY}\underline{\Psi}_{j} = \lambda_{j}\widetilde{\boldsymbol{M}}_{YY}\underline{\Psi}_{j} \tag{42}$$

The following transformation matrix allows a second reduction of the degrees of freedom:

$$\boldsymbol{T_2} = \begin{bmatrix} \boldsymbol{I} & \boldsymbol{0} \\ \boldsymbol{0} & \boldsymbol{\Psi} \end{bmatrix} \tag{43}$$

The mass and stiffness matrices can be further reduced as:

$$\breve{\boldsymbol{M}}_{CB}^{s} = (\boldsymbol{T_2})^{T}\widetilde{\boldsymbol{M}}_{CB}^{s}\boldsymbol{T_2} = \begin{bmatrix} \breve{\boldsymbol{M}}_{qq} & \breve{\boldsymbol{M}}_{qz} \\ \breve{\boldsymbol{M}}_{zq} & \breve{\boldsymbol{M}}_{zz} \end{bmatrix} \tag{44}$$

$$\breve{\boldsymbol{K}}_{CB}^{s} = (\boldsymbol{T_2})^{T}\widetilde{\boldsymbol{K}}_{CB}^{s}\boldsymbol{T_2} = \begin{bmatrix} \breve{\boldsymbol{K}}_{qq} & \boldsymbol{0} \\ \boldsymbol{0} & \breve{\boldsymbol{K}}_{zz} \end{bmatrix} \tag{45}$$

Therefore, the overall equations of motion become:

$$\begin{bmatrix} \breve{\boldsymbol{M}}_{qq}^{\alpha} & \breve{\boldsymbol{M}}_{qz}^{\alpha} & \mathbf{0} \\ \breve{\boldsymbol{M}}_{zq}^{\alpha} & \breve{\boldsymbol{M}}_{zz} & \breve{\boldsymbol{M}}_{zq}^{\beta} \\ \mathbf{0} & \breve{\boldsymbol{M}}_{qz}^{\beta} & \breve{\boldsymbol{M}}_{qq}^{\beta} \end{bmatrix} \begin{bmatrix} \ddot{\underline{q}}_i^{\alpha} \\ \ddot{\underline{z}} \\ \ddot{\underline{q}}_i^{\beta} \end{bmatrix} + \begin{bmatrix} \breve{\boldsymbol{K}}_{qq}^{\alpha} & \mathbf{0} & \mathbf{0} \\ \mathbf{0} & \breve{\boldsymbol{K}}_{zz} & \mathbf{0} \\ \mathbf{0} & \mathbf{0} & \breve{\boldsymbol{K}}_{qq}^{\beta} \end{bmatrix} \begin{bmatrix} \underline{q}_i^{\alpha} \\ \underline{z} \\ \underline{q}_i^{\beta} \end{bmatrix} = \begin{bmatrix} \underline{\tilde{F}}_{\boldsymbol{i}}^{\boldsymbol{\alpha}} \\ \underline{\breve{F}}_{\boldsymbol{b}} \\ \underline{\tilde{F}}_{\boldsymbol{i}}^{\boldsymbol{\beta}} \end{bmatrix} \tag{46}$$

The CB modeling approach was investigated with various numbers of fixed interface and characteristic constraint modes for the 9-bay panel. This effort eventually led to the selection of 6 β-fixed interface modes, 28 characteristic constraint modes and 200 α-fixed interface modes, the predictions from which match well with the baseline (see Fig. 64). This model later will be used for the construction of component-centric ROMs. A known aspect of the CB method, i.e., Eqs (33) and (34), even after proper reduction[37, 47] , of Eq. (41), is the much larger size of the reduced model as compared to the linear modes, primarily due to the often large number of boundary degrees of freedom (see Fig. 65). To avoid its pitfall of a large number of generalized coordinates, it is proposed here to develop ROM-based "top-down" approaches. Two different secondary reductions are discussed in the ensuing sections.

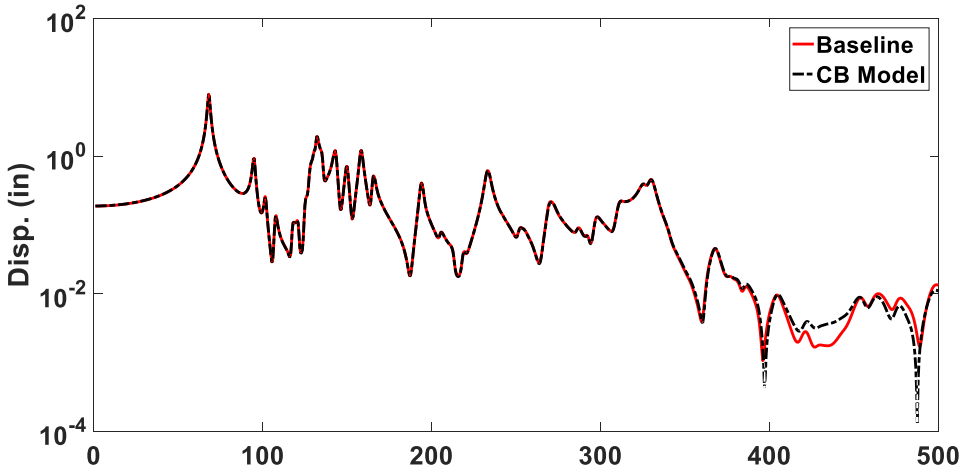

Figure 64 Magnitude of the frequency responses at the middle point of Bay 4, transverse displacement

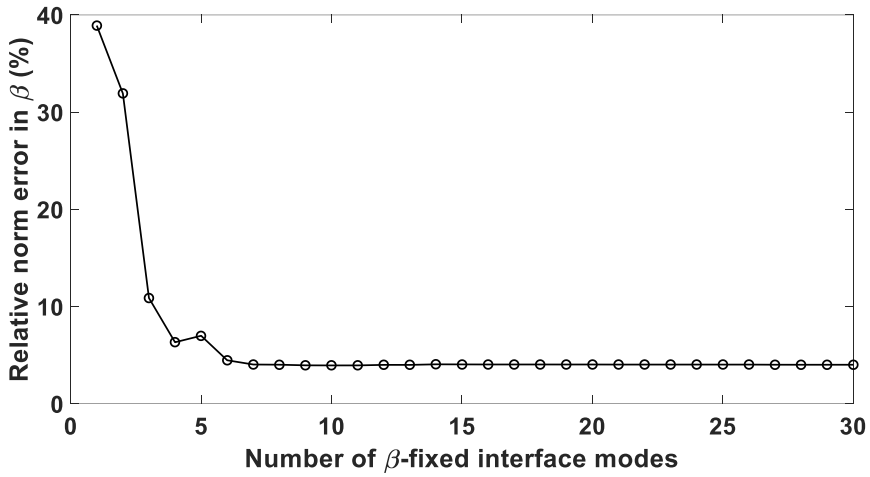

(a)

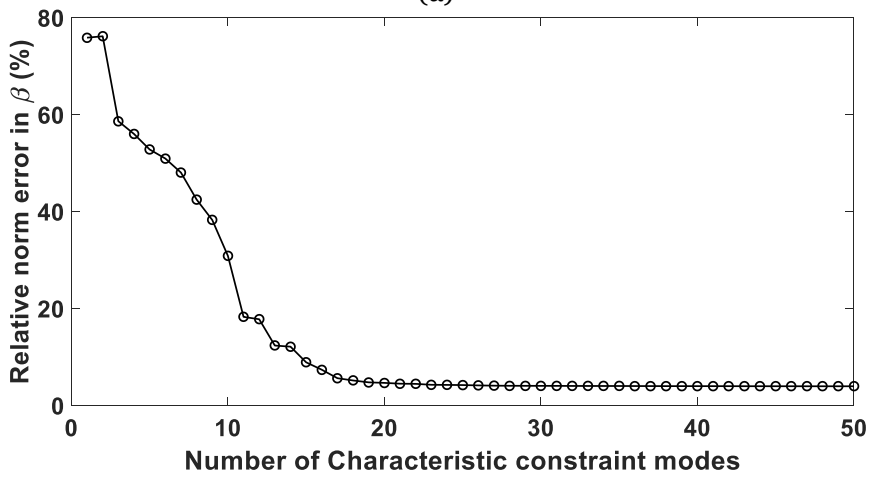

(b)

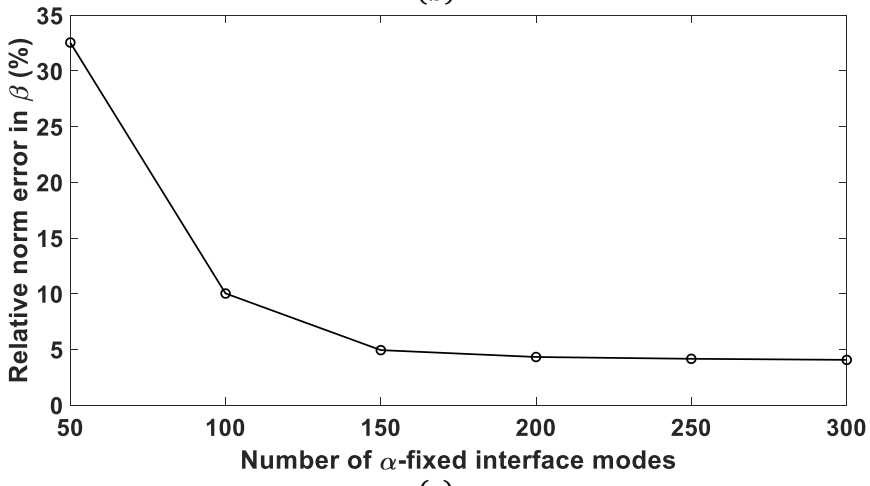

(c)

Figure 65 Convergence study for the β-fixed interface modes (a), characteristic constraint modes (b) and α-fixed interface modes (c)

4.1.1 ROMs Based on β-Fixed Interface and α-POD Modes

A potential improvement of this situation may result here from the condition that only the β component needs to be modeled accurately. Then, the mode reduction should extract only the modes in α that have significant effects on the response in the β component. Given reciprocity, these modes can be obtained as the responses in α due to imposed β motions. With that perspective, the modal basis was determined as follows:
(i) the fixed interface modes of the β component were assumed to vary harmonically one at a time and for all frequencies in the range of interest,
(ii) the damped response of the α component and the boundary were determined from Eq. (46) without additional forces on them, i.e.,
(iii) a Proper Orthogonal Decomposition (POD) analysis of the responses obtained in (ii) was carried out to extract the dominant components (see [48] for a recent review), and finally
(iv) the component-centric ROM was built with the fixed interface modes of the β component (referred to as "β-fixed") and the POD modes for α and the boundary (referred to as "α-POD").

$$\begin{bmatrix} \breve{\boldsymbol{M}}_{qq}^{\alpha} & \breve{\boldsymbol{M}}_{qz}^{\alpha} \\ \breve{\boldsymbol{M}}_{zq}^{\alpha} & \breve{\boldsymbol{M}}_{zz} \end{bmatrix} \begin{bmatrix} \ddot{\underline{q}}_i^{\alpha} \\ \ddot{\underline{z}} \end{bmatrix} + \begin{bmatrix} \boldsymbol{C}_{qq}^{\alpha} & \boldsymbol{C}_{qz}^{\alpha} \\ \boldsymbol{C}_{zq}^{\alpha} & \boldsymbol{C}_{zz} \end{bmatrix} \begin{bmatrix} \dot{\underline{q}}_i^{\alpha} \\ \dot{\underline{z}} \end{bmatrix} + \begin{bmatrix} \boldsymbol{k}_{qq}^{\alpha} & \boldsymbol{0} \\ \boldsymbol{0} & \boldsymbol{k}_{zz} \end{bmatrix} \begin{bmatrix} \underline{q}_i^{\alpha} \\ \underline{z} \end{bmatrix} = \begin{bmatrix} \boldsymbol{0} \\ -\boldsymbol{M}_{Yq}^{\beta} \ddot{\underline{q}}_i^{\beta} \end{bmatrix} \qquad (47)$$

Note that the singular value decomposition (SVD) was used for all POD analyses to avoid the loss of precision when forming the covariance matrix. Therefore, the POD modes are computed by performing an SVD on the matrix of snapshot data. The assessment of the above procedure was carried out by first comparing the magnitude of the frequency response of the β components to its baseline. Figure 66 provides this comparison at the middle point of the β component with 6 β-fixed and 30 α-POD modes. The excellent matching with the baseline curve indicates that this method does provide a good prediction of the response in the β component with enough α-POD modes.

To obtain a more global representation of the matching over the two components, a representation error was defined as

$$representation\ error = \frac{norm_{L_2}\ of\ response\ error}{norm_{L_2}\ of\ response} \times maximum\ response \qquad (48)$$

which is computed in both components (α and β) and at each frequency. Shown in Fig. 67 are the representation errors in α and β components with the 6 β-fixed and 30 α-POD modes component-centric ROM. They confirm the good match seen in Fig. 66 and demonstrate that the modeling of the β component is better than the one for the α component as could be expected. However, 36 modes are necessary while a similar prediction can already be achieved with as few as 21 linear modes (see section 4.4). Moreover, reducing the number of α-POD modes degrades rapidly the accuracy: the ROM built with 6 β-fixed and 20 α-POD modes fails to capture some of the peaks, see Fig. 68. The need for a large number of α-POD modes is again verified by the slow decrease of the representation errors in Fig. 69. It is concluded that this method provides a good matching of the response in the β component but does not appear to lead to a very compact ROM.

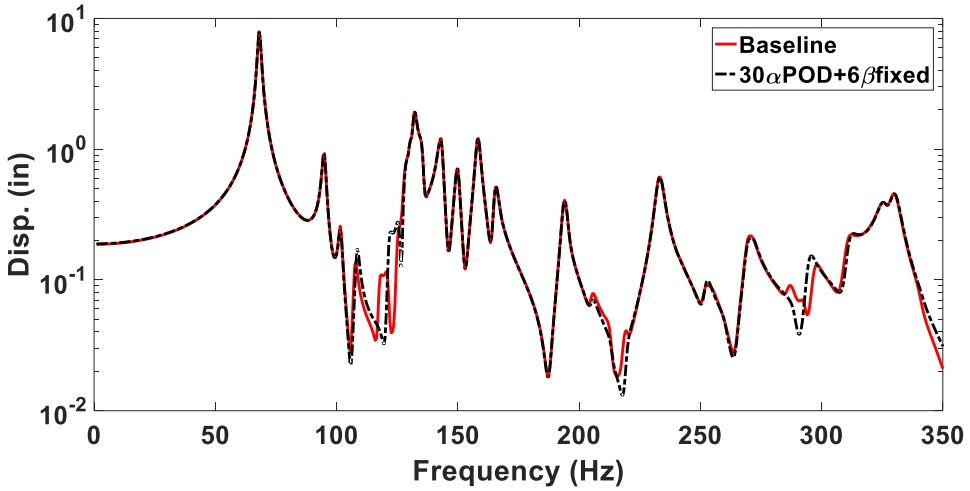

Figure 66 Comparison of the magnitudes of the frequency responses at the middle point of Bay 4, 6 β-fixed and 30 α-POD modes and baseline model

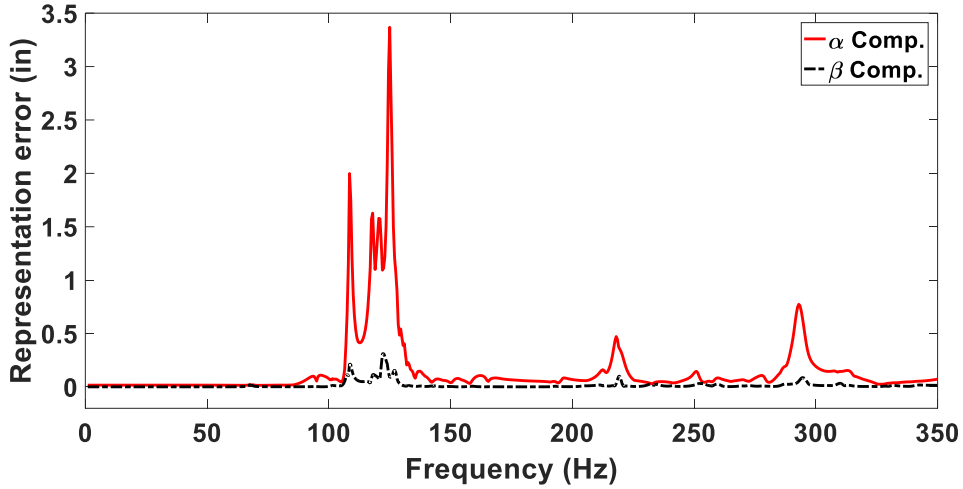

Figure 67 Comparison of the representation errors in α and β components, 6 β-fixed and 30 α-POD modes

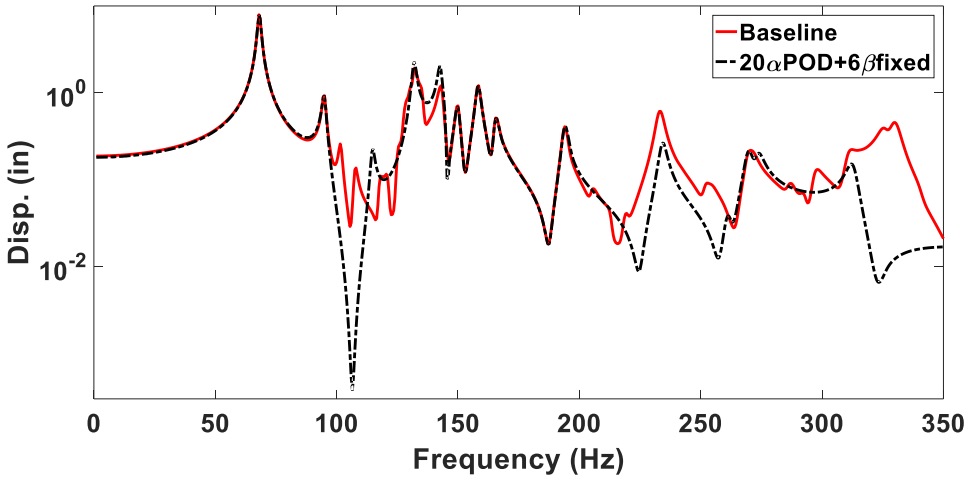

Figure 68 Comparison of the magnitudes of the frequency responses at the middle point of Bay 4, 6 β-fixed and 20 α-POD modes and baseline model

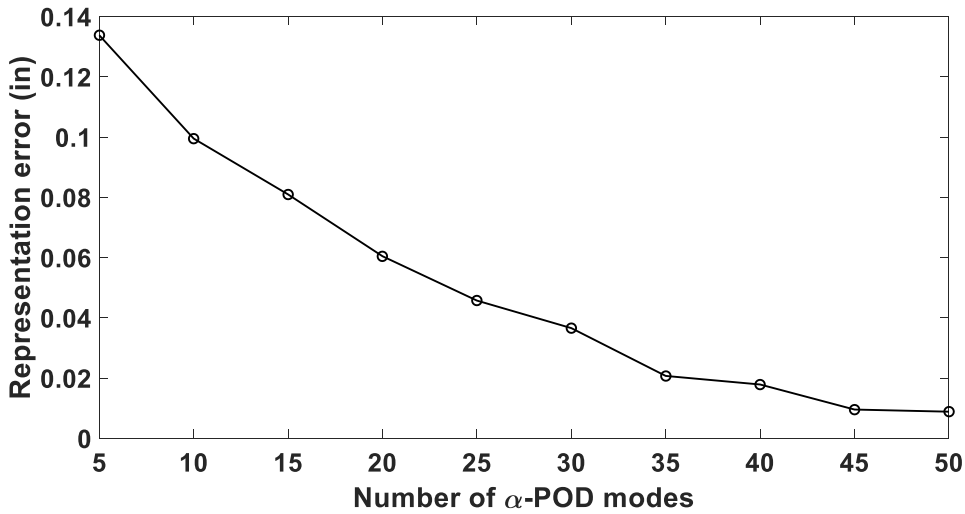

Figure 69 Representation error of the magnitude of frequency response in β versus the number of α-POD modes

4.1.2 ROMs Based on β-POD and α-POD Modes

The large ROM size required in the previous section could be attributed in part to the use of the fixed interface modes of the β component which are not representative of the actual motions in that component. Thus, a large number of such modes may be necessary. Moreover, to each mode in the β component is associated a series of α-POD modes forcing the model size to be larger than necessary. To try to mitigate this situation, a different representation of the β component response was sought. Specifically, the deflections of the β component of the linear modes in the [0,350] Hz band were first extracted and then a POD analysis of the snapshot matrix composed of these responses was carried out. These computed POD modes are referred to as "β-POD" modes in the sequel and were used to generate an associated basis in the β component following a process similar to the previous section.

A notable difference between β-POD and β-fixed interface modes is however that the degrees of freedom of the interface are included in the β-POD modes vs. separate degrees of freedom in the previous formulation. Then, the imposition of the motions in β to obtain the α-POD modes is actually achieved by prescribing the motion of the entire

boundary, i.e., the degrees of freedom $\underline{z}$ and computing the corresponding response in α according to Eq. (47) or

$$\boldsymbol{M}_{qq}^{\alpha}\ddot{\underline{q}}^{\alpha} + \boldsymbol{C}_{qq}^{\alpha}\dot{\underline{q}}^{\alpha} + \boldsymbol{K}_{qq}^{\alpha}\underline{q}^{\alpha} = -\boldsymbol{M}_{qY}^{\alpha}\ddot{\underline{z}} \tag{49}$$

Shown in Fig. 70 is the comparison of the magnitudes of the frequency responses at the middle point of the β component obtained with this 30 α-POD and 10 β-POD basis component-centric ROM and the baseline model. The excellent matching indicates the convergence of the prediction of the response in the β component with enough modes. The representation errors in α and β components shown in Fig. 71 confirm the finding and indicate that a better modeling of the β component than of the α one is achieved. These observations support the suitability of this approach as a component-centric ROM. However, the method suffers from the same large size issue as the previous one: 40 modes are used for Figs 70 and 71. Reducing the number of either α-POD or β-POD modes degrades the accuracy of the predictions as seen in Figs 72 and 73. Similar conclusions can be made from the slow representation error drop in β in Fig. 74.

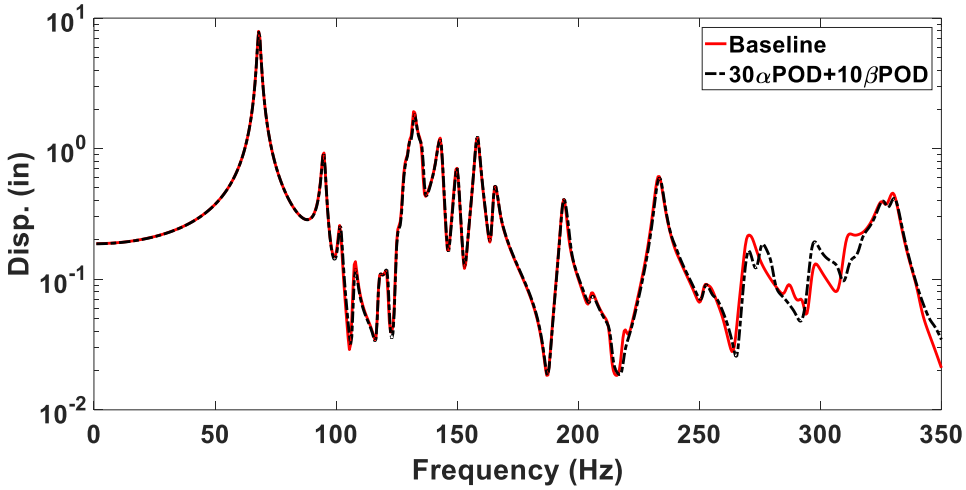

Figure 70 Comparison of the magnitudes of the frequency responses at the middle point of Bay 4, 30 α-POD and 10 β-POD modes and baseline model

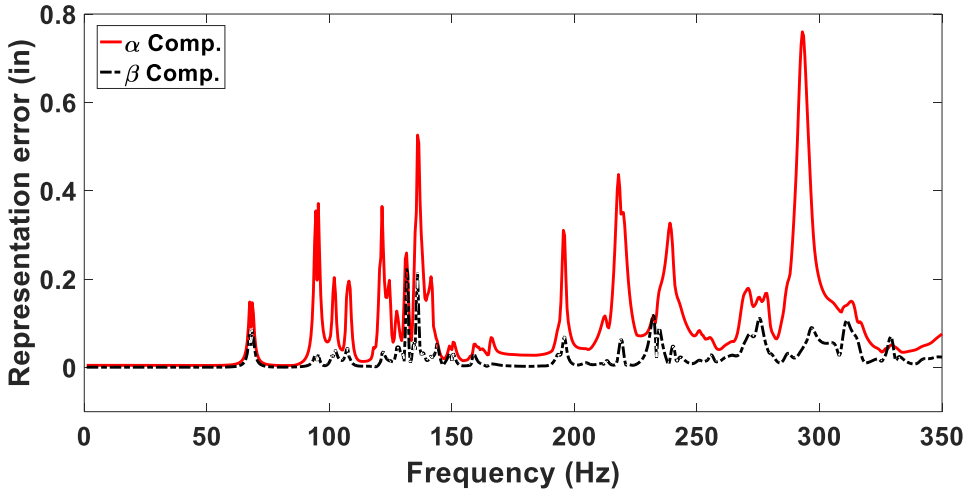

Figure 71 Comparison of the representation errors in α and β components, 30 α-POD and 10 β-POD modes

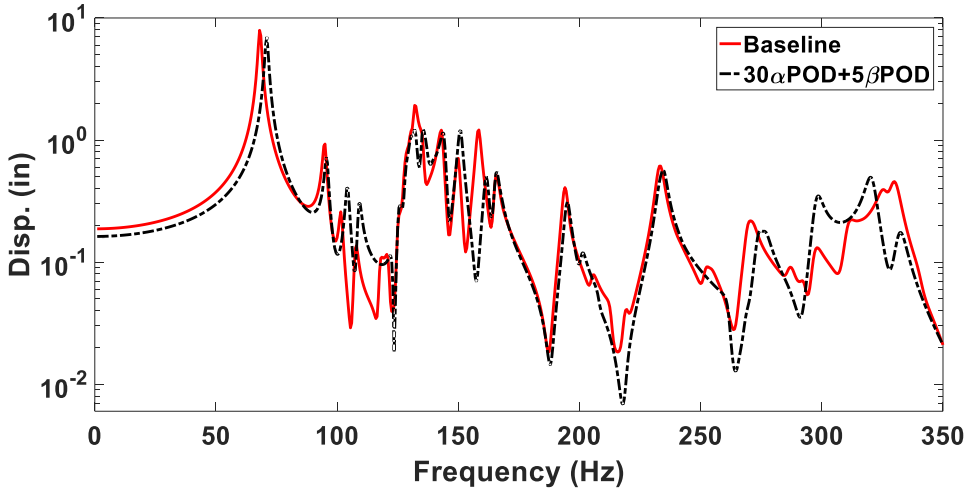

Figure 72 Comparison of the magnitudes of the frequency responses at the middle point of Bay 4, 30 α-POD and 5 β-POD modes and baseline model

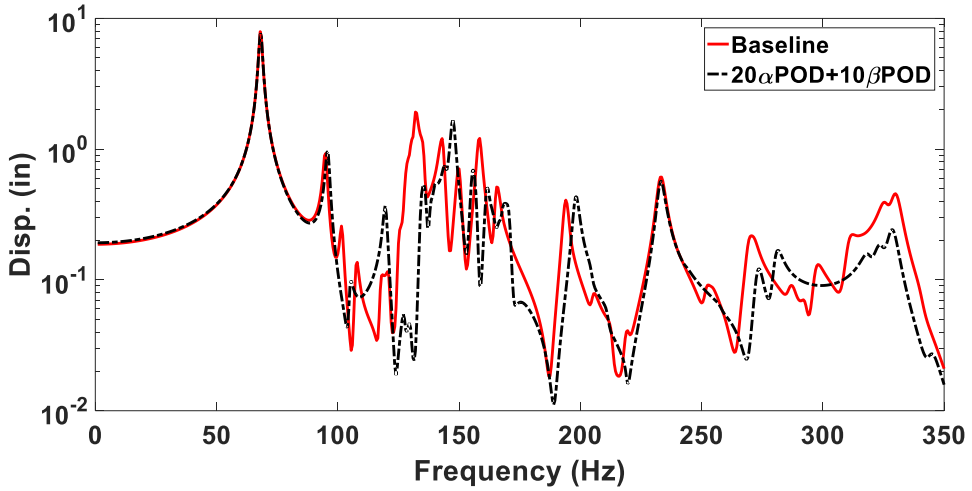

Figure 73 Comparison of the magnitudes of the frequency responses at the middle point of Bay 4, 20 α-POD and 10 β-POD modes and baseline model

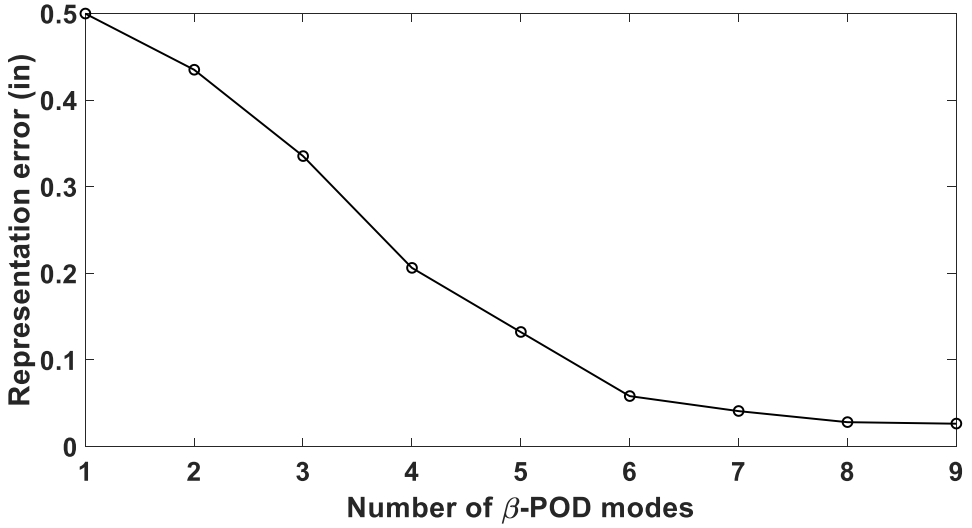

Figure 74 Representation error of the magnitude of frequency response in β versus the number of β-POD modes

4.2 "Global-Local" Based Method

The global-local method [49] proposed by Soize and Batou initially was used to deal with a complex structure with some global modes but numerous local modes in the low frequency range. Such feature exists in structures containing stiffened parts as well as flexible parts, for instance, complex aircraft panels and automotive vehicles. While the POD methods function as a spatial filter based on the left eigenvalue of measured

frequency responses using singular value decomposition (SVD) [50, 51], the algorithm introduced in [49] separately calculate the global modes and local modes of a structure which allows to construct a projection basis of the admissible space of displacements. The overall strategy of the "global-local" method is to divide the structure into subdomains. Global modes are then obtained by "smoothing"/averaging the mass matrix over each subdomain and local modes span the complement of the global modes. By varying the size of the subdomains, one can change how "global" or "local" the computed global and local modes. Within the present context, it would appear appropriate to divide the entire 9-bay panel into two subdomains, α and β, to approximate the α component and the β component with different accuracies. Before addressing this decomposition, the methodology is briefly reviewed.

The entire domain, Ω, is divided into n subdomains Ω_j^s:

$$\Omega = \cup_{j=1}^{n} \Omega_j^s, \text{ and } \Omega_j^s \cap \Omega_k^s = 0 \tag{50}$$

for j and k in $\{1\ 2\ \cdots n\}$. The size of the subdomains relates to the highest "wavelength" of the global modes that are extracted from the linear modes of the entire structure. Then a projection operator, $\underline{u} \longmapsto h_s^g(\underline{u})$ is defined which smooths the displacement field, transforming into a step value function constant in each subdomain. This operator is defined as:

$$\{h_s^g(\underline{u})\}(x) = \sum_j^n \mathbf{1}_{\Omega_j^s}(x) \frac{1}{m_j} \int \rho(x')u(x')dx' \tag{51}$$

in which $\mathbf{1}_{\Omega_j^s}(x) = 1$ if x is in the subdomain Ω_j^s and equals to zero, otherwise. Moreover, m_j is the mass of the subdomain Ω_j^s, which equals to $\int_{\Omega_j^s} \rho(x)dx$. In the discretized format of finite elements, Eq. (51) can be written as $\underline{u}_g = \boldsymbol{H}^g \underline{u}$. The mass matrix associated with the global displacements $\underline{u}_g$ is then:

$$\tilde{\boldsymbol{M}}_g = (\boldsymbol{H}^g)^T \tilde{\boldsymbol{M}} \boldsymbol{H}^g = \tilde{\boldsymbol{M}} \boldsymbol{H}^g = (\boldsymbol{H}^g)^T \tilde{\boldsymbol{M}} \tag{52}$$

where the last two equalities of Eq. (52) result from Eq. (51). A complementary mass matrix $\tilde{\boldsymbol{M}}_l$ is then simply introduced as

$$\tilde{\boldsymbol{M}}_l = \tilde{\boldsymbol{M}} - \tilde{\boldsymbol{M}}_g \tag{53}$$

The global modes are computed from the generalized eigenvalue problem:

$$\tilde{\boldsymbol{K}} \tilde{\phi}_g = \tilde{\lambda}_g \tilde{\boldsymbol{M}}_g \tilde{\phi}_g \tag{54}$$

For the local modes:

$$\tilde{\boldsymbol{K}} \tilde{\phi}_l = \tilde{\lambda}_l \tilde{\boldsymbol{M}}_l \tilde{\phi}_l \tag{55}$$

This above method is referred to as the "direct method". Alternatively, a "double projection method" can be used that has a lower computational cost and is less intrusive use to commercial finite element codes. The basic idea is to transform the finite element domain into a reduced order domain represented using the normal linear modes of the structure, $\boldsymbol{\Phi}$, so that the global modes and local modes from Eq. (54) and (55) will be expressed as:

$$\phi_g = \boldsymbol{\Phi} \tilde{\phi}_g, \quad \phi_l = \boldsymbol{\Phi} \tilde{\phi}_l \tag{56}$$

These modes can be obtained from the general eigenvalue problem shown below:

$$\boldsymbol{K} \phi_g = \lambda_g \boldsymbol{M}_g \phi_g, \quad \boldsymbol{K} \phi_l = \lambda_l \boldsymbol{M}_l \phi_l \tag{57}$$

where $\boldsymbol{K}, \boldsymbol{M}_g, \boldsymbol{M}_l$ are in the reduced system, $\boldsymbol{K} = \boldsymbol{\Phi}^T \tilde{\boldsymbol{K}} \boldsymbol{\Phi}, \boldsymbol{M}_g = \boldsymbol{\Phi}^T (\boldsymbol{H}^g)^T \tilde{\boldsymbol{M}} \boldsymbol{H}^g \boldsymbol{\Phi}, \boldsymbol{M}_l = \boldsymbol{\Phi}^T \tilde{\boldsymbol{M}} \boldsymbol{\Phi} - \boldsymbol{M}_g$.

Following either approach, the physical displacement field can then be expressed as using the basis a sum of contributions from the global and local modes:

$$\underline{u} = \underline{u}_g + \underline{u}_l \tag{58}$$

In which

$$\underline{u}_g = \sum_j^n \phi_g^{(j)} q_g^{(j)}$$
$$\underline{u}_l = \sum_j^\infty \phi_l^{(j)} q_l^{(j)} \tag{59}$$

where $q_g^{(j)}$ and $q_l^{(j)}$ are corresponding generalized coordinates. Note that the linear operator is conducted only on the transverse degrees of freedom, thus, the number of global modes obtained equals to the number of subdomains. The number of local modes included can be as large as possible based on the desired accuracy.

This method was adopted with the global modes intended to capture the coupling or interactions between the α and β components and the local modes as "enrichment" to accurately model the β component. To this end, 2 global modes and some local modes were obtained following the instruction above and are shown in Fig. 75. It is seen that the "global" modes obtained are not all "global"; also, include β-local by construction. Moreover, the "local" modes are not all "local" but are α-local.

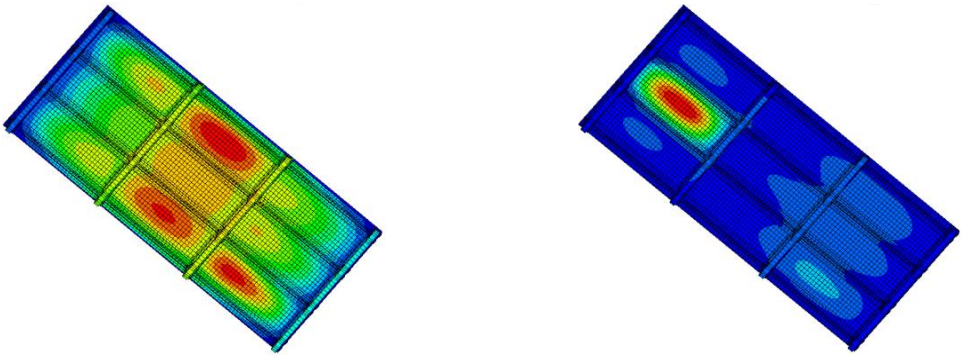

(a) (b)

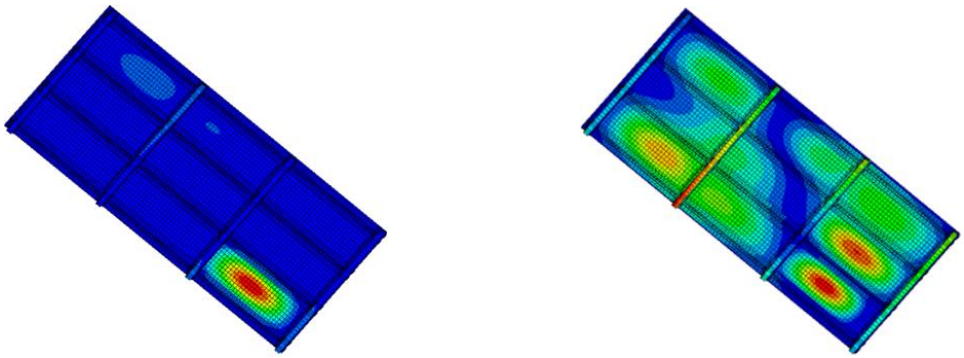

(c) (d)

Figure 75 Mode shapes of two global modes (a), (b) and two local modes (c), (d)

To maximize the information for the β component carried by the local modes, they were split into α-local modes and β-local modes based on the ratio of kinetic energy in β over that in α. Shown in Fig. 76 is these ratios for the linear modes and the local modes both in decreasing order. A fast decay is observed for the local modes with the maximum ratio for the local modes of 1.81 while that for the linear modes is 0.84. Finally, Fig. 77 compares the magnitude of the linear frequency responses at the center of bay 4 (considered as the β component). Generally close agreement can be seen between predictions from the Baseline and the ROM with 42 global-local modes. Also, the predictions in β are better than those in α as tasked.

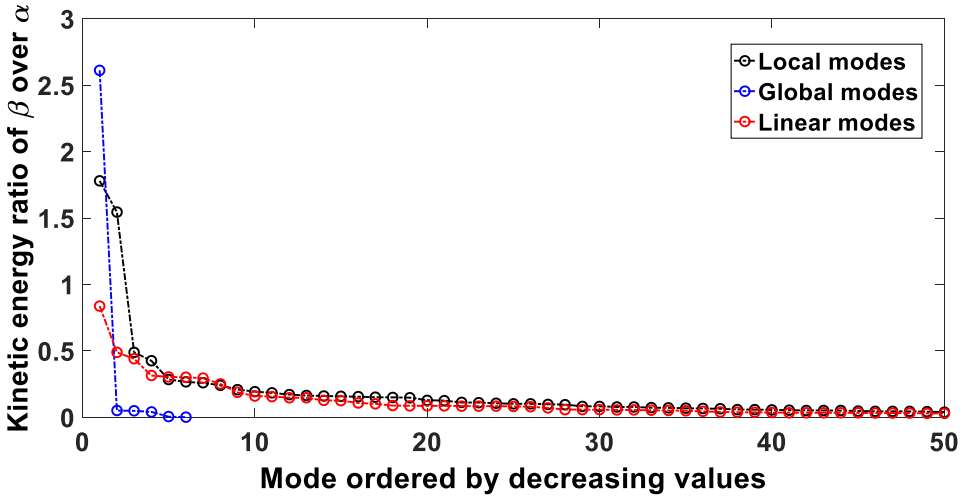

Figure 76 Ratio of kinetic energy in β over that in α

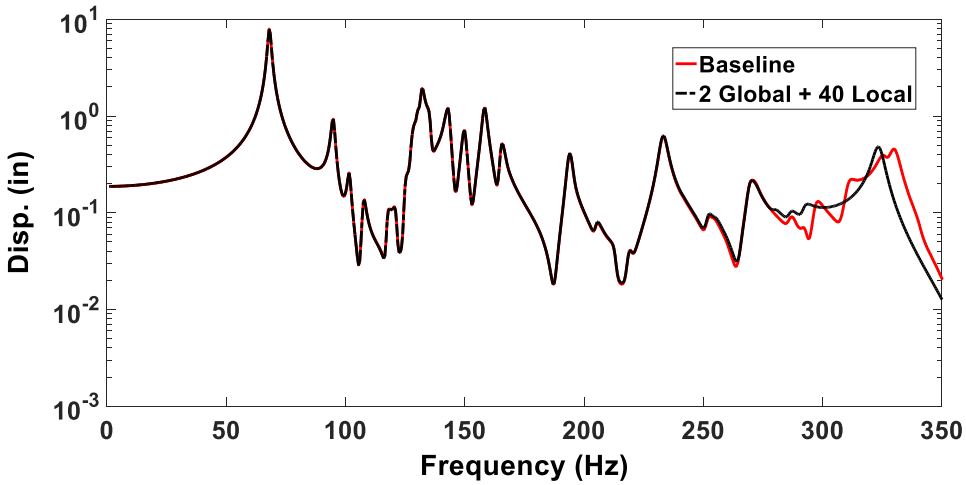

Figure 77 Comparison of the magnitudes of the frequency responses at the middle point of Bay 4

Even though the "Global-Local" approach generally agrees with the prediction of the linear mode basis, the modal reduction is not significant. The mode shapes of the linear modes are generally "global" (i.e., large deformation distributed in the entire structure) indicating a strong coupling of components and thus, it is very difficult to capture this coupling with a smaller set of modes. As the linear modes naturally account for the coupling, a fourth method is next investigated which starts from them and then rationally reduce the modal size without losing accuracy in β.

4.3 Linear Modes Based, Modal Lumping Approach

Analyzing the results obtained by the two Craig-Bampton methods suggests that the large ROM size issue originates from the large number of α-POD modes needed, i.e., from the difficulty in modeling the coupling between the α and β components. This modeling is however achieved naturally with the linear modes suggesting that they could be the foundation for a compact component-centric ROM. Seeking a reduction of the number of modes from the 50 existing in [0,350] Hz, it is first observed in Fig. 2 that there are only 16 separate peaks vs. the 50 expected. There are two reasons for the lower number of peaks. First, some of the linear modes have very small modal amplitudes resulting from the uniform pressure. Second, some peaks have merged with each other to

form single broader peaks. Based on these observations, the forth approach to construct a compact component-centric ROM starts from the linear modes in the band (all 50) and proceeds with two successive reductions of the modal basis: the linear mode selection and modal lumping both of which are described in the ensuing sections.

4.3.1 Linear Modal Selection

The first step of the modal basis reduction process is the careful selection of the linear modes based on their contribution to the response in the β component. This process is performed recursively as follows starting with the baseline model (including all modes) and its frequency response in the band:

(a) compute the response in the β component when one of the linear modes from the current model is removed and evaluate the corresponding norm error with respect to the predictions of the current model in the β component,

(b) repeat the computations of (a) for each mode of the current model in turn and determine which of the modes induced the smallest error,

(c) remove the mode with the smallest error from the current model to obtain a new, smaller size current model,

(d) repeat steps (a)-(c) until only one mode is left in the model.

Note that the "importance" of the linear modes should be opposite to the elimination order (e.g., the linear mode left at the end should be the most important one). The above recursive method provides a rigorous way to find the modes that contribute most to the response *in the* β *component*, but it requires the computation of a series of full solution. However, a much more practical strategy to determine these dominant modes can be based on the response estimate R_i derived from mode *i* maximum response in the β component, i.e.,

$$R_i = \left| \frac{F_i}{2\omega_i^2 \zeta_i} \right| \max(|\underline{U}_\beta^i|) \tag{60}$$

where F_i, ω_i , ζ_i are the modal force, natural frequency and damping ratio associated with the linear mode i. This mode has values $\underline{U}_\beta^i$ in the β component and their maximum (in absolute value) is $\max(|\underline{U}_\beta^i|)$. Shown in Tables 3 and 4 are the 21 most important linear modes predicted, respectively, from the recursive algorithm described above and from Eq. (60), i.e., those with the largest values of R_i. Comparing them, it is seen that the 14 most dominant modes are identical, i.e., correctly predicted by Eq. (60), with some switches of order occurring on the following ones due, most likely, to the lack in Eq. (60) of coupling effects between two modes of close natural frequencies. The frequency response functions of the middle point of Bay 4 predicted by the two 21 modes models of Tables 3 and 4 are compared to each other and to the baseline in Fig. 78. An excellent match between the three curves is observed demonstrating that: (i) the number of modes necessary to achieve a close match of the frequency response in the β component is much smaller than the total number of modes in the band for a given loading, and (ii) the two selections algorithms, the recursive one and the one based on Eq. (60), are effectively equivalent in identifying the modes that matter.

Table 3

Selected Mode Numbers (by Decreasing Order of Importance) and Corresponding Natural Frequencies (Hz) for Bay 4, Recursive Algorithm

Mode	Natural Frequency	Mode	Natural Frequency	Mode	Natural Frequency	Mode	Natural Frequency	Mode	Natural Frequency
1	68.15	29	241.09	11	132.00	17	158.29	28	233.58
49	340.73	15	143.17	2	94.89	16	149.89	21	193.86
12	135.43	10	130.43	48	330.00	19	165.35	36	271.22
9	129.01	45	314.94	25	218.23	8	127.48	35	269.53
37	279.35								

Table 4

Selected Mode Numbers (by Decreasing Order of Importance) and Corresponding Natural Frequencies (Hz) for Bay 4, Predicted from Eq. (60)

Mode	Natural Frequency	Mode	Natural Frequency	Mode	Natural Frequency	Mode	Natural Frequency	Mode	Natural Frequency
1	68.15	29	241.09	11	132.00	17	158.29	28	233.58
49	340.73	15	143.17	2	94.89	16	149.89	21	193.86
12	135.43	10	130.43	48	330.00	19	165.35	14	142.23
36	271.22	4	107.58	9	129.01	45	314.94	25	218.23
26	219.67								

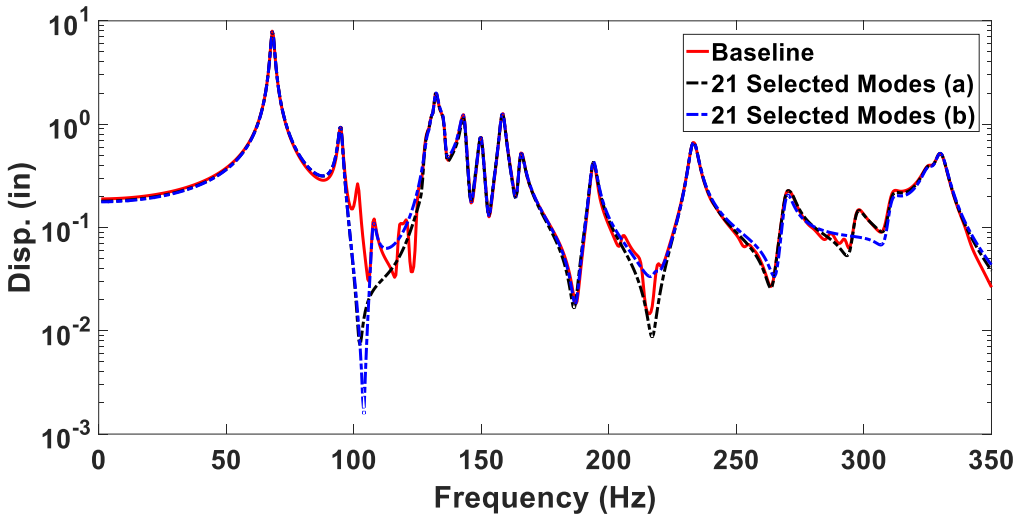

Figure 78 Comparison of the magnitudes of the frequency responses at the middle point of Bay 4, baseline model and 21 selected modes from (a) the recursive algorithm (Table 3), (b) Eq. (60) (Table 4)

4.3.2 Linear Modal Lumping

The presence of stiffeners leads to two particular properties. First, it induces a partial localization of higher modes and to the appearance of groups of modes with close natural frequencies, as discussed in section 3.1, see Table 1 and Fig. 2. Second, the displacement field of a particular panel is often similar in many of these modes, especially those with close natural frequencies. For illustration, the 5 linear modes 8-12 with close frequencies (between 127 Hz and 136 Hz) are plotted in Figs 79 and 80. It is clearly seen that the 5 mode shapes in each bay are most of the time similar. This phenomenon provides a potential to further reduce the number of modes for the ROM by “lumping” these linear

modes together - that is, by approximating the contributions of these 5 close frequencies modes *in the* β *component only* by that of a single one of them or two if needed. Formally, modal lumping will refer here to as approximating in the β component the sum of two or more modal contributions by that of a single mode. For the approximation to be accurate, the two or more modes must have (i) close frequencies and (ii) similar modal deflections in the β component. Stated differently, modes that can be lumped would be those which would be difficult to differentiate/identify if a modal testing of the structure was carried out and only the response in the β component was captured. To clarify the lumping process, let the displacement field in the β component be represented as:

$$\underline{u}_\beta(\underline{X},t) = q_1(t)\underline{U}_\beta^1 + q_2(t)\underline{U}_\beta^2 + \cdots + q_i(t)\underline{U}_\beta^i + q_j(t)\underline{U}_\beta^j + \cdots + q_n(t)\underline{U}_\beta^n \tag{61}$$

where $\boldsymbol{U}_\beta = \left[\underline{U}_\beta^1\ \underline{U}_\beta^2\ \cdots\ \underline{U}_\beta^i\ \underline{U}_\beta^j\ \cdots\ \underline{U}_\beta^n\right]$ are the displacements in the β component of the mass normalized linear modes and $q_1, q_2, \cdots, q_n$ are the corresponding generalized coordinates. Next, assume that $\underline{U}_\beta^i$ and $\underline{U}_\beta^j$ are the modes that can potentially be lumped, i.e., their mode shape in the β component are very similar so that

$$\underline{U}_\beta^j \approx a\underline{U}_\beta^i \tag{62}$$

where the scalar a may be estimated as $a = (\underline{U}_\beta^j)^T\underline{U}_\beta^i/\left\|\underline{U}_\beta^i\right\|^2$.

Introducing the approximation of Eq. (62) in Eq. (61), it is found that

$$\underline{u}_\beta(\underline{X},t) = q_1(t)\underline{U}_\beta^1 + q_2(t)\underline{U}_\beta^2 + \cdots + \bar{q}_i(t)\underline{U}_\beta^i + \cdots + q_n(t)\underline{U}_\beta^n \tag{63}$$

$$\bar{q}_i(t) = q_i(t) + aq_j(t) \tag{64}$$

Consider next the equations of motion for the generalized coordinates $q_i(t)$ and $q_j(t)$, i.e.,

$$\ddot{q}_i + 2\zeta_i\omega_i\dot{q}_i + \omega_i^2 q_i = F_i \tag{65}$$

and

$$\ddot{q}_j + 2\zeta_j\omega_j\dot{q}_j + \omega_j^2 q_j = F_j \tag{66}$$

where F_i and F_j are the corresponding modal forces. Assuming that the mode j has both natural frequency and damping ratio close to those of mode i, Eq. (66) can be approximated as

$$\ddot{q}_j + 2\zeta_i\omega_i\dot{q}_j + \omega_i^2 q_j = F_j \tag{67}$$

which can be combined with Eq. (65) to yield

$$\ddot{\bar{q}}_i + 2\zeta_i\omega_i\dot{\bar{q}}_i + \omega_i^2\bar{q}_i = F_i + aF_j \tag{68}$$

Thus, the sum of the contributions of the two modes i and j has been approximated by that of a single one (mode i) in both time, Eq. (68), and space, Eq. (62).

As a first example of application of the lumping process, consider Bay 4 and note from Table 3 that modes 8-12 are all listed in the 21 most important modes. They exhibit close natural frequencies, between 127 and 136 Hz, and very similar modal deflection in the β component, see Fig. 80. They are thus prime candidates for modal lumping. Of these 5 modes, mode 11 is the largest contributor to the response and thus was selected as the mode on which the other 4 were lumped. Shown in Fig. 81 are the frequency response function of the middle point of Bay 4 computed using (a) the 21 selected modes, (b) the 17 modes remaining after the elimination of modes 8, 9, 10, and 12 from the 21 selected ones, and (c) the 17 modes model of (b) with modes 8, 9, 10, and 12 lumped onto mode 11. The magnitude of the response obtained with the latter 17 modes model clearly matches much better the 21 selected modes predictions than the 17 modes model of (b). In fact, the matching of the lumped modes model frequency response function with its counterpart from the 21 selected modes is so close that it can be substituted for it leading to a reduction of the number of modes in the ROM from 21 to 17.

To further demonstrate the applicability and benefits of the lumping method, shown in Fig. 82 are the frequency responses of the middle of Bay 1 (assumed as β component)

with the largest 20 selected linear modes and a 20-mode model including these modes as well as the lumping of 6 other modes (modes 9, 10, 12, 15, 22, and 42) of frequencies 129.01, 130.43, 135.43, 143.17, 195.42 and 296.87Hz. The contributions of the first three modes were lumped on the one of mode 11 of frequency 132.00Hz while those of the last 3 modes were lumped with those of modes 14, 21 and 40 of frequencies equal to 142.23, 193.86 and 292.14Hz. As shown, the lumping method improves notably the prediction of the response. The conclusions derived from these results hold for the rest of the panels as shown in Figs. 83 to 89.

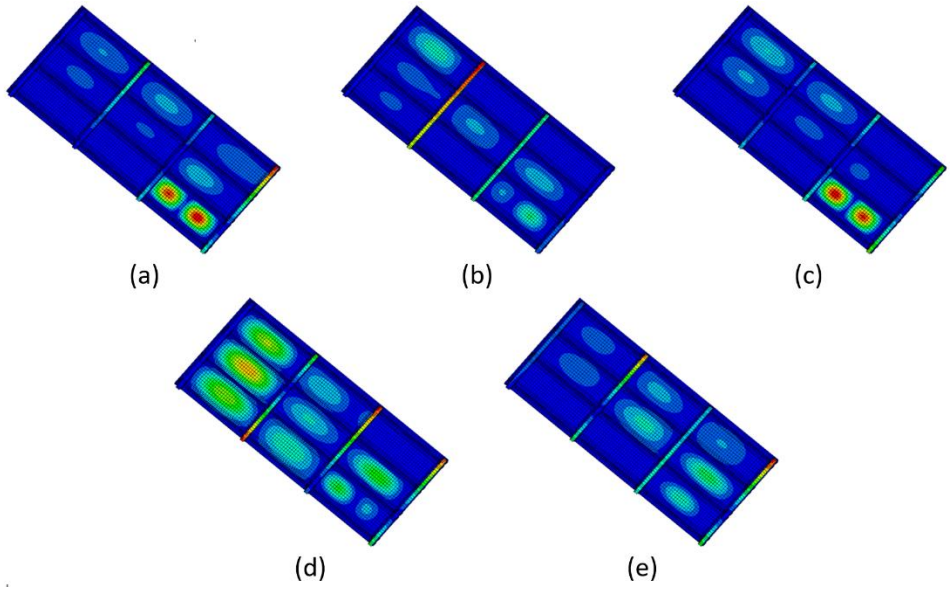

Figure 79 Contour plots of the norm of displacements for linear modes 8-12 (in order (a)-(e)) in the band [127,136] Hz. Dark blue/red zones correspond to the lowest/highest values

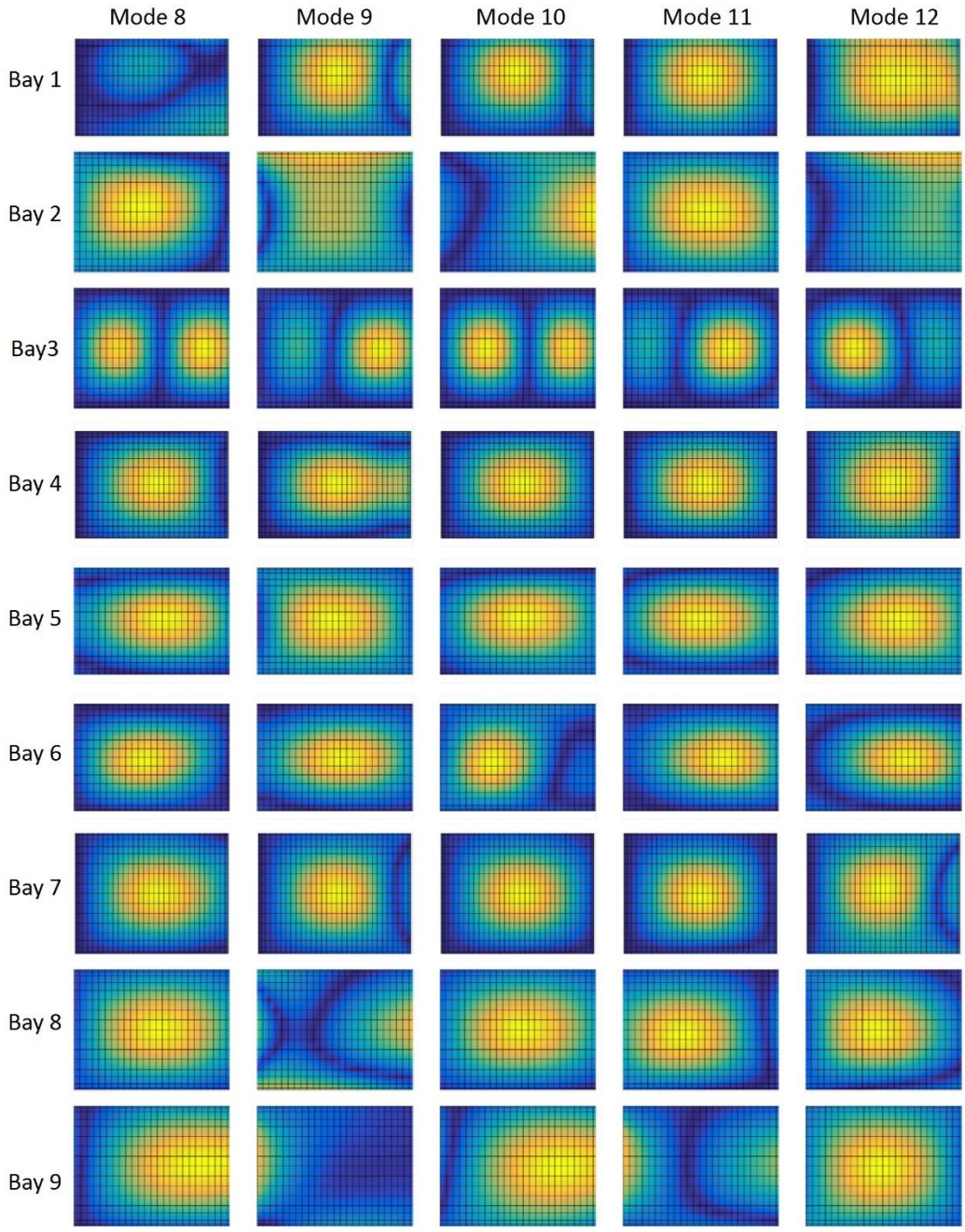

Figure 80 Contour plots of the norm of displacements for the linear modes of Fig. 79 but each mode is normalized in each bay

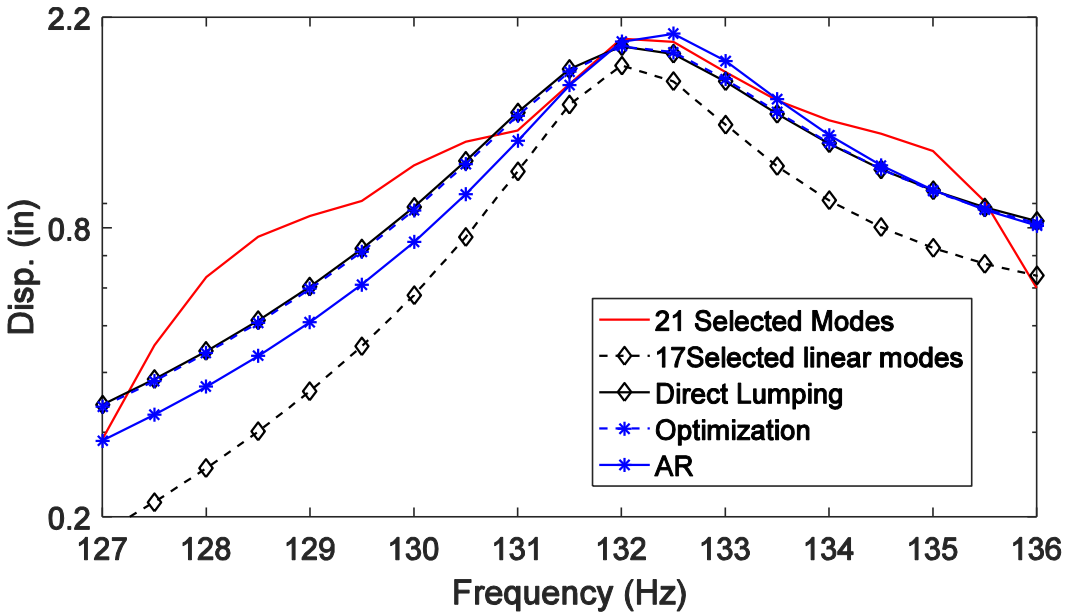

Figure 81 Comparison of the magnitudes of the frequency responses of the middle point of Bay 4 obtained with 17 selected linear modes and the 17 modes model resulting from a direct and optimized lumping of modes 8, 9, 10, and 12 on mode 11

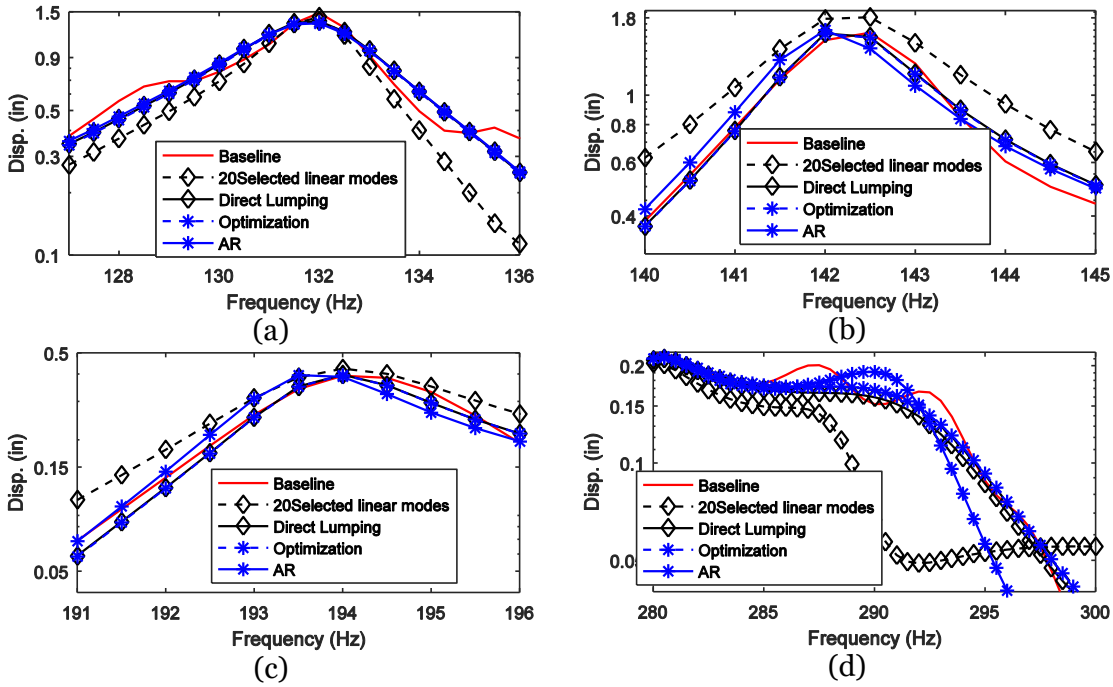

Figure 82 Comparison of the magnitudes of the frequency responses of the middle point of Bay 1 obtained with 20 selected linear modes and the 20 modes model resulting from direct lumping and optimized lumping. Frequency band: (a) [127,136] Hz, (b) [140,145] Hz, (c) [191,196] Hz, (d) [280,300] Hz

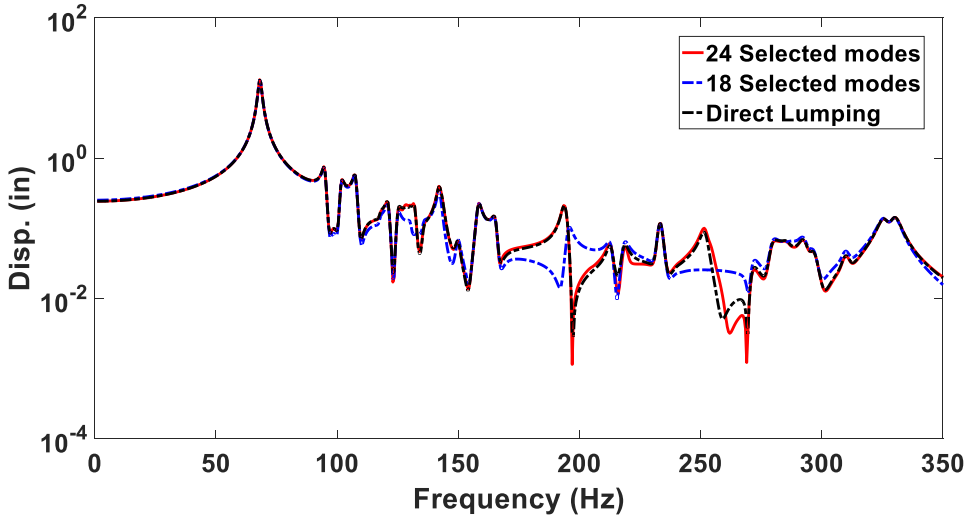

Figure 83 Comparison of the magnitudes of the frequency responses of the middle point of Bay 2 obtained with 18 selected linear modes and the 18 modes model resulting from direct lumping

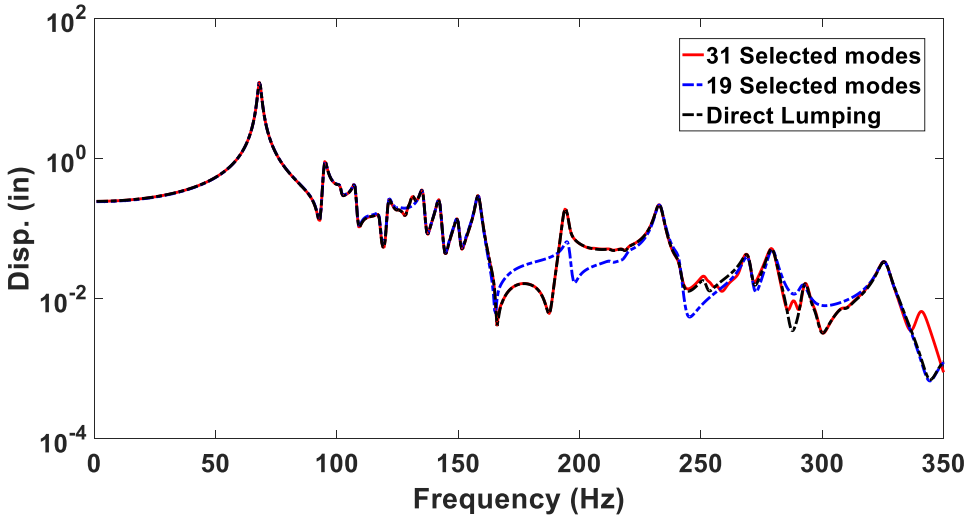

Figure 84 Comparison of the magnitudes of the frequency responses at the middle point of Bay 3 obtained with 19 selected linear modes and the 19 modes model resulting from direct lumping

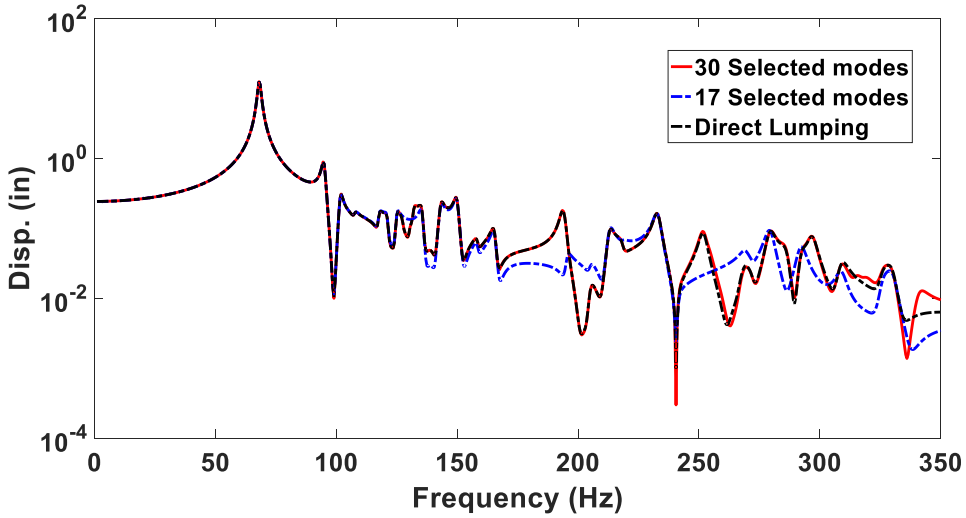

Figure 85 Comparison of the magnitudes of the frequency responses at the middle point of Bay 5 obtained with 17 selected linear modes and the 17 modes model resulting from direct lumping

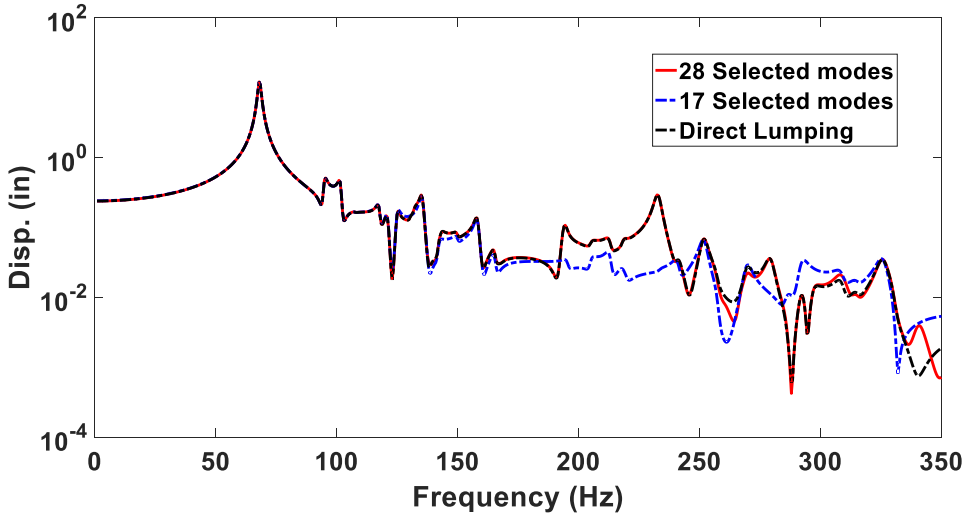

Figure 86 Comparison of the magnitudes of the frequency responses at the middle point of Bay 6 obtained with 17 selected linear modes and the 17 modes model resulting from direct lumping

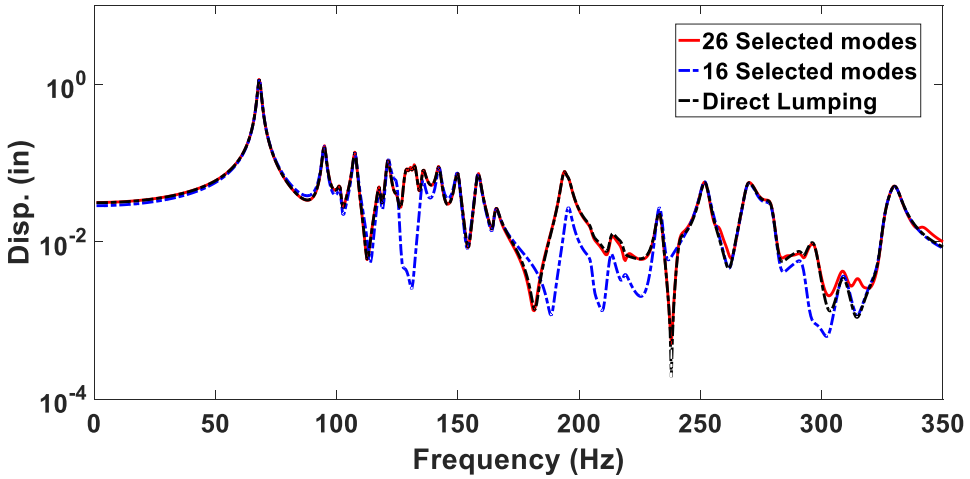

Figure 87 Comparison of the magnitudes of the frequency responses at the middle point of Bay 7 obtained with 16 selected linear modes and the 16 modes model resulting from direct lumping

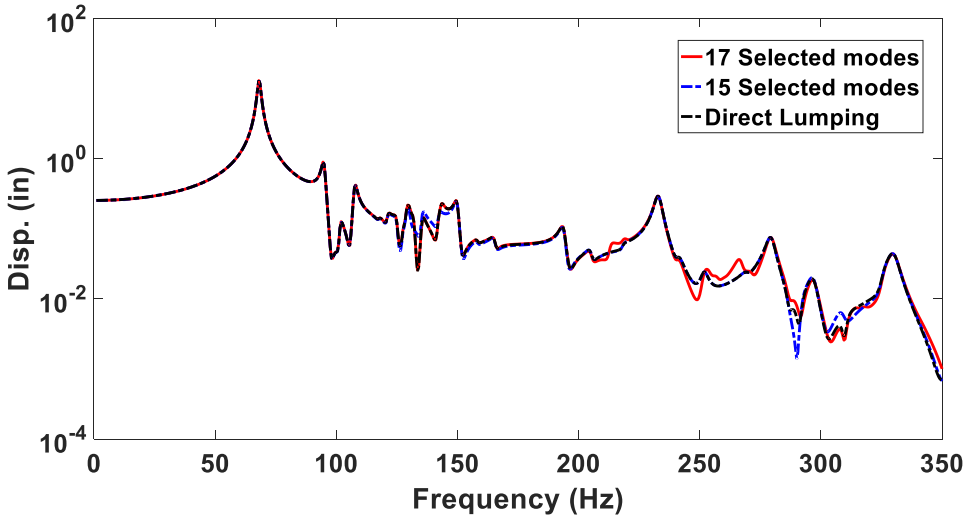

Figure 88 Comparison of the magnitudes of the frequency responses at the middle point of Bay 8 obtained with 15 selected linear modes and the 15 modes model resulting from direct lumping

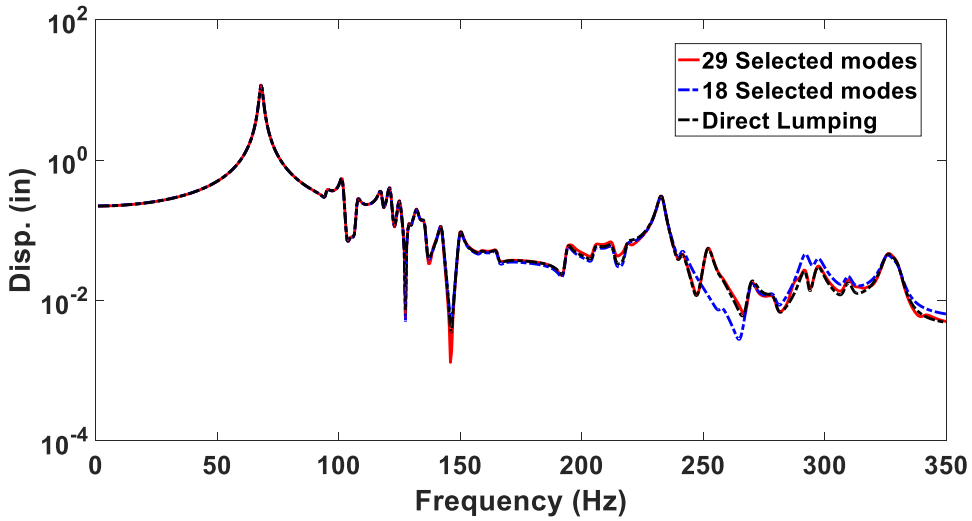

Figure 89 Comparison of the magnitudes of the frequency responses at the middle point of Bay 9 obtained with 18 selected linear modes and the 18 modes model resulting from direct lumping

4.3.3 Linear Modal Lumping with Optimization

In the lumping approach described above, referred to as “direct lumping” in the sequel, the resulting natural frequency and damping ratio are those of the dominant mode. Further improvements of the matching of the resulting frequency response function with its baseline can be sought by optimizing these two parameters as well as the modal force. Two optimization options have been investigated.

(A) A frequency domain optimization in which the natural frequency, damping ratio, and modal force are sought to minimize the norm difference of the frequency responses of the model with the lumped modes and the baseline model over the frequency band of the lumped modes natural frequencies. The frequency response corresponding to each linear mode is obtained by solving Eq. (65) and the summation of these solutions forms the approximation of the actual structural response, i.e., for two modes

$$H(\omega) = \frac{F_p}{\left(\omega_p^2 - \omega^2\right) + 2i\zeta_p\omega_p\omega} + a\,\frac{F_q}{\left(\omega_q^2 - \omega^2\right) + 2i\zeta_q\omega_q\omega} \tag{69}$$

where p and q represent the indices of the linear modes being lumped, $a = (\underline{U}_\beta^q)^T \underline{U}_\beta^p / \left\|\underline{U}_\beta^p\right\|^2$, and i is the imaginary unit ($i^2 = -1$). Then, the natural frequency $\breve{\omega}$, damping ratio $\breve{\zeta}$, and modal force $\breve{F}$ of the optimum lumped mode will be selected to minimize

$$\int_{\omega_p-\delta}^{\omega_q+\delta} \left| |H(\omega)| - \left| \frac{\breve{F}}{(\breve{\omega}^2 - \omega^2) + 2i\breve{\zeta}\breve{\omega}\omega} \right| \right| d\omega \tag{70}$$

where $\delta > 0$ specifies the range of frequencies to be considered outside of the domain of the natural frequencies of the two modes to be lumped. Initial guesses for $\breve{\omega}$, $\breve{\zeta}$ and $\breve{F}$ were selected as

$$\breve{\omega}_0 = \left(\omega_p + \omega_q\right)/2 \;\; ; \breve{\zeta}_0 = \left(\zeta_p + \zeta_q\right)/2 \;\; ; \;\; \breve{F}_0 = F_p + aF_q \tag{71}$$

with the initial guess on the modal force consistent with the direct lumping approach. The selection of $\breve{\omega}_0$ as the average of the natural frequencies stems from the expectation that $\breve{\omega}$ would lie between ω_p and ω_q.

The above procedure was applied first to Bay 4, to the lumping of the contributions of modes 8, 9, 10, and 12 onto the one of mode 11. The optimization was carried out numerically using the optimizer *fminsearch* in Matlab. The average of the natural frequencies of the 5 modes is 131Hz and the damping ratios of these modes range from 0.0068 to 0.0069. Moreover, the parameter δ was chosen equal to 5Hz. The convergence result shows that the optimal natural frequency is 132 Hz and the damping ratio is 0.0095. The frequency response function of the middle point of Bay 4 corresponding to this approximation is shown in Fig. 81. Comparing it to the direct lumping and the 21 selected modes curves, it is seen that the optimization does indeed provide an improved matching of the baseline frequency response over the direct lumping method.

(B) An identification based approach in the time domain was considered next. In this strategy, the responses of the modes to be lumped are combined in the time domain to simulate "measured data" (e.g., impulse response) to which a single degree of freedom ("1-DOF") model is fit using an autoregressive (AR) modeling, Fig. 90 illustrates the process.

The simulated "measured data" $x(n)$ is assumed here to be the impulse response of a representative point of the β component constructed only from the set of linear modes to be lumped, i.e., assuming the two modes p and q as before:

$$x(n) = \frac{F_p}{\omega_{dp}} e^{-\zeta_p \omega_p n\Delta t} \sin(\omega_{dp} n\Delta t) + a \frac{F_q}{\omega_{dq}} e^{-\zeta_q \omega_q n\Delta t} \sin(\omega_{dq} n\Delta t) \qquad (72)$$

where $a = (\underline{U}_\beta^q)^T \underline{U}_\beta^p / \left\| \underline{U}_\beta^p \right\|^2$ provides the scaling of mode q in comparison to mode p as in Eq. (69). Further, ω_{dp} and ω_{dq} are the damped circular frequencies of modes p and q defined as

$$\omega_{dp} = \omega_p \sqrt{1 - \zeta_p^2} \; ; \omega_{dq} = \omega_q \sqrt{1 - \zeta_q^2} \qquad (73)$$

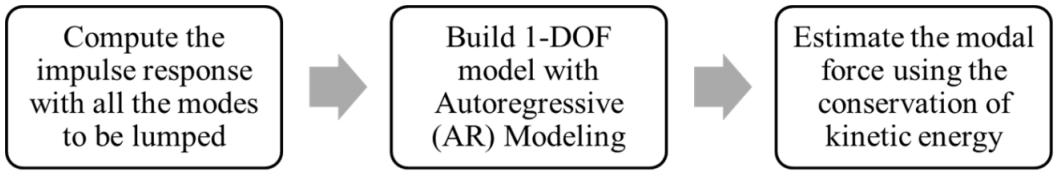

Figure 90 Illustration of the optimization process using the AR modeling

Figure 91 shows the simulation data constructed for Bay 4 with the linear modes 8 to 12. As expected, this curve is more complex than the response of a single degree of freedom system and thus the time window over which this data is modeled will affect the estimates of the natural frequency and especially of the damping ratio. For the simulated measured data to appear as originating from a single degree of freedom system, the observation time must be small enough that the difference in frequencies between the various modes is *not* perceived. Then, the modal contributions will effectively be lumped.

This window must however be long enough to get an accurate estimate of the frequency and damping ratio. These conflicting requirements led to the use of 1.5 period of the average frequency of the modes to be lumped. Finally, the window was started at the peak of the data so that the decay of the response be visible in the short analysis window. For the simulated measured data of Fig. 91, the analysis window was thus selected as shown in Fig. 92.

Modeling the free response of Fig. 92 by that of a single degree of freedom system was carried out through an autoregressive (AR) fit of the data. That is, the data was modeled according to the recursion [48, 52, 53]

$$x(n) = \sum_{i}^{M} a_i x(n-i) + \varepsilon(n) \tag{74}$$

where $x(n)$ is the current value of the time series, a_i are predictor (weighting) coefficients, M is the model order, indicating the number of the past values used to predict the current value, and $\varepsilon(n)$ represents a one-step prediction error, i.e. the difference between the predicted value and the current value at this point.

Since the free response of a single degree of freedom data is exactly representable in the form of Eq. (74) with M = 2, this value was adopted; leading to the model

$$x(n) + a_1 x(n-1) + a_2 x(n-2) = \varepsilon(n) \tag{75}$$

The coefficients a_1 and a_2 were obtained from the correlation approach [52] seeking the minimum of $\sum_n [\varepsilon(n)]^2$. The natural frequency $\breve{\omega}$ and damping ratio $\breve{\zeta}$ (assumed less than 1) could then be estimated by equating the free responses of the AR and SDOF models. The latter is of the form $e^{\lambda t}$, sampled at $t = n\Delta t$, where

$$\lambda = -\check{\zeta}\breve{\omega} \pm i\breve{\omega}\sqrt{1-\check{\zeta}^2} \tag{76}$$

The free response of the AR model of Eq. (75) is of the form ρ^n where ρ is any of the two solutions of the quadratic equation

$$\rho^2 + a_1\rho + a_2\rho = 0 \tag{77}$$

Then, matching the two free response implies that $\rho = e^{\lambda\,\Delta t}$ from which it is found that [53, 54]

$$\begin{aligned} \breve{\omega} &= \sqrt{\left(\frac{\ln(|\rho|)}{\Delta t}\right)^2 + \left(\frac{\arg(\rho)}{\Delta t}\right)^2} \\ \check{\zeta} &= -\frac{\ln(|\rho|)}{\breve{\omega}\Delta t} \end{aligned} \tag{78}$$

Finally, the equivalent modal force $\check{F}$ is determined by matching the signal energy of the simulated measured data of Eq. (72) and its single degree of freedom approximation $\check{x}(n)$, i.e.,

$$\check{x}(n) = \frac{\check{F}}{\breve{\omega}_d} e^{-\check{\zeta}\breve{\omega}n\Delta t}\sin(\breve{\omega}_d n\Delta t) \tag{79}$$

where $\breve{\omega}_d = \breve{\omega}\sqrt{1-\check{\zeta}^2}$. That is,

$$\check{F} = sign(F_b)\frac{\|x\|}{\|\check{x}\|} \tag{80}$$

The above procedure was first applied to Bay 4 and the lumping of modes 8-12. The time step was chosen as $\Delta t = \pi/(30\bar{\omega})$, where $\bar{\omega}$ is the average of the natural frequencies of the modes to be lumped. Shown in Fig. 81 is the resulting approximation of the frequency response function of the middle point of Bay 4. It is seen that the AR identification approach of (B) yields very similar results as the frequency optimization of (A).

Another assessment of the three lumping methods was carried out on Bay 1 where the contributions of modes 9, 10, 12, 15, 22, and 42 were lumped onto those of modes 11, 14, 21 and 40 as performed earlier with the direct lumping method. Fig. 82 is the corresponding comparison of the frequency responses. As in Fig. 81, it is seen from Fig. 37 that the full optimization approach (A) provides an improved matching of the baseline frequency response over the direct lumping method. Moreover, the AR identification approach of (B) again yields very similar results to those obtained with the frequency optimization method (A) except in the neighborhood of 325Hz. A similar, although clearer, perspective on the benefits of the lumping optimization methods can finally be obtained from the mean representation error, see Table 5. Given its lower computational cost, the AR identification approach (B) appears to be the best tradeoff between accuracy of the resulting model and computational effort.

Table 5

Mean Representation Errors (in) of the Three Modal Lumping Approaches

Bay #	Direct Lumping	Optimization	AR
1	0.04	0.015	0.02
2	0.05	0.012	0.018
3	0.06	0.016	0.02
4	0.03	0.014	0.015
5	0.02	0.011	0.012
6	0.04	0.011	0.014
7	0.03	0.012	0.02
8	0.03	0.011	0.011
9	0.04	0.013	0.015

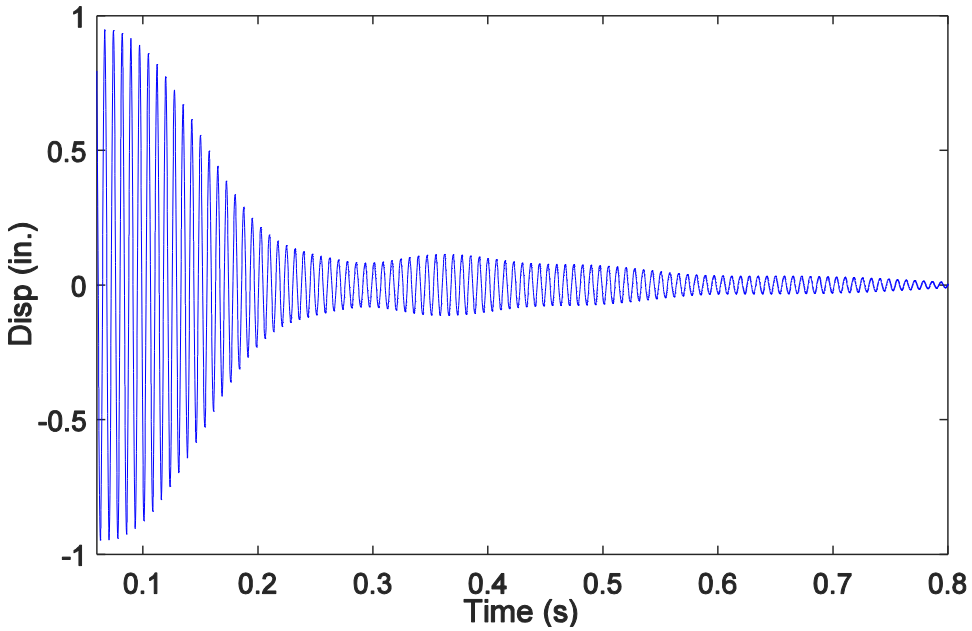

Figure 91 Simulation data for the identification based lumping of the linear modes 8 to 12; Bay 4

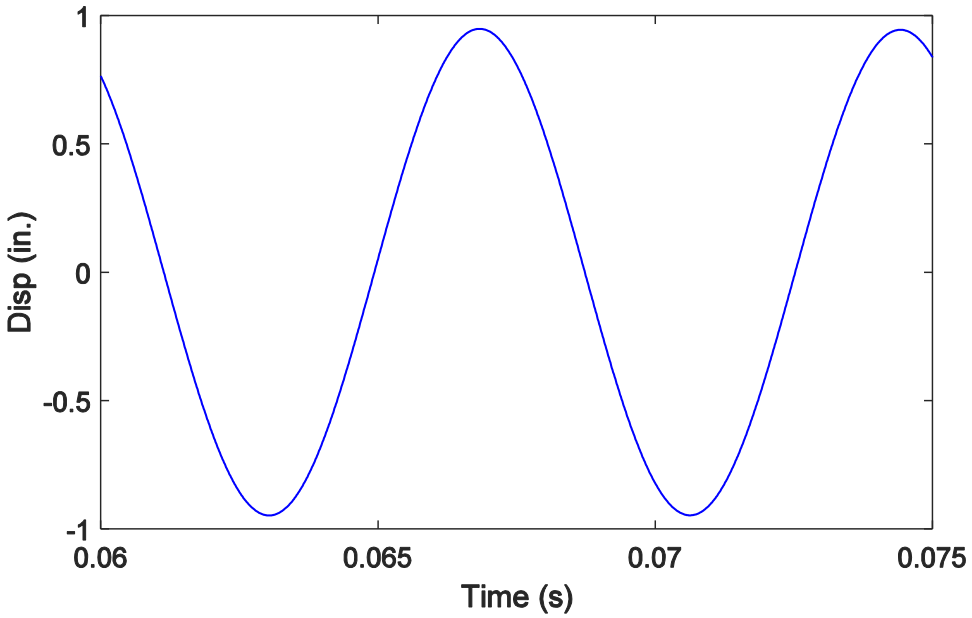

Figure 92 Data used for the identification based lumping of the linear modes 8 to 12; Bay 4

4.3.4 Robustness Assessment

The construction of component-centric ROMs by the modal lumping approaches, see section 4.4, relied on a known loading and on the occurrence of close frequencies of a

particular set of modes (those being lumped). These conditions may change if the environment varies and/or the structure is modified, e.g., as would happen in the design process. Accordingly, it is desirable to assess the sensitivity of the response predictions accuracy to variations in both the loading and/or the structural properties of the β component.

These assessments were carried out with the 17 mode ROM of Bay 4 obtained with the AR lumping approach, see Fig 81. First, the uniform loading was retained but the thickness of bay 4 was reduced (see Fig. 93(b)) or increased (see Fig. 93(c)) by 20%. The modal basis used for these computations, including the lumping details, was the same as for the original thickness but the ROM mass and stiffness matrices were computed for each thickness by projecting the corresponding finite element mass and stiffness matrices on the modes. Accordingly, they were full for the latter modified cases vs. diagonal for the original model. While the accuracy of the predictions is somewhat degraded, the ROM still captures well the β component dynamics suggesting that this component-centric ROM could be used in an optimization effort without having to reselect the modal basis.

To assess the sensitivity to the loading, a triangular load varying from zero to full value along the *x*-axis (long side of the panel) was applied to the ROM of Bay 4 constructed with the uniform loading. Then, shown in Fig. 93(d) is the resulting prediction of the frequency response of the middle point of Bay 4 as compared to a full modal solution. With the exception of the peak around 101Hz, the matching is still excellent. The large increase of the response at that frequency results from the symmetry breaking of the triangular loading which excites particularly that mode (mode 3). This observation suggests that the loading used to develop the component-centric ROM should either closely approximate the one that the structure will be subjected to, if known, or

otherwise not exhibit a particular symmetry that may induce a zero modal force in some important modes. If mode 3 had been included in the original lumping process to form an 18 mode model based on a uniform loading, the prediction would have been excellent for the triangular load as is shown on Fig. 93(e).

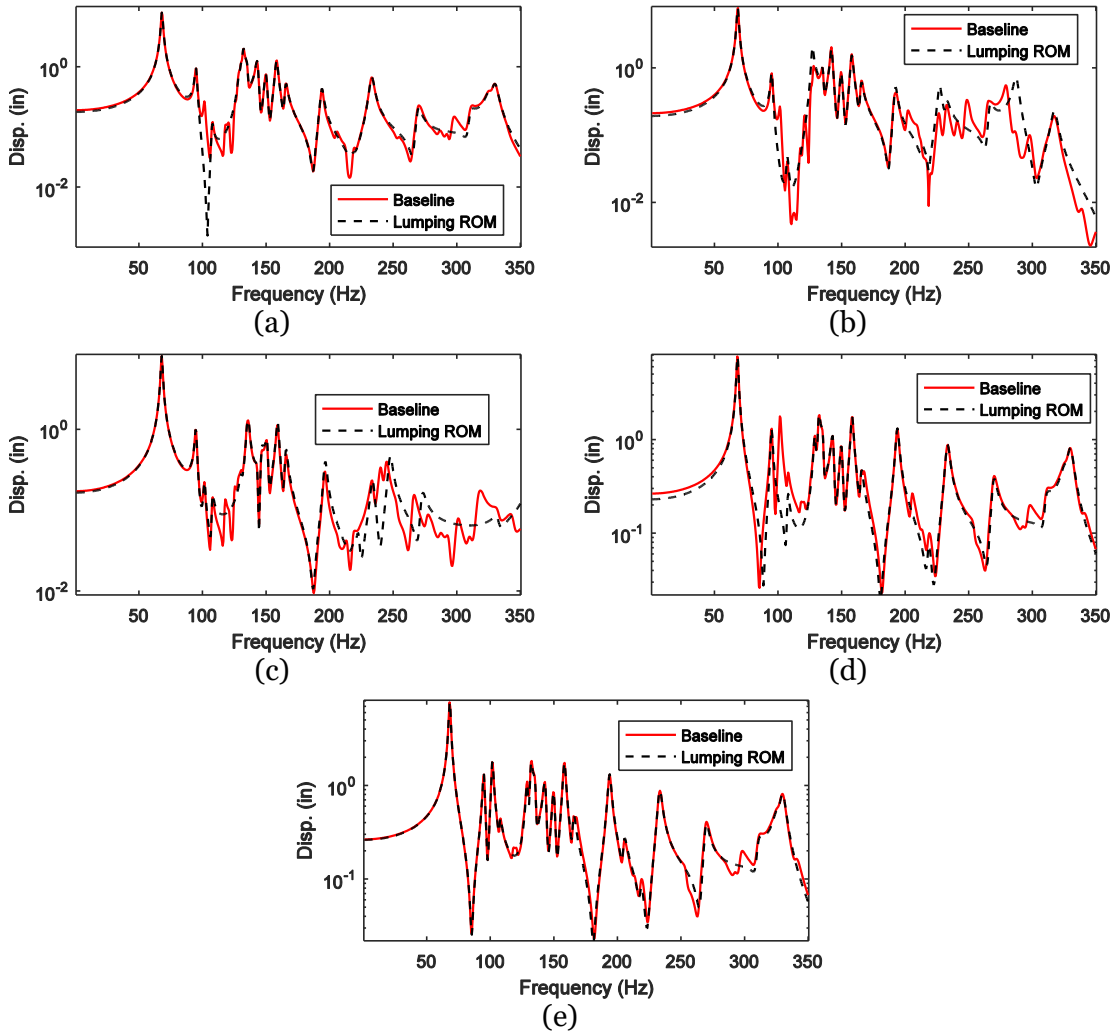

Figure 93 Comparisons of frequency responses at the middle of Bay 4 obtained with the component-centric ROM and with the appropriate baseline model for (a) nominal thickness/ uniform pressure, (b) 80% of the nominal thickness/uniform pressure, (c) 120% of the nominal thickness and uniform pressure, (d) nominal thickness and triangular pressure distribution, (e) same as (d) but ROM includes mode 3

4.3.5 Computational Benefits

As discussed in section 4.1, the Craig-Bampton based approaches only provide a marginal reduction of the number of modes necessary, say 30 to 35 for Bay 4, over the

consideration of all 45 active (i.e., with a non-negligible modal force) linear modes in the band. On the contrary, the modal lumping based approaches lead to much more compact reduced order models: less than 20 modes are sufficient to obtain excellent approximations of the frequency response functions of the middle points of Bay 4, see Fig. 81, and Bay 1, see Fig. 82. In fact, this observation is true for all bays as can be seen from Table 6.

The reduction of the number of modes observed in Table 6, by 12%-43% depending on the bay analyzed, is potentially quite valuable for the linear structures considered here but is likely to have a dramatic impact when considering the nonlinear geometric ROMs developed within the last decade. Therefore, it is intended to expand the modal lumping method to nonlinear settings and the discussion will be presented in the next chapter.

Table 6

Computational Cost Estimates for Linear ROMs of the Various Bays

Bay	Modal Selection	Lumping Method	mode reduction (%)
1	27	20	26%
2	24	18	25%
3	31	19	39%
4	21	17	19%
5	30	17	43%
6	28	17	39%
7	26	16	38%
8	17	15	12%
9	29	18	38%

4.4 Validation on the Beam Model

The beam model that shares similar features of the 9-bay panel was created as a simple test structure for nonlinear analysis. For completeness, the modal lumping method is also applied to it with mode 4 lumped onto mode 3 following the process in section 4.3. Shown in Fig. 94 is a comparison of the ROM transfer functions resulting from the

loading with spatial distribution specified in Chapter 3 and varying harmonically with time. The response of the ROM without mode 4 (the black curve) is significantly different from the reference demonstrating the need to retain it in some manner. Performing a modal lumping of this mode on mode 3 leads to a near perfect match with the reference results. These results demonstrate that the modal lumping method performs very well for the beam model in the linear case. The validation results considering panel 2 to 4 of the beam as the β component accordingly are presented in Fig. 95 to 97.

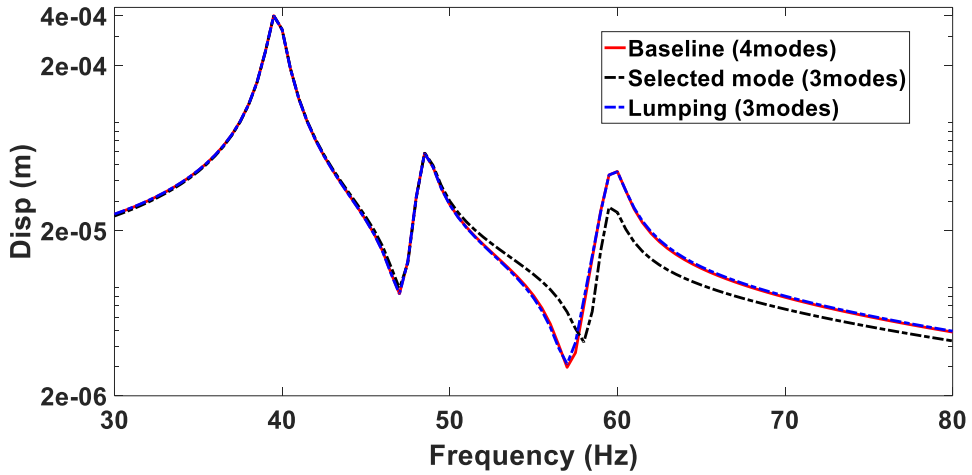

Figure 94 Magnitudes of the frequency responses at the node with max. disp. in the first bay of the beam

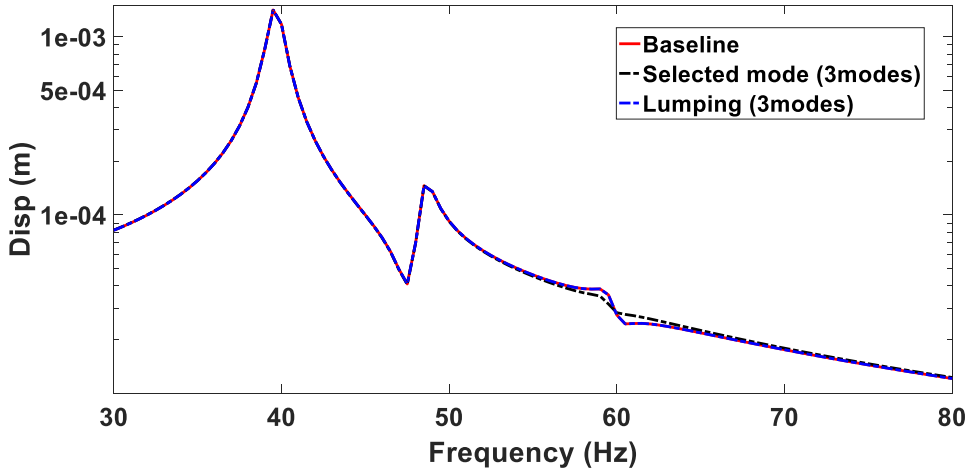

Figure 95 Magnitudes of the frequency responses at the node with max. disp. in the second bay of the beam

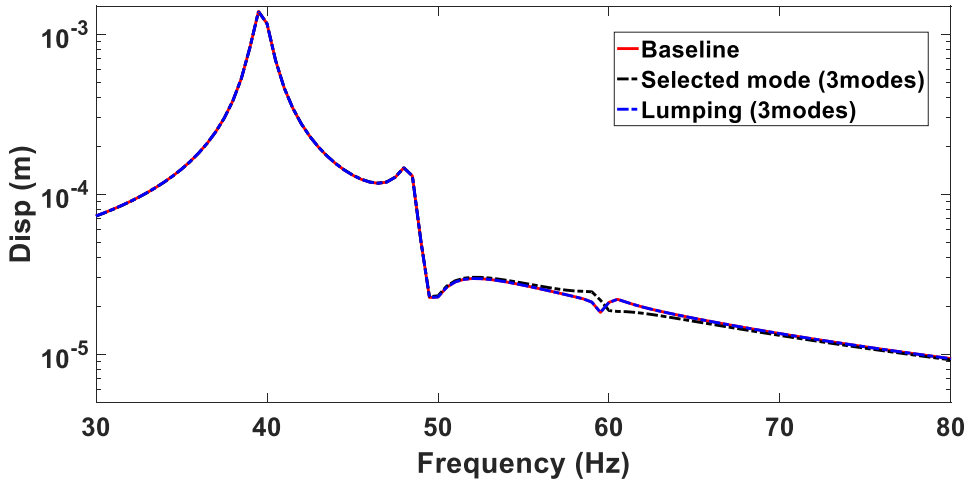

Figure 96 Magnitudes of the frequency responses at the node with max. disp. in the third bay of the beam

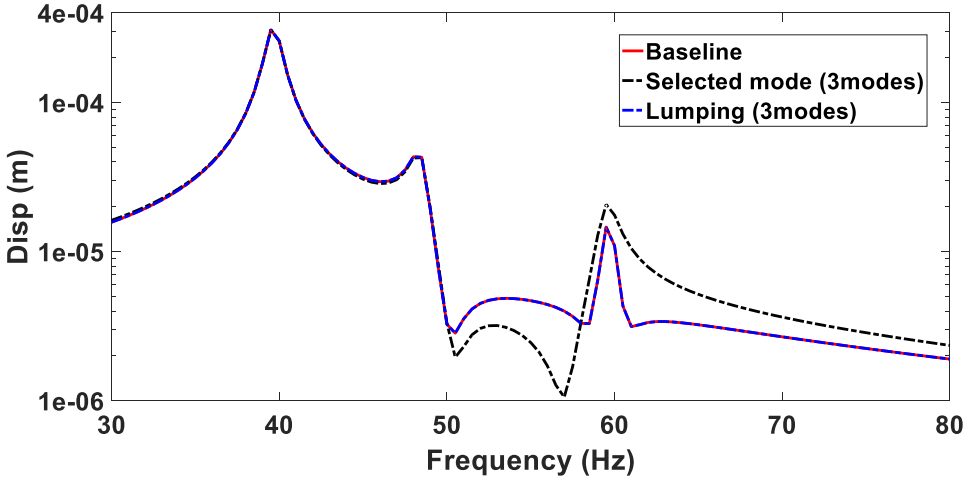

Figure 97 Magnitudes of the frequency responses at the node with max. disp. in the fourth bay of the beam

4.5 Validation on the Multi-Bay Structure with Identical Bays

Next, it is intended to evaluate the modal lumping method on the original 9-bay panel with identical bays [25, 44]. Table 7 compares the modal reduction in percentage after applying the modal lumping method for the two models. The benefit of reducing the model size is not as significant as that of the different 9-bay panel for the original 9-bay panel. This can be expected since the original panel is symmetric leading to much simpler responses, see Fig. 98, thus the model size after the modal selection process is quite small already and there is not much opportunity to further reduce the model size.

Moreover, the mode shapes of the linear modes are more global, thus less modes can meet the requirements for the “lumping” process.

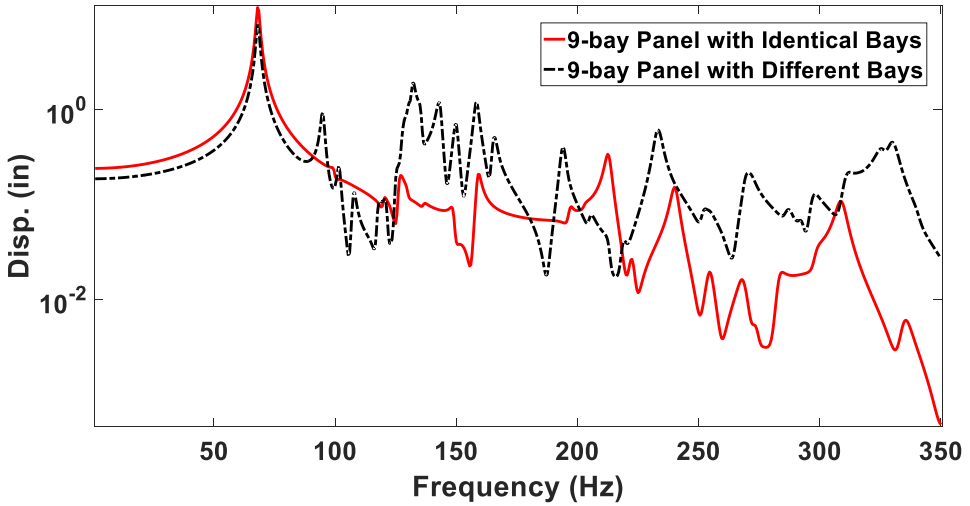

Figure 98 Magnitudes of the frequency responses at the middle point of Bay 4 (the original 9-bay panel and the new 9-bay panel), transverse displacement

Table 7

Comparison of Modal Reduction for the Multi-Bay Structures

Bay	Panel with Identical Bays			Panel with different Bays		
	Modal Selection	Lumping Method	% mode reduction	Modal Selection	Lumping Method	% mode reduction
1	11	11	0%	27	20	26%
2	10	9	10%	24	18	25%
3	13	12	8%	31	19	39%
4	9	8	11%	21	17	19%
5	15	12	20%	30	17	43%
6	9	8	11%	28	17	39%
7	13	13	8%	26	16	38%
8	10	9	10%	17	15	12%
9	11	11	0%	29	18	38%

CHAPTER 5

NONLINEAR COMPONENT-CENTRIC ROM

5.1 Extension of Modal Lumping Method to Nonlinear

Even though, NLROMs are much more expedient than full order finite element models for long simulation times, the computational effort to construct and run them does grow rapidly with the number of basis functions ("modes") used in the representation, or equivalently, with the complexity of the structural model. One remedy proposed in [24] involves eliminating the nonlinear terms in the ROM that are expected to have a small contribution to the nonlinear restoring forces. Another strategy, potentially complementary of this approach, is considered here that is based on the concept of component-centric ROMs introduced in Chapter 4 for linear structural models. Such ROMs are designed to provide an accurate prediction of the linear response of a part of structure (referred to as the "β" component) while allowing a lower accuracy in the rest of the structure (referred to as the "α" component). The advantage of this method over the standard ROMs/modal models is a significant reduction (by 60% for the 9-bay example]) of the number of generalized coordinates needed for stiffened structures. Moreover, the component-centric ROMs corresponding to different parts of the structure are uncoupled and thus can be run in parallel to provide an accurate prediction of the response of the structure in a smaller wall time. In this light, this chapter focuses on extending the linear component-centric ROMs to the nonlinear geometric situation.

5.1.1 Another Aspect of Modal Lumping: Modal Rotation

The lumping process can also be recognized as originating from a rotation of the two modes $\underline{U}^i$ and $\underline{U}^j$, defined in the entire structure (i.e., in both α and β components) as

$$\underline{U}^i = \begin{bmatrix} \underline{U}_\alpha^i \\ \underline{U}_\beta^i \end{bmatrix} \text{ and } \underline{U}^j = \begin{bmatrix} \underline{U}_\alpha^j \\ \underline{U}_\beta^j \end{bmatrix} \sim \begin{bmatrix} \underline{U}_\alpha^j \\ a\underline{U}_\beta^i \end{bmatrix} \tag{81}$$

Since the natural frequencies of these two modes are assumed to be identical, the structure has repeated frequencies (assumed two here) and thus any linear combination of these two modes is also a mode. On this basis, introduce the two new modes:

$$\begin{aligned} \underline{\tilde{U}}^i &= (\underline{U}^i + a\underline{U}^j)/\sqrt{1+a^2} \\ \underline{\tilde{U}}^j &= (a\underline{U}^i - \underline{U}^j)/\sqrt{1+a^2} \end{aligned} \tag{82}$$

which are readily shown to exhibit the same orthonormality properties as the original modes $\underline{U}^i$ and $\underline{U}^j$, i.e.,

$$\begin{gathered} \left(\underline{\tilde{U}}^i\right)^T \boldsymbol{M}\, \underline{\tilde{U}}^i = 1\ ;\ \ \left(\underline{\tilde{U}}^j\right)^T \boldsymbol{M}\, \underline{\tilde{U}}^j = 1\ ;\ \ \left(\underline{\tilde{U}}^i\right)^T \boldsymbol{M}\, \underline{\tilde{U}}^j = 0\ ;\left(\underline{\tilde{U}}^i\right)^T \boldsymbol{M}\, \underline{U}^l = \\ 0\ ;\left(\underline{\tilde{U}}^j\right)^T \boldsymbol{M}\, \underline{U}^l = 0 \end{gathered} \tag{83}$$

where $\boldsymbol{M}$ denotes the mass matrix of the entire structure and the index l of the mode $\underline{U}^l$ is such that $l \neq i$ or j. Introducing Eq. (81) in Eq. (82), it is found that

$$\begin{aligned} \underline{\tilde{U}}^i &= \begin{bmatrix} \underline{U}_\alpha^i + a\underline{U}_\alpha^j \\ (1+a)\underline{U}_\beta^i \end{bmatrix} /\sqrt{1+a^2} \\ \underline{\tilde{U}}^j &= \begin{bmatrix} a\underline{U}_\alpha^i - \underline{U}_\alpha^j \\ \underline{0} \end{bmatrix} /\sqrt{1+a^2} \end{aligned} \tag{84}$$

Note that the elements in $\underline{\tilde{U}}^j$ corresponding to the β component are all zero. Thus, the displacement in that component is not a function of the generalized coordinate $\tilde{q}_j$ associated with the mode $\underline{\tilde{U}}^j$. Moreover, this generalized coordinate is uncoupled to $\tilde{q}_i$ and the remaining generalized coordinates q_l, $l \neq i$ or j, because of the orthogonality properties of Eq. (84). Thus, the value/time history of $\tilde{q}_j$ does not appear anywhere in the prediction of the response of the β component (it will however appear in the displacement of the α component which is not of concern here) and mode j has indeed

been lumped into mode i. Note finally that the governing equation for the generalized coordinate $\tilde{q}_i$ can be shown to reduce to Eq. (68) with $\bar{q}_i = \tilde{q}_i\sqrt{1+a^2}$ so that the above two perspectives on lumping are consistent.

Again, as discussed in section 4.4, to optimize the accuracy of the approximation, the lumping of two modes should be done on the mode of largest modal coordinate and/or the one with the most representative deflection in the β component of the modes to be lumped. Moreover, the lumping of multiple modes on one of them proceeds as described above with two modes under the same assumptions of close natural frequencies and similar modal deflection in the β component for all modes involved.

5.1.2 A "Closure" Type Scheme

The construction of a nonlinear component-centric ROM proceeds as in the linear case, see Chapter 3, with first the modal selection and then possible modal lumping.

Regarding modal selection, note first that the response estimate R_i of Eq. (60) will in general not be a reliable estimate of the contribution of mode i in the dynamic response. However, the *relative* magnitudes of these estimates may still provide a correct ordering of the importance of the various modes.

The modal lumping also starts as in section 4.4.1 with a rotation of the modes to be lumped leading to elements in $\underline{\tilde{U}}^j$ corresponding to the β component that are all zero. Thus, the displacements in that component are not functions of the generalized coordinate $\tilde{q}_j$. Moreover, as in the linear case, this coordinate is not present in the linear stiffness terms $K_{ij}^{(1)}q_j$ of the selected modes *but* it appears in their quadratic and cubic terms which couples the modes. Thus, the generalized coordinate $\tilde{q}_j$ is transformed into an unobservable but active coordinate; it remains present in the ROM equations of motion even though it has no direct (through $\underline{\tilde{U}}^j$) effect**.**

To truly eliminate the lumped coordinate $\tilde{q}_j$, it is proposed here to express it in terms of the other rotated coordinate(s) $\tilde{q}_i$ because these two modes have close (assumed equal) natural frequencies and thus strong interactions between them is expected, stronger than with other modes. This approximation will be referred to as a "closure" scheme as it allows to proceed with the solution of the equations of motion without $\tilde{q}_j$. In selecting the form of the approximation, it was imposed that the form of the equations of motion, remain, i.e., that it is linear in the inertia and cubic in the stiffness terms. This structure can be achieved only if the approximation is memoryless and linear, i.e.,

$$\tilde{q}_j(t) = c_0 + c_1 \tilde{q}_i(t) \tag{85}$$

The estimation of the coefficients c_0 and c_1 can be achieved from a limited set of nonlinear static or dynamic computations as discussed in the ensuing validations.

5.2 Validation on the Beam Model

The bay 1 (containing node 1-11) is first considered as the component of interest (the β component). Since mode 3 is slightly larger than mode 4 in this bay, see Fig. 59, mode 3 was selected as the dominant mode and thus mode 4 was selected for either elimination or lumping. A rotation of modes 3 and 4 was first performed as in Eq. (82) with the factor a = 0.9641 ≈ 1 as expected from Fig. 59. Figure 99 illustrates the rotation of the mode shapes for modes 3 and 4, comparing the original linear modes to the rotated ones. As shown in Fig. 99(b), mode 4 after rotation, has nearly zero deformation in β. The component-centric ROMs could then formally be expressed in terms of $\tilde{q}_3$ and $\tilde{q}_4$ with the transformation (see Eq. (82))

$$\begin{aligned} q_3 &= (\tilde{q}_3 + a\tilde{q}_4)/\sqrt{1+a^2} \\ q_4 &= (a\tilde{q}_3 - \tilde{q}_4)/\sqrt{1+a^2} \end{aligned} \tag{86}$$

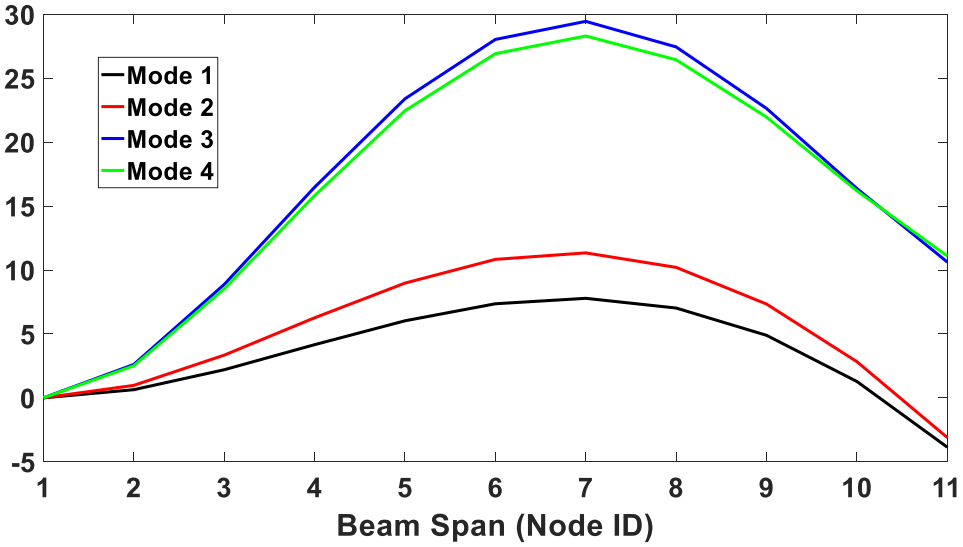

(a)

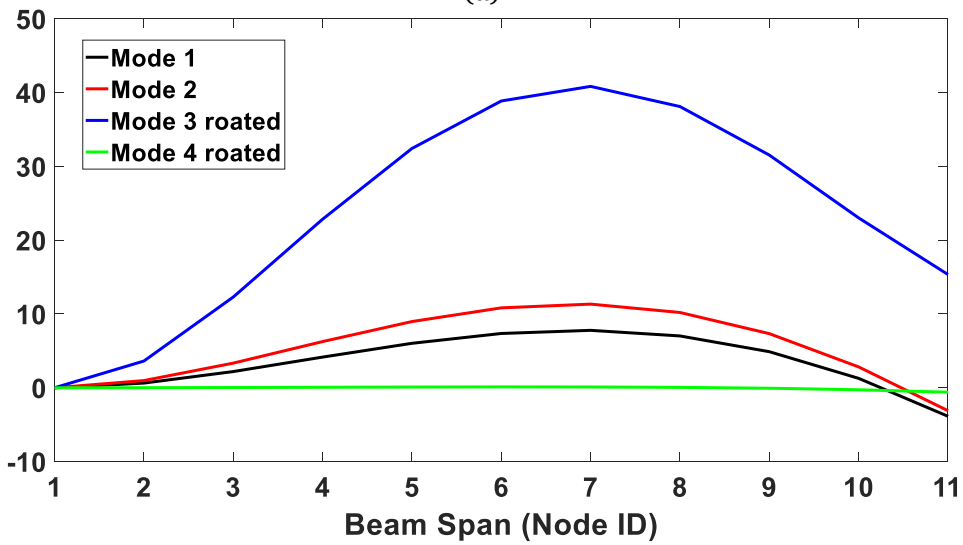

(b)

Figure 99 Lowest 4 linear modes of the beam in bay 1 (a) before rotation, (b) after rotation

Since the linear component-centric ROM provides a very close approximation of the full modal model (see section 4.5), the investigation proceeded next with the construction and assessment of its nonlinear counterpart. In addition to the step carried out above, it was also necessary to establish the "closure" approximation of the generalized coordinate $\tilde{q}_4$ in terms of $\tilde{q}_3$, see Eq. (85). To estimate the corresponding coefficients c_0 and c_1 a short time simulation with the full size nonlinear ROM was conducted and the scatter

plot of the modal responses corresponding to the linear modes 3 and 4 was obtained, see Fig. 100(a). From these result, the simple linear fit

$$\tilde{q}_4 \approx 0.9\tilde{q}_3 \tag{87}$$

was obtained. Note c_0 needs to be ignored when estimations were conducted using nonlinear static solutions. Similar results can be obtained from a set of nonlinear static solutions with the full-size ROM (see Fig. 100(b)) with the maximum transverse displacement varying from 0.5 to 3 thickness of the beam structure and much less computational cost. In fact, a similar process can be achieved *without* relying on the full ROM by constructing the same static responses from the finite element model and projecting them on the rotated modes 3 and 4. Combining Eqs (86) and (87) led to the final change of variables

$$\begin{aligned} q_3 &= \tilde{q}_3(1 + 0.9\,a)/\sqrt{1+a^2} \\ q_4 &= \tilde{q}_3(a - 0.9)/\sqrt{1+a^2} \end{aligned} \tag{88}$$

which was performed on the nonlinear ROM leading to the desired nonlinear component-centric ROM.

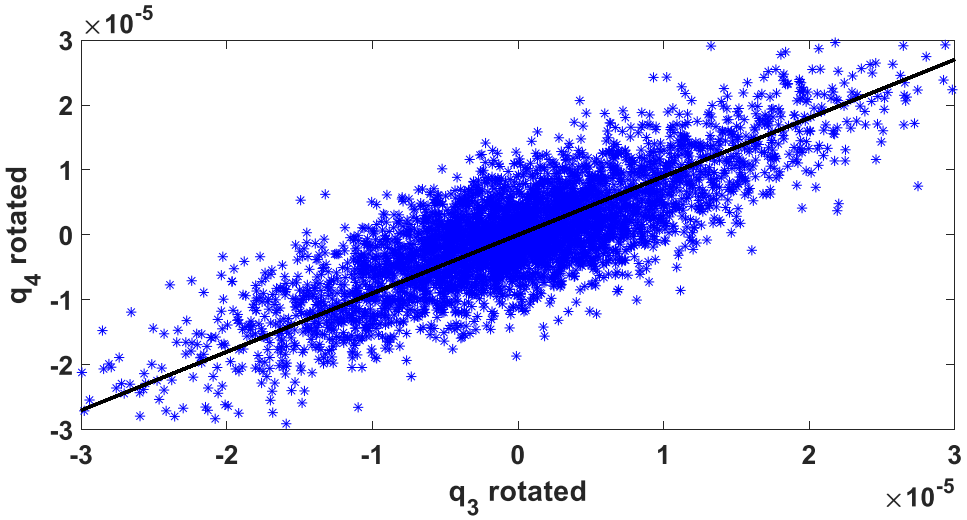

(a)

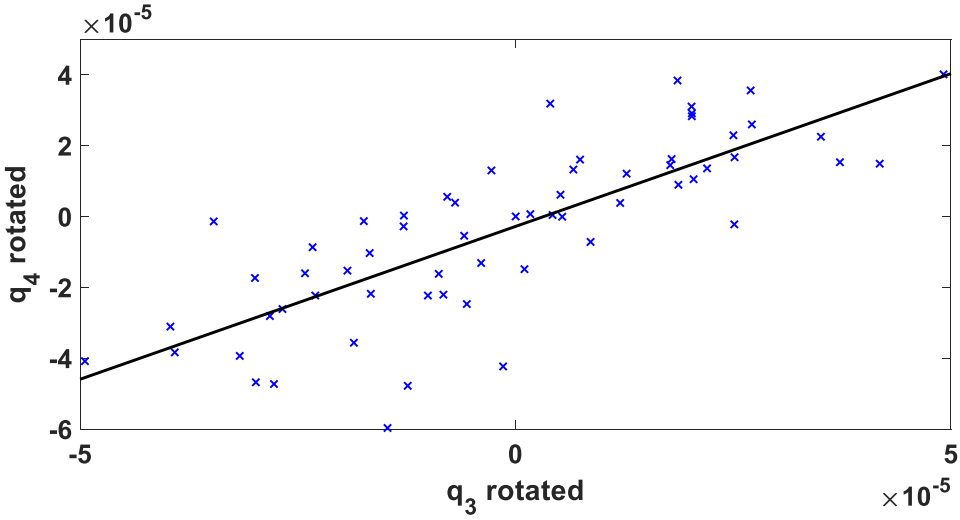

(b)

Figure 100 Estimated relation between modal responses of the rotated modes 3 and 4 from (a) a very short time dynamic simulation (b) a set of nonlinear static solutions

The evaluation of the nonlinear component-centric ROM accuracy was conducted by comparing the power spectral densities (PSD) of the transverse (T3) and in-plane (T1) responses of the node with the maximum displacement in bay 1 as shown in Fig. 101. Shown on these figures are the corresponding predictions of the nonlinear ROM with the original mode 4 (i) ignored and (ii) lumped onto the rotated mode 3. Clearly, the matching of the responses (both T1 and T3) is very good for the latter model while rather poor for the former one. These first results strongly support the applicability and accuracy of the proposed nonlinear component centric ROM construction. Similar results are obtained with panel 2, 3, and 4 as β component shown in Fig. 102 to 104. Note that the knowledge of the displacements provides a complete description of the bay 1 behavior including stresses and strains which can be evaluated at any point from the generalized coordinates as described in section 2.3. To assess the appropriateness of component-centric models for the prediction of the stresses in the structure, the corresponding stress distribution in the beam obtained in both linear and nonlinear cases were estimated and compared to their full ROM/NLROM counterparts. In all, linear and nonlinear, cases, an excellent match was observed, see Fig. 105,

demonstrating that a component-centric model predicting well the displacement field in the β component also predicts well the stresses in that component.

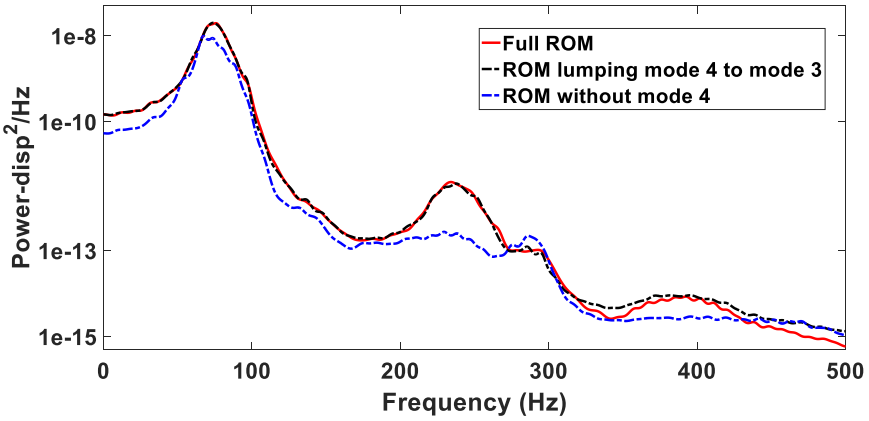

(a)

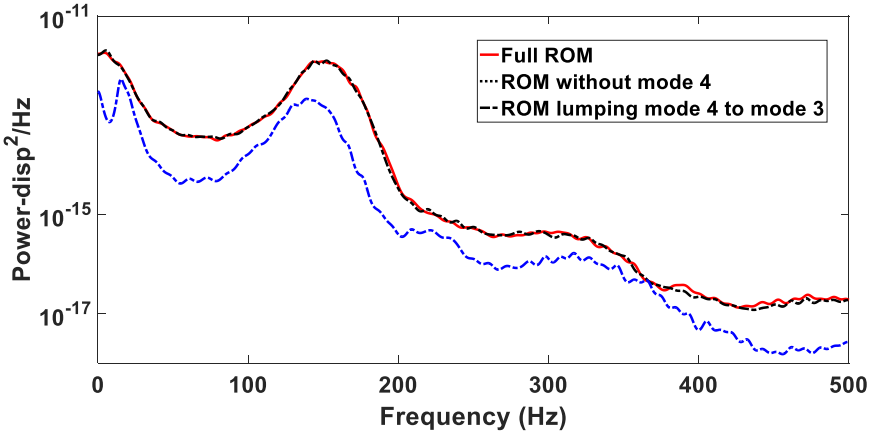

(b)

Figure 101 Power spectral densities of the (a) transverse and (b) in-plane deflections at the node with max. disp. in the first bay (β)

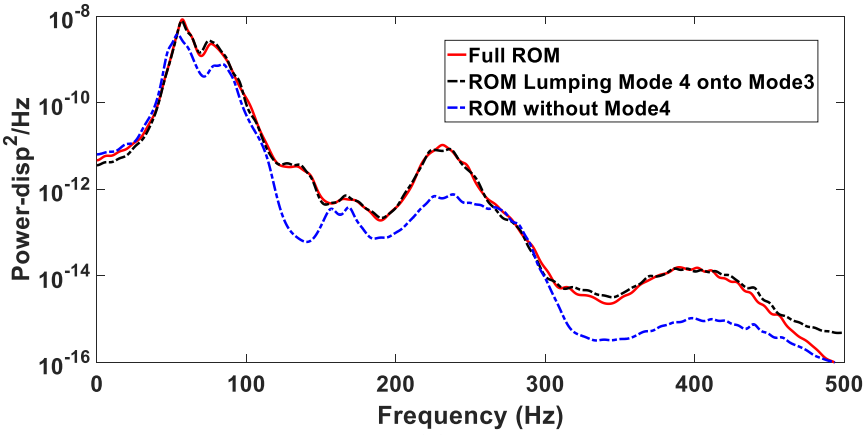

(a)

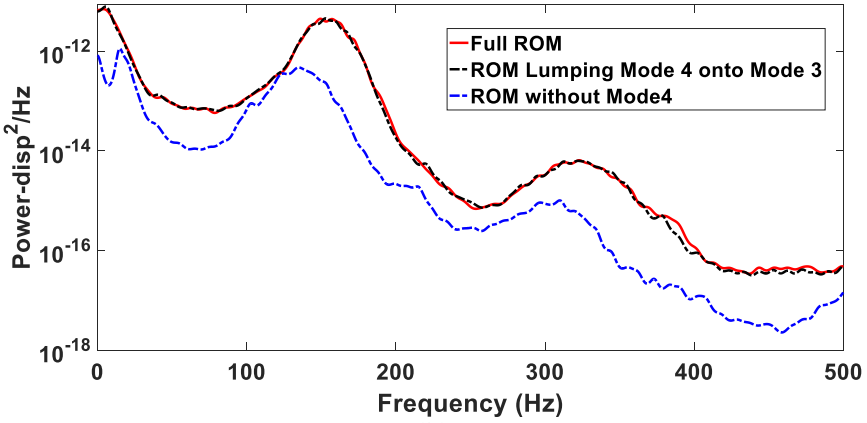

(b)

Figure 102 Power spectral densities of the (a) transverse and (b) in-plane deflections at the node with max. disp. in the second bay (β)

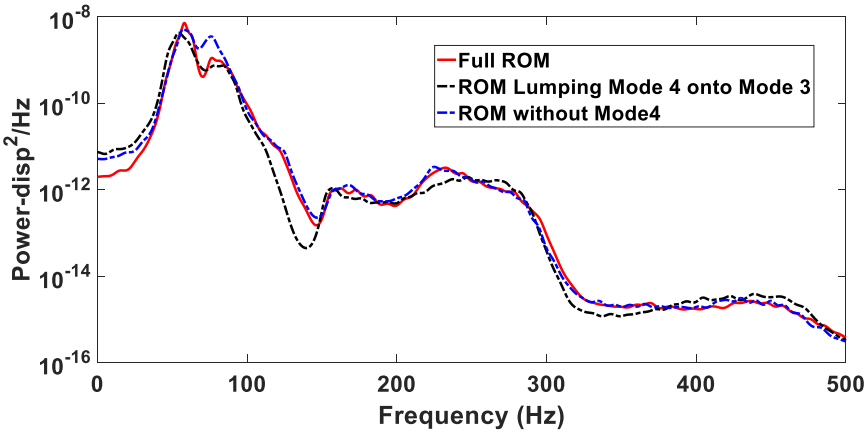

(a)

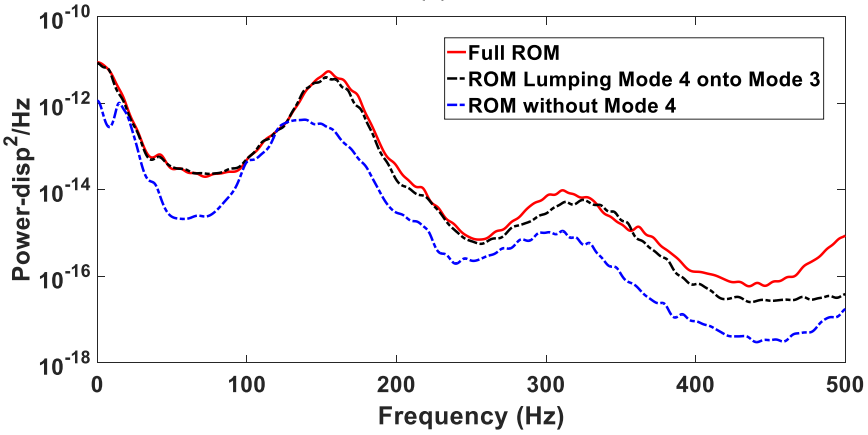

(b)

Figure 103 Power spectral densities of the (a) transverse and (b) in-plane deflections at the node with max. disp. in the third bay (β)

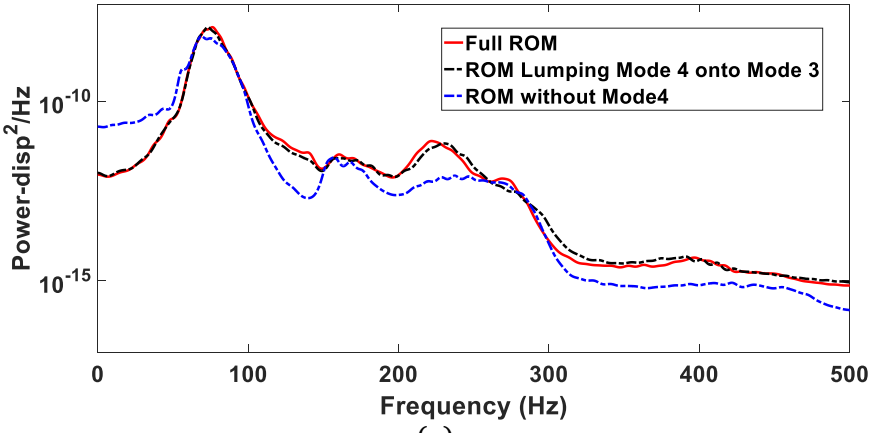

(a)

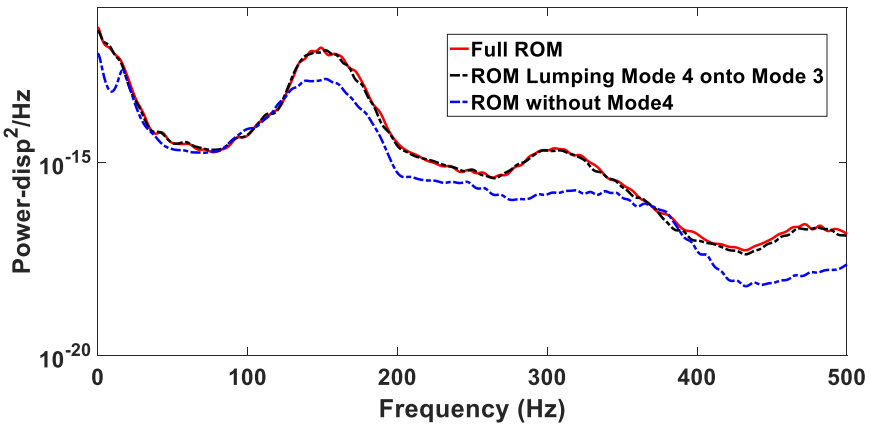

(b)

Figure 104 Power spectral densities of the (a) transverse and (b) in-plane deflections at the node with max. disp. in the fourth bay (β)

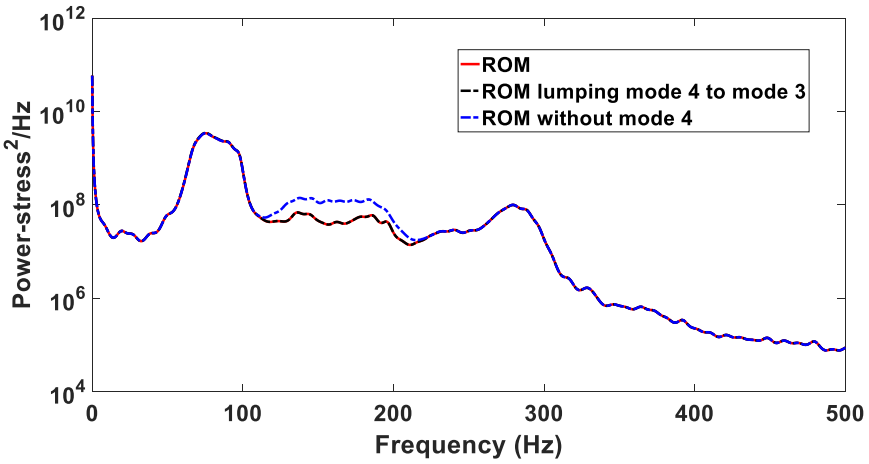

(a)

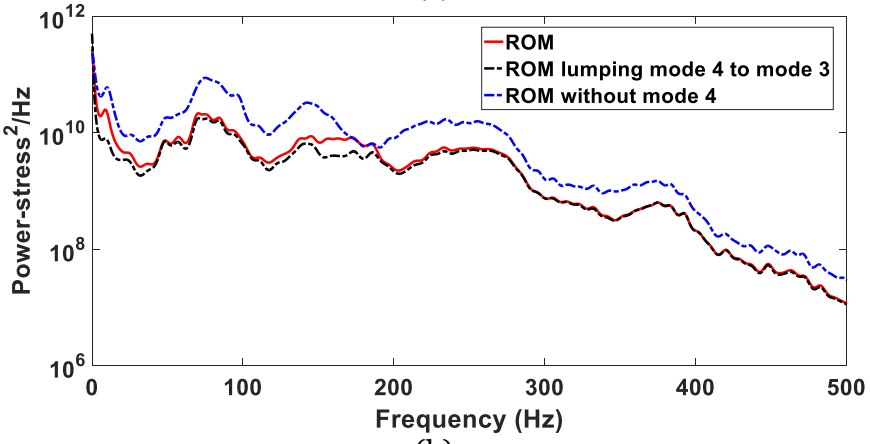

(b)

Figure 105 Power spectral densities of the second Piola-Kirchhoff stress Sxx for the (a) linear and (b) nonlinear dynamic cases at the node with max. disp. in the first bay (β)

5.3 Validation on the Multi-Bay Structure

Same as the linear case considering bay 4 as the β component, 5 modes (i.e., modes 9, 12, 15, 22, and 40) of frequencies 129.01, 135.43, 143.17, 195.42 and 292.14Hz were lumped first. Figure 106 illustrates the rotation of the mode shapes for the two linear modes 10 and 11, comparing the original linear modes to the rotated ones. As shown in the two-top right figure, the mode after rotation has nearly zero deformation in β. The contributions of the first two modes were lumped on the one of mode 11 of frequency 132.00Hz while those of the last 3 modes were lumped, respectively, with those of modes 14, 21 and 42 of frequencies equal to 142.23, 193.86 and 296.87Hz.

To estimate the corresponding coefficients c_0 and c_1 in Eq. (85) for each mode pair mentioned above, a series of nonlinear static simulation with the full size nonlinear ROM was conducted (full Nastran solutions could also be used and do not require the full ROM) leading to 0.5 – 3 thickness of the panel. For each case, the relation between modal coordinates is estimated via a simple linear fit and the results can be seen in Table 8. Using these approximate linear relations permits the reduction of the model to a 46-mode one.

Table 8

Coefficients of the Linear Relation of Eq. (85), for Bay 1

$\tilde{q}_i$	$\tilde{q}_j$	c_0	c_1
11	9	7e-5	0.51
11	12	7e-5	0.51
14	15	-1e-6	-2.7
21	22	4.8e-5	0.66
40	42	9e-7	-4.6

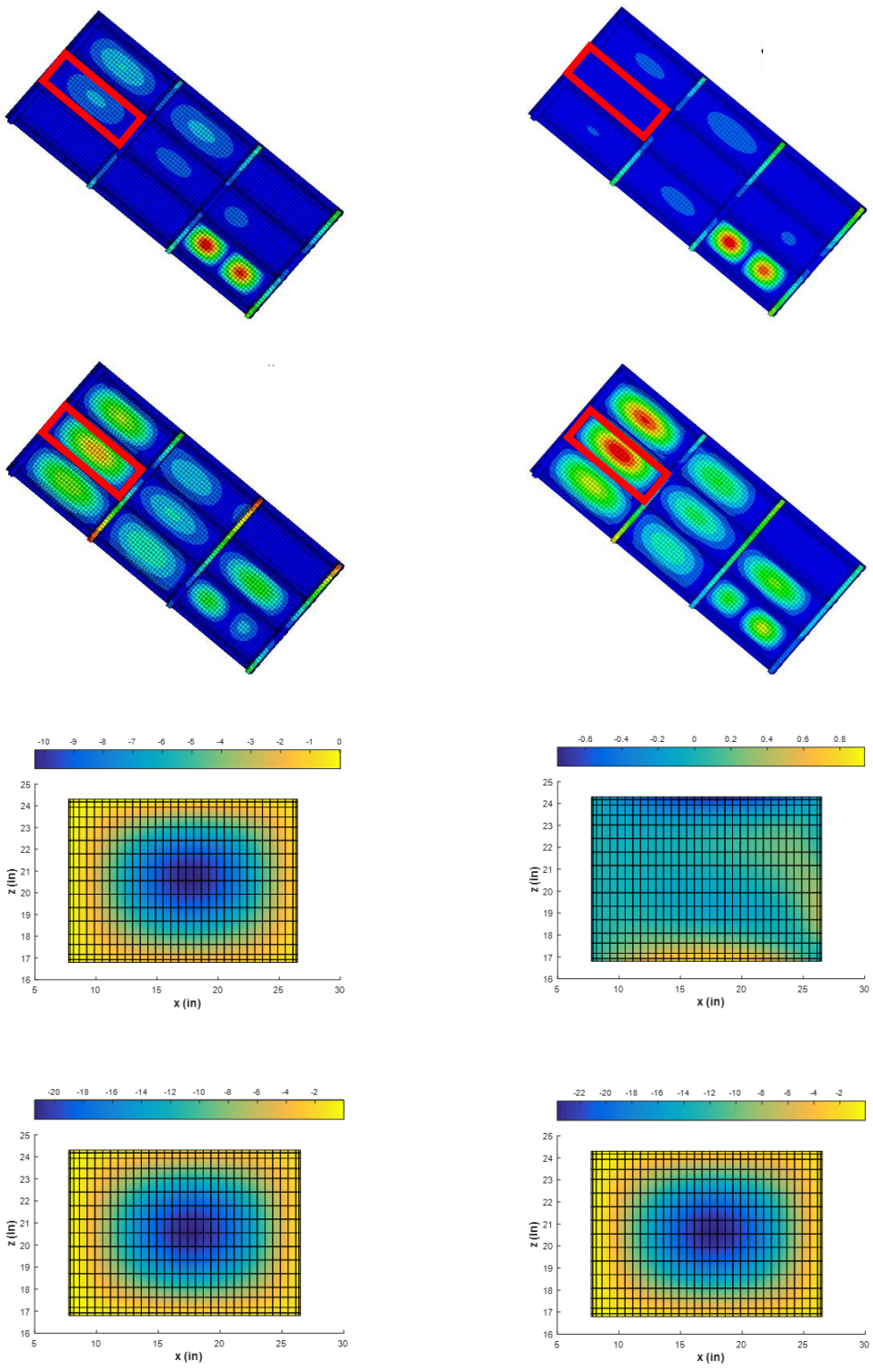

Figure 106 Mode shapes before, $\underline{U}^i$ and $\underline{U}^j$ - left column, and after rotation, $\underline{\tilde{U}}^i$ and $\underline{\tilde{U}}^j$ - right column. (row 1, 2) Entire structure and (row 3, 4) β-component (bay 4) only

To validate the above process, the magnitude of the white noise excitation was selected to achieve a full nonlinear regime. In fact, the average peak transverse displacement was found to be approximately 1 skin panel thicknesses which is well in the geometric nonlinear regime. Then, shown in Fig. 107 are the PSD of the transverse response of Panel 1 center computed using (a) the 74-mode Mono-ROM, (b) the 46 modes model obtained by lumping modes 9, 12, 15, 22, and 40 onto modes 11, 14, 21 and 42, respectively, and (c) the 46 modes obtained by discarding modes 9, 12, 15, 22, and 40 from the 26 selected ones. The response obtained with the lumped model (b) clearly matches much better the Nastran predictions than the latter model. Further, this increase in accuracy is obtained at no cost to the complexity of the model providing a first confirmation of the benefit of modal lumping in leading to accurate but compact ROMs. PSD results for the transverse and in-plane (T2) displacements at the center of all bays can be found in Fig. 108 to 142.

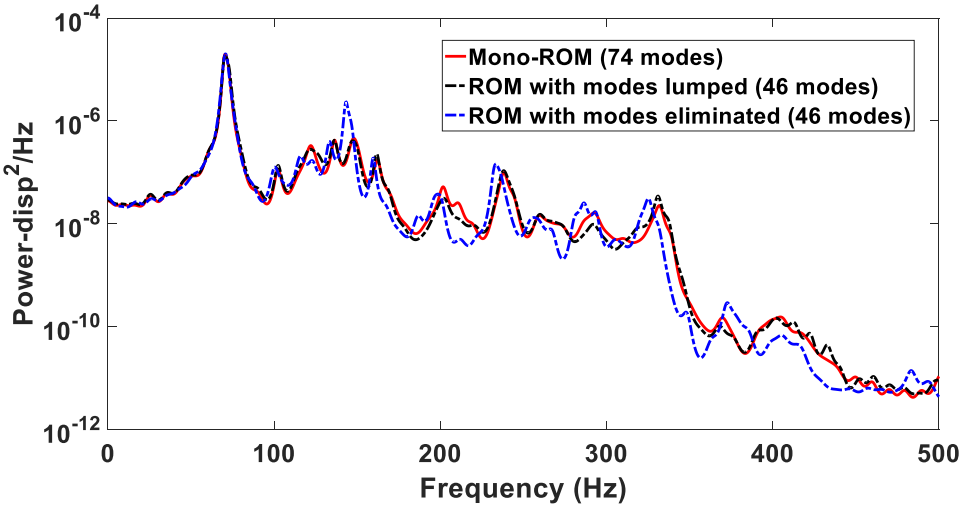

Figure 107 Power spectral densities of the transverse responses of Panel 1 center for OASPL of 136dB obtained with the 74-mode full ROM (red), the component-centric 46-mode ROM with 7 linear modes lumped (black), the 46-mode ROM with the same linear modes eliminated (blue)

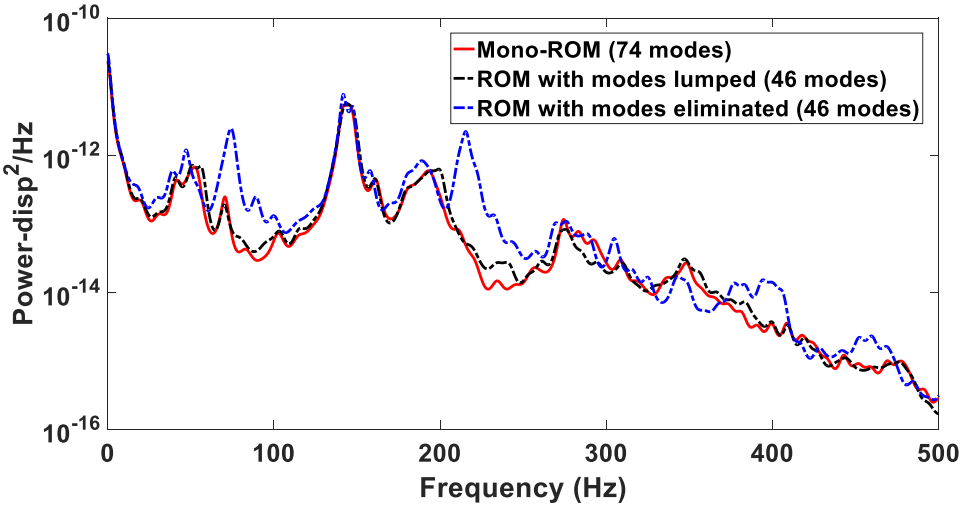

Figure 108 Power spectral densities of the in-plane (T2) responses of Panel 1 center for OASPL of 136dB obtained with the 74-mode full ROM (red), the component-centric 46-mode ROM with 7 linear modes lumped (black), the 46-mode ROM with the same linear modes eliminated (blue)

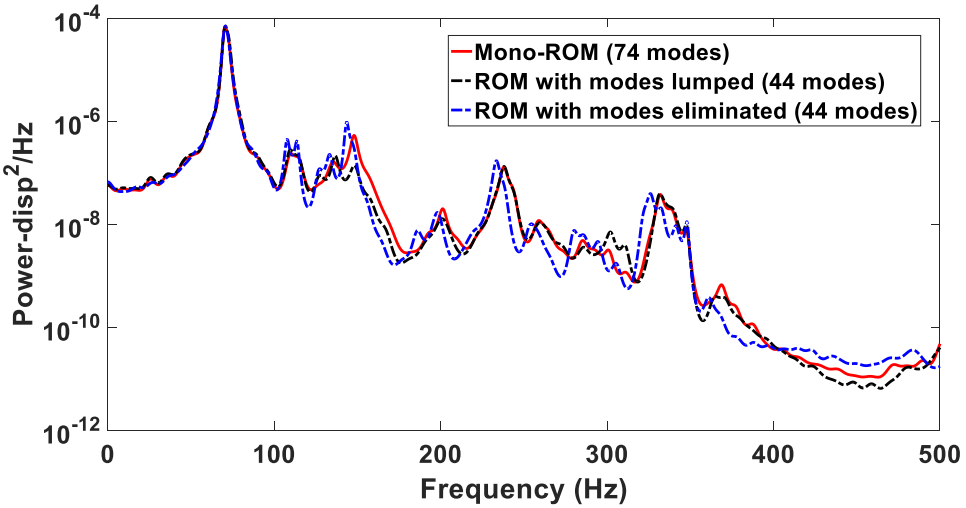

Figure 109 Power spectral densities of the transverse responses of Panel 2 center for OASPL of 136dB obtained with the 74-mode full ROM (red), the component-centric 44-mode ROM with 6 linear modes lumped (black), the 44-mode ROM with the same linear modes eliminated (blue)

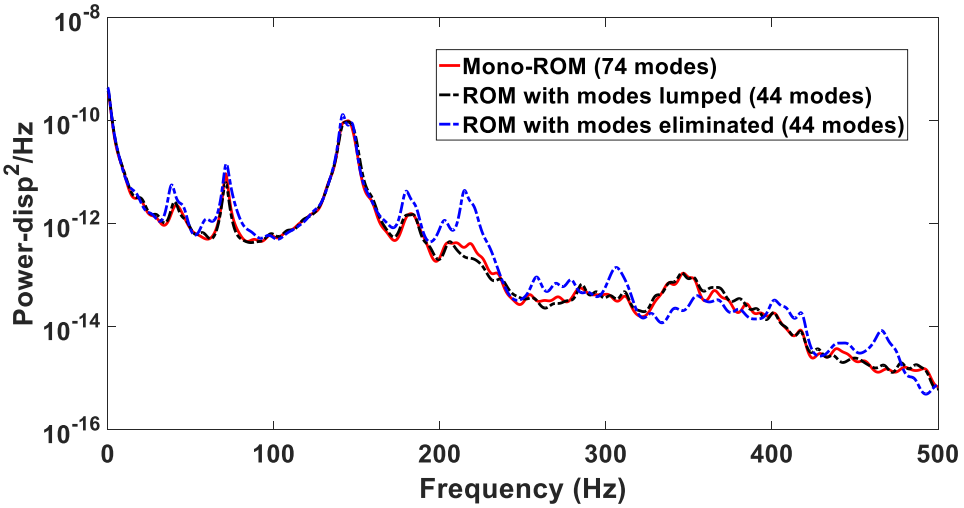

Figure 110 Power spectral densities of the in-plane (T2) responses of Panel 2 center for OASPL of 136dB obtained with the 74-mode full ROM (red), the component-centric 44-mode ROM with 6 linear modes lumped (black), the 44-mode ROM with the same linear modes eliminated (blue)

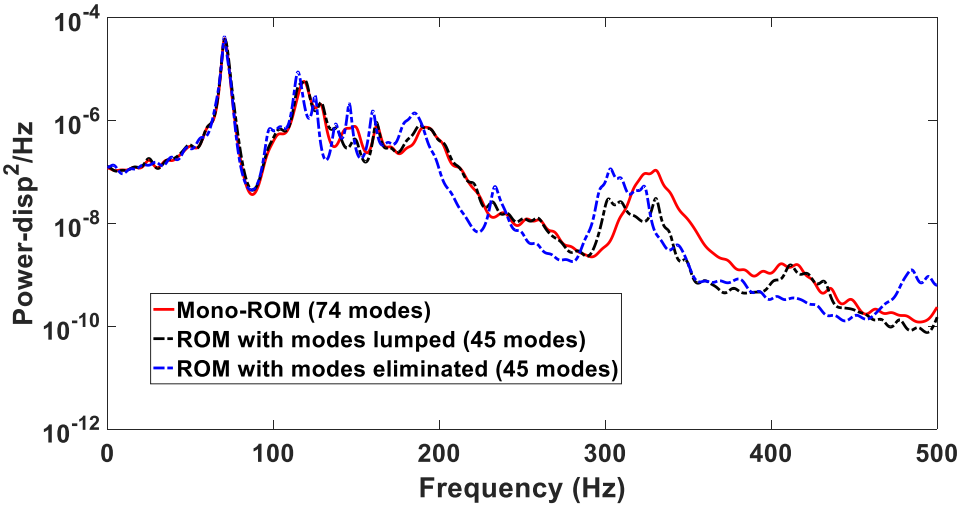

Figure 111 Power spectral densities of the transverse responses of Panel 3 center for OASPL of 136dB obtained with the 74-mode full ROM (red), the component-centric 45-mode ROM with 12 linear modes lumped (black), the 45-mode ROM with the same linear modes eliminated (blue)

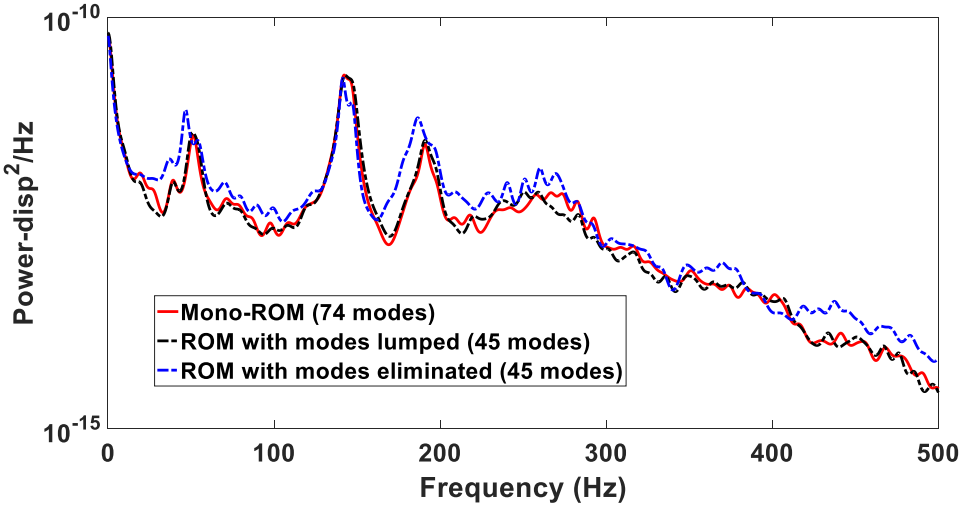

Figure 112 Power spectral densities of the in-plane (T2) responses of Panel 3 center for OASPL of 136dB obtained with the 74-mode full ROM (red), the component-centric 45-mode ROM with 12 linear modes lumped (black), the 45-mode ROM with the same linear modes eliminated (blue)

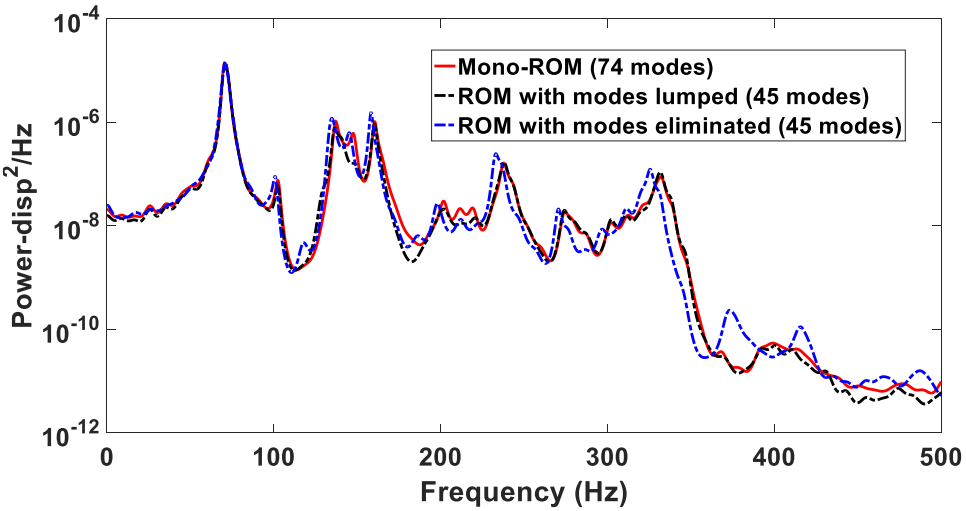

Figure 113 Power spectral densities of the transverse responses of Panel 4 center for OASPL of 136dB obtained with the 74-mode full ROM (red), the component-centric 45-mode ROM with 4 linear modes lumped (black), the 45-mode ROM with the same linear modes eliminated (blue)

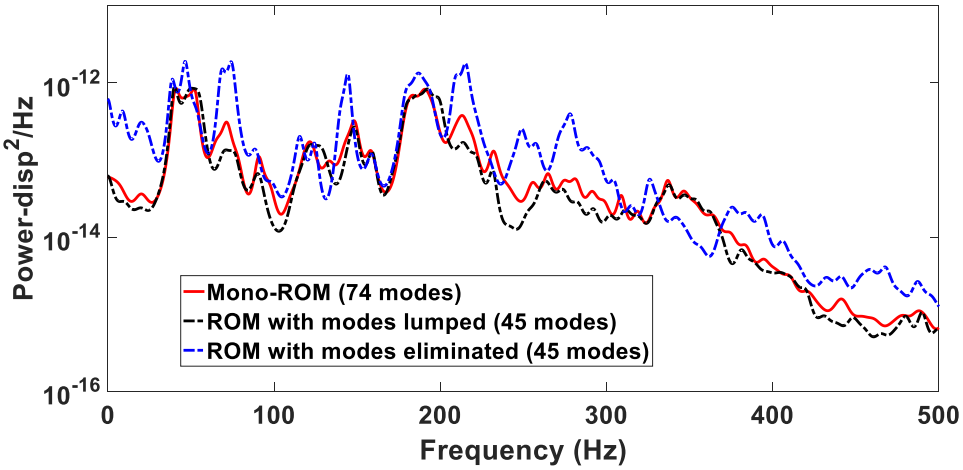

Figure 114 Power spectral densities of the in-plane (T2) responses of Panel 4 center for OASPL of 136dB obtained with the 74-mode full ROM (red), the component-centric 45-mode ROM with 4 linear modes lumped (black), the 45-mode ROM with the same linear modes eliminated (blue)

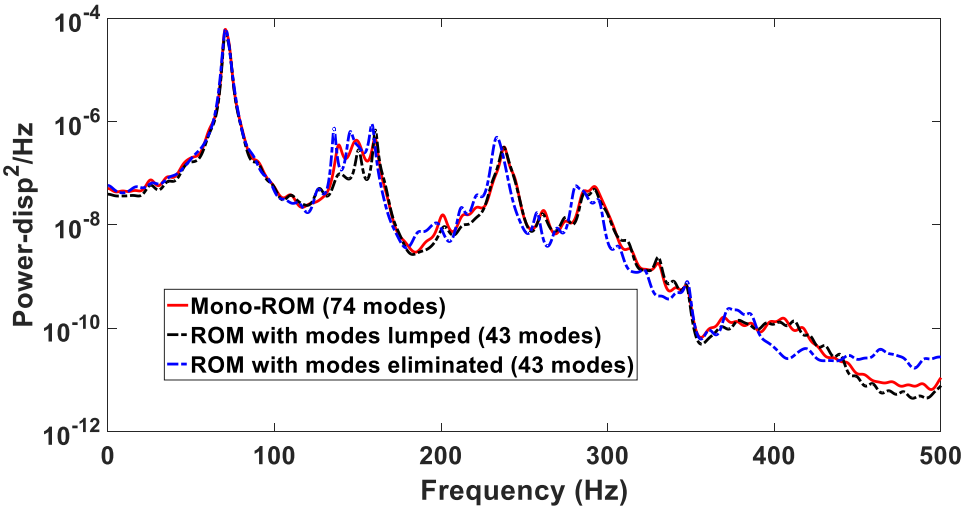

Figure 115 Power spectral densities of the transverse responses of Panel 5 center for OASPL of 136dB obtained with the 74-mode full ROM (red), the component-centric 43-mode ROM with 13 linear modes lumped (black), the 43-mode ROM with the same linear modes eliminated (blue)

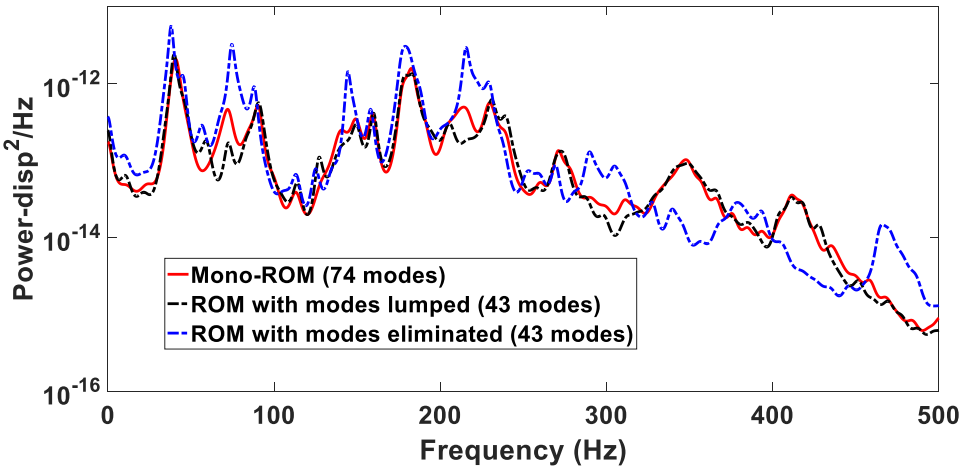

Figure 116 Power spectral densities of the in-plane (T2) responses of Panel 5 center for OASPL of 136dB obtained with the 74-mode full ROM (red), the component-centric 43-mode ROM with 13 linear modes lumped (black), the 43-mode ROM with the same linear modes eliminated (blue)

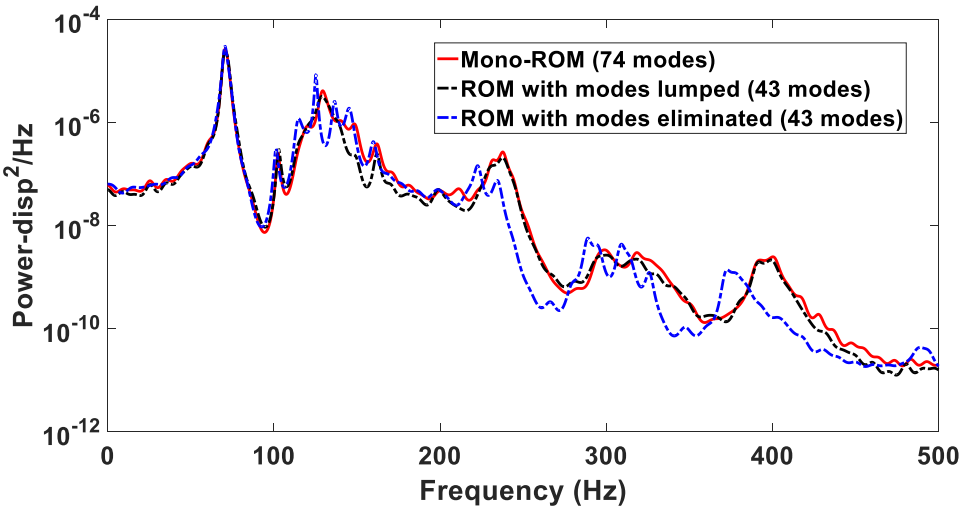

Figure 117 Power spectral densities of the transverse responses of Panel 6 center for OASPL of 136dB obtained with the 74-mode full ROM (red), the component-centric 43-mode ROM with 17 linear modes lumped (black), the 43-mode ROM with the same linear modes eliminated (blue)

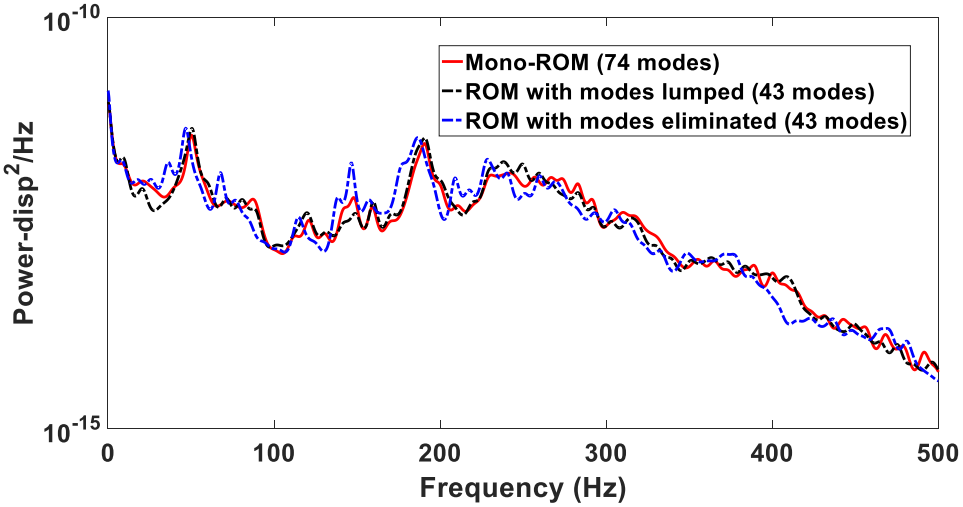

Figure 118 Power spectral densities of the in-plane (T2) responses of Panel 6 center for OASPL of 136dB obtained with the 74-mode full ROM (red), the component-centric 43-mode ROM with 17 linear modes lumped (black), the 43-mode ROM with the same linear modes eliminated (blue)

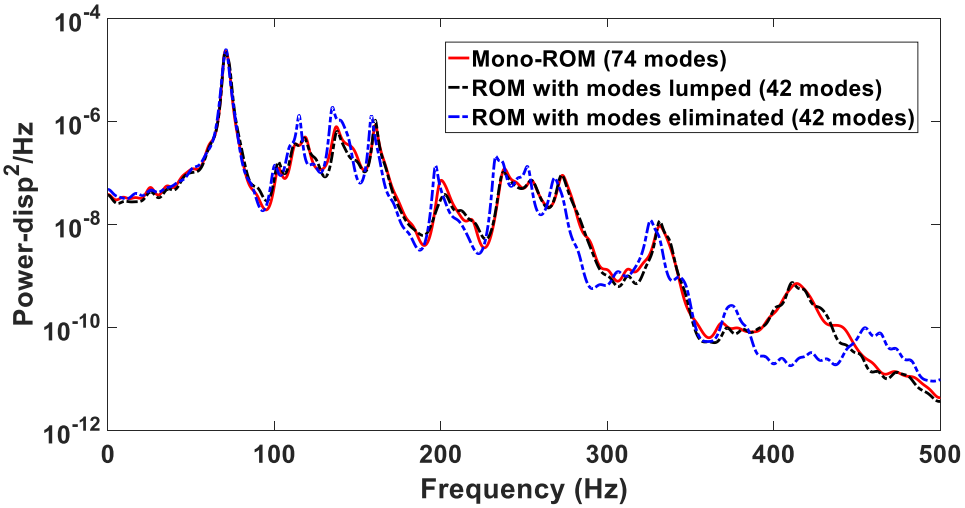

Figure 119 Power spectral densities of the transverse responses of Panel 7 center for OASPL of 136dB obtained with the 74-mode full ROM (red), the component-centric 42-mode ROM with 10 linear modes lumped (black), the 42-mode ROM with the same linear modes eliminated (blue)

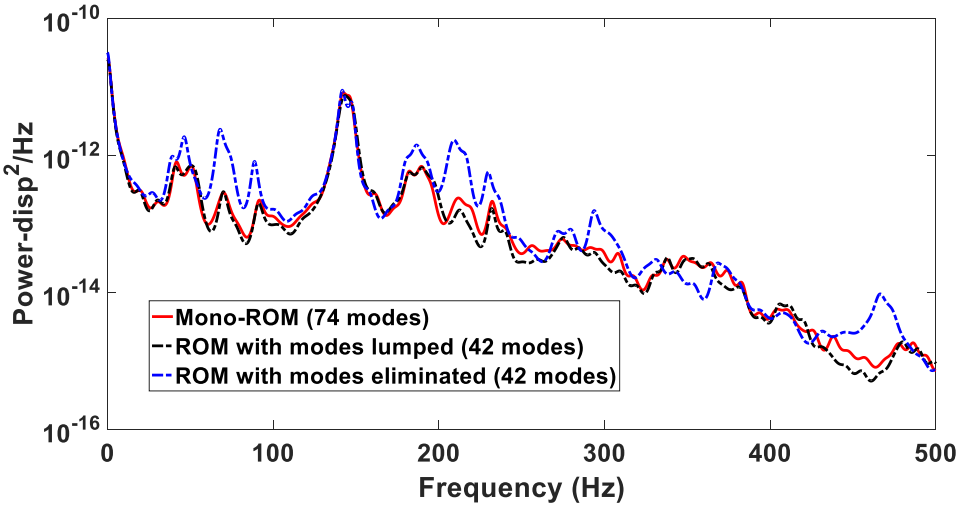

Figure 120 Power spectral densities of the in-plane (T2) responses of Panel 7 center for OASPL of 136dB obtained with the 74-mode full ROM (red), the component-centric 42-mode ROM with 10 linear modes lumped (black), the 42-mode ROM with the same linear modes eliminated (blue)

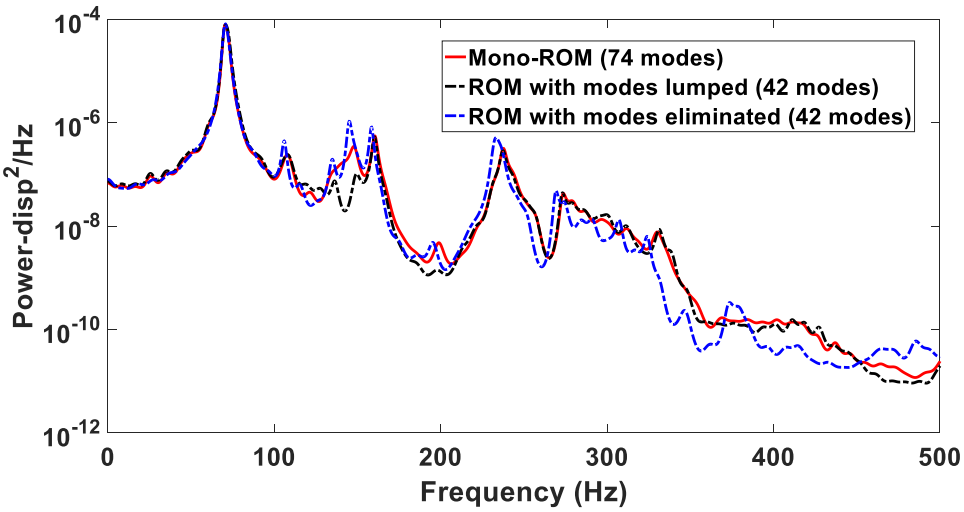

Figure 121 Power spectral densities of the transverse responses of Panel 8 center for OASPL of 136dB obtained with the 74-mode full ROM (red), the component-centric 42-mode ROM with 2 linear modes lumped (black), the 42-mode ROM with the same linear modes eliminated (blue)

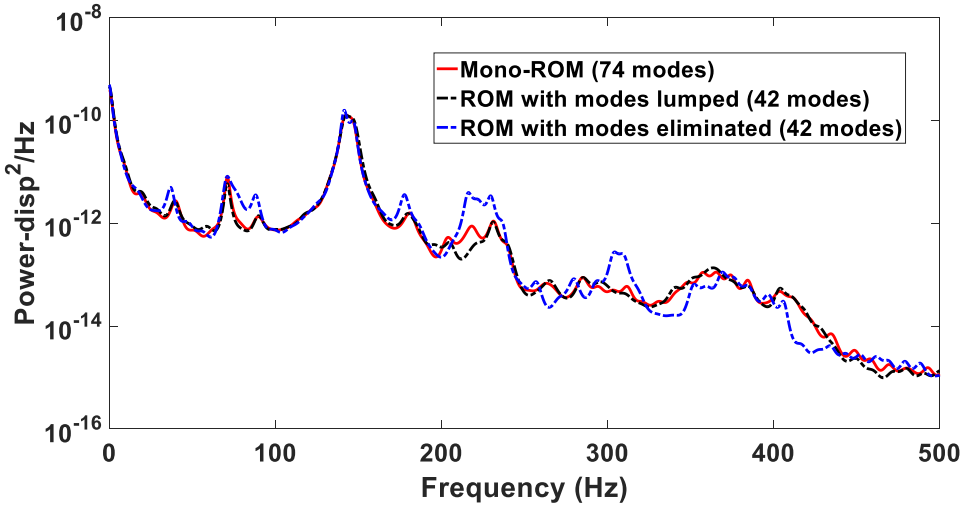

Figure 122 Power spectral densities of the in-plane (T2) responses of Panel 8 center for OASPL of 136dB obtained with the 74-mode full ROM (red), the component-centric 42-mode ROM with 2 linear modes lumped (black), the 42-mode ROM with the same linear modes eliminated (blue)

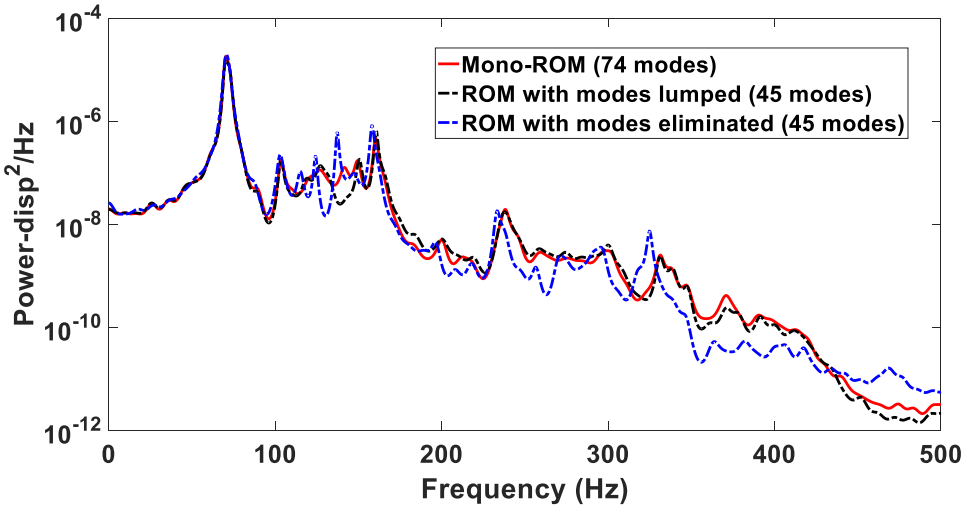

Figure 123 Power spectral densities of the transverse responses of Panel 9 center for OASPL of 136dB obtained with the 74-mode full ROM (red), the component-centric 45-mode ROM with 11 linear modes lumped (black), the 45-mode ROM with the same linear modes eliminated (blue)

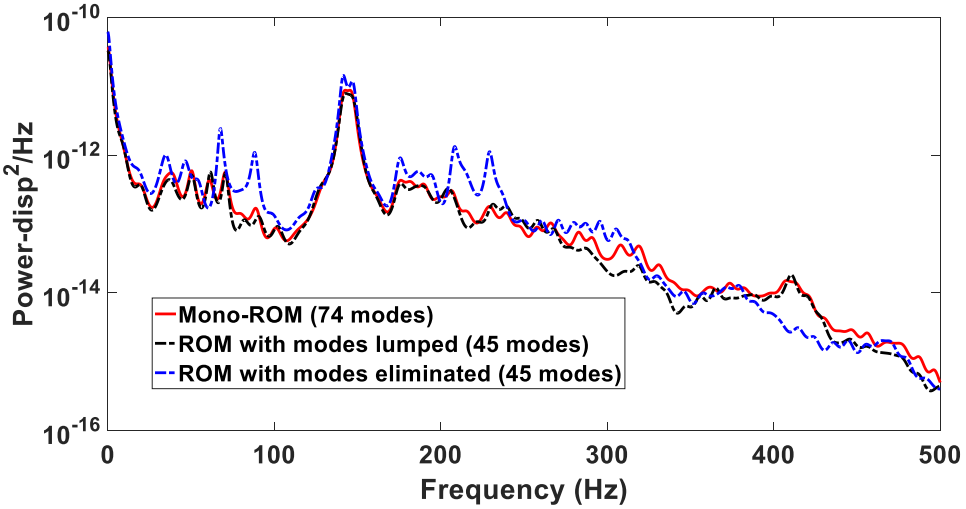

Figure 124 Power spectral densities of the in-plane (T2) responses of Panel 9 center for OASPL of 136dB obtained with the 74-mode full ROM (red), the component-centric 45-mode ROM with 11 linear modes lumped (black), the 45-mode ROM with the same linear modes eliminated (blue)

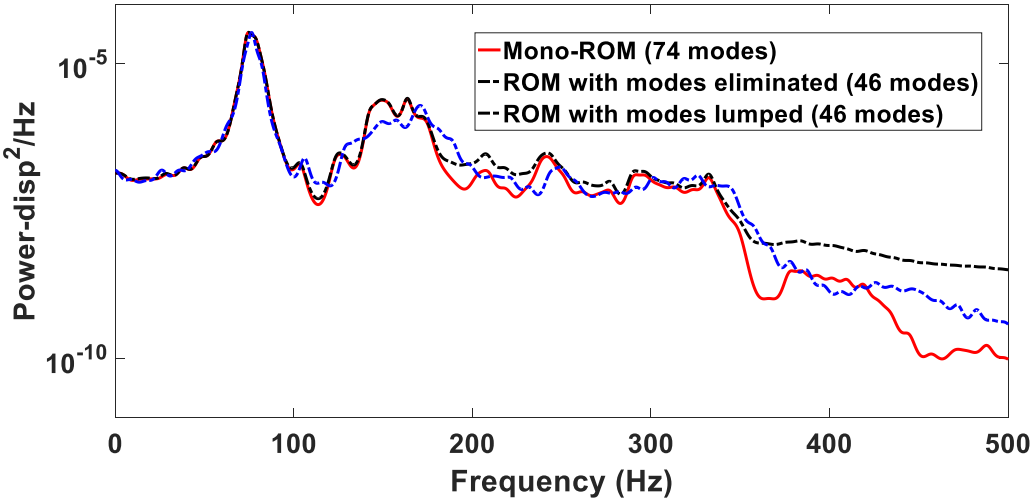

Figure 125 Power spectral densities of the transverse responses of Panel 1 center for OASPL of 144dB obtained with the 74-mode full ROM (red), the component-centric 46-mode ROM with 7 linear modes lumped (black), the 46-mode ROM with the same linear modes eliminated (blue)

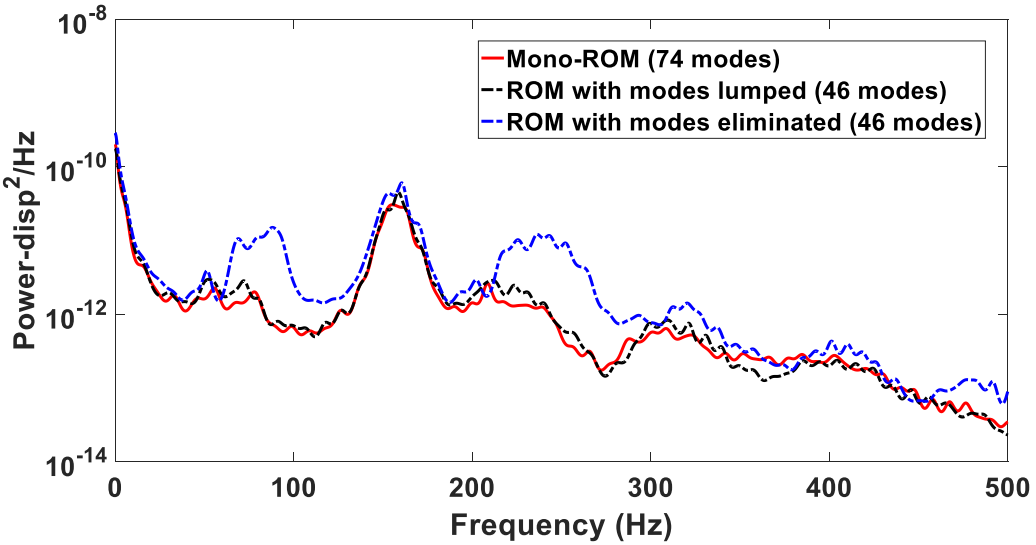

Figure 126 Power spectral densities of the in-plane (T2) responses of Panel 1 center for OASPL of 144dB obtained with the 74-mode full ROM (red), the component-centric 46-mode ROM with 7 linear modes lumped (black), the 46-mode ROM with the same linear modes eliminated (blue)

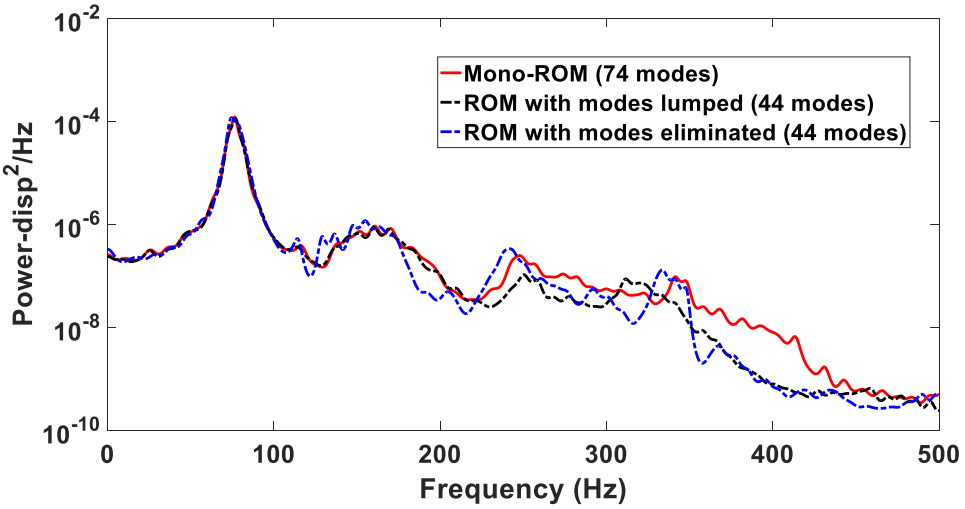

Figure 127 Power spectral densities of the transverse responses of Panel 2 center for OASPL of 144dB obtained with the 74-mode full ROM (red), the component-centric 44-mode ROM with 6 linear modes lumped (black), the 44-mode ROM with the same linear modes eliminated (blue)

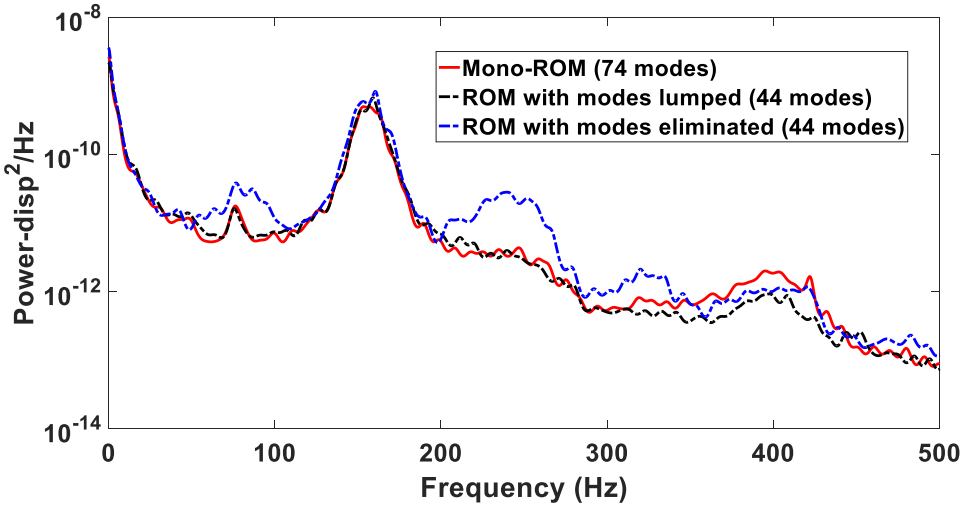

Figure 128 Power spectral densities of the in-plane (T2) responses of Panel 2 center for OASPL of 144dB obtained with the 74-mode full ROM (red), the component-centric 44-mode ROM with 6 linear modes lumped (black), the 44-mode ROM with the same linear modes eliminated (blue)

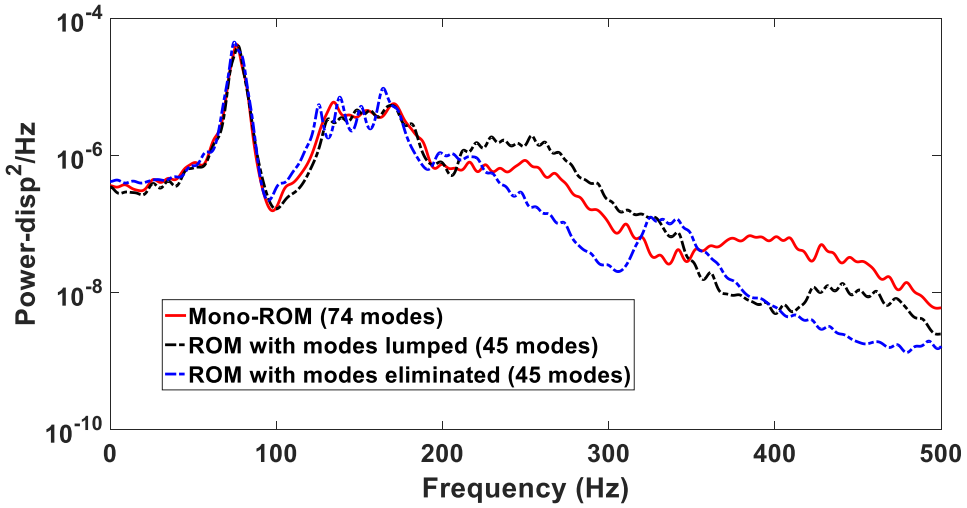

Figure 129 Power spectral densities of the transverse responses of Panel 3 center for OASPL of 144dB obtained with the 74-mode full ROM (red), the component-centric 45-mode ROM with 12 linear modes lumped (black), the 45-mode ROM with the same linear modes eliminated (blue)

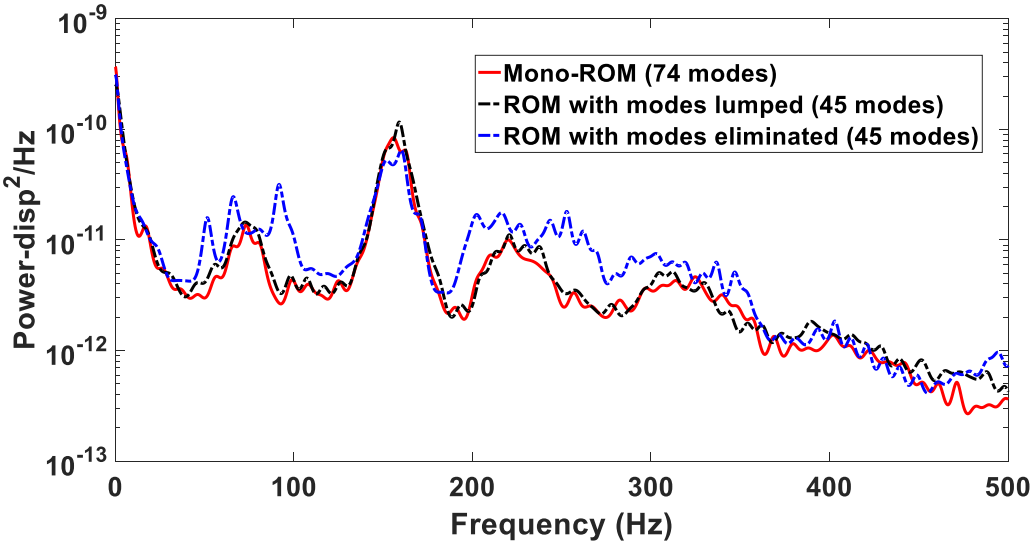

Figure 130 Power spectral densities of the in-plane (T2) responses of Panel 3 center for OASPL of 144dB obtained with the 74-mode full ROM (red), the component-centric 45-mode ROM with 12 linear modes lumped (black), the 45-mode ROM with the same linear modes eliminated (blue)

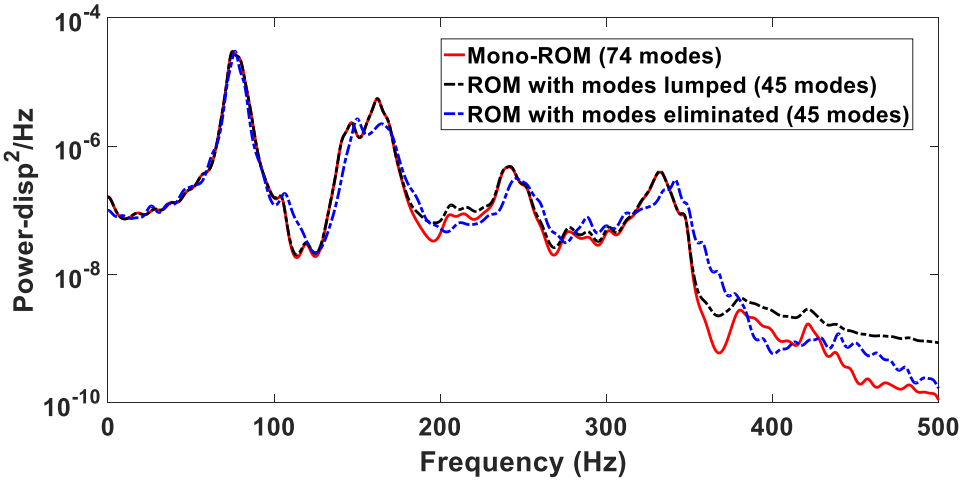

Figure 131 Power spectral densities of the transverse responses of Panel 4 center for OASPL of 144dB obtained with the 74-mode full ROM (red), the component-centric 45-mode ROM with 4 linear modes lumped (black), the 45-mode ROM with the same linear modes eliminated (blue)

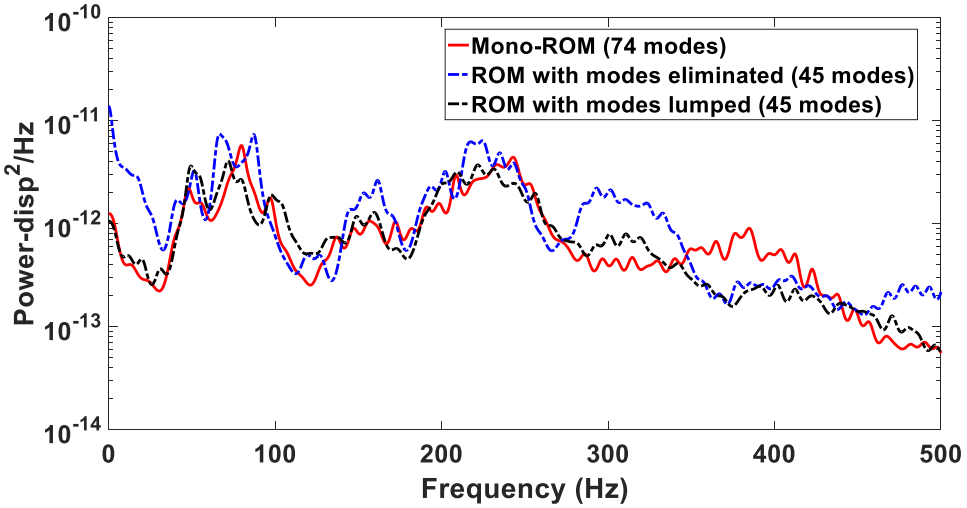

Figure 132 Power spectral densities of the in-plane (T2) responses of Panel 4 center for OASPL of 144dB obtained with the 74-mode full ROM (red), the component-centric 45-mode ROM with 4 linear modes lumped (black), the 45-mode ROM with the same linear modes eliminated (blue)

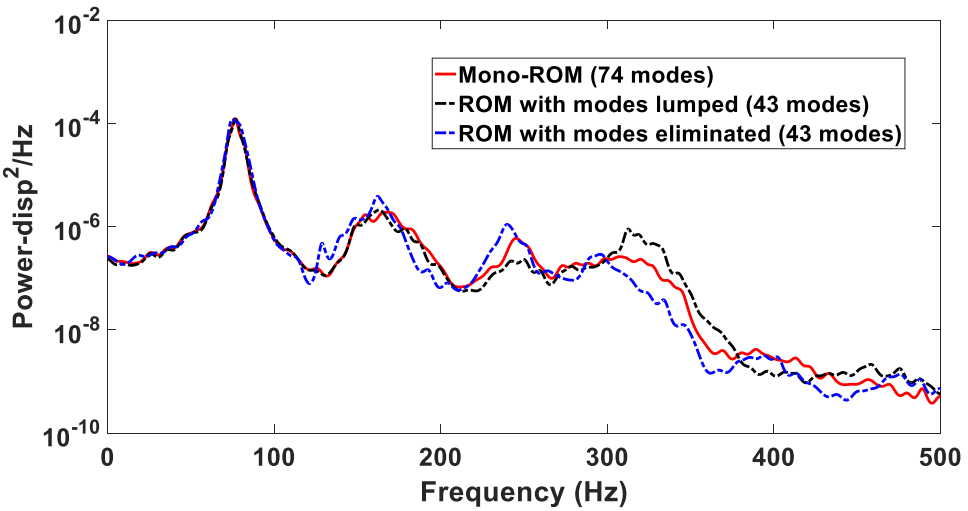

Figure 133 Power spectral densities of the transverse responses of Panel 5 center for OASPL of 144dB obtained with the 74-mode full ROM (red), the component-centric 43-mode ROM with 13 linear modes lumped (black), the 43-mode ROM with the same linear modes eliminated (blue)

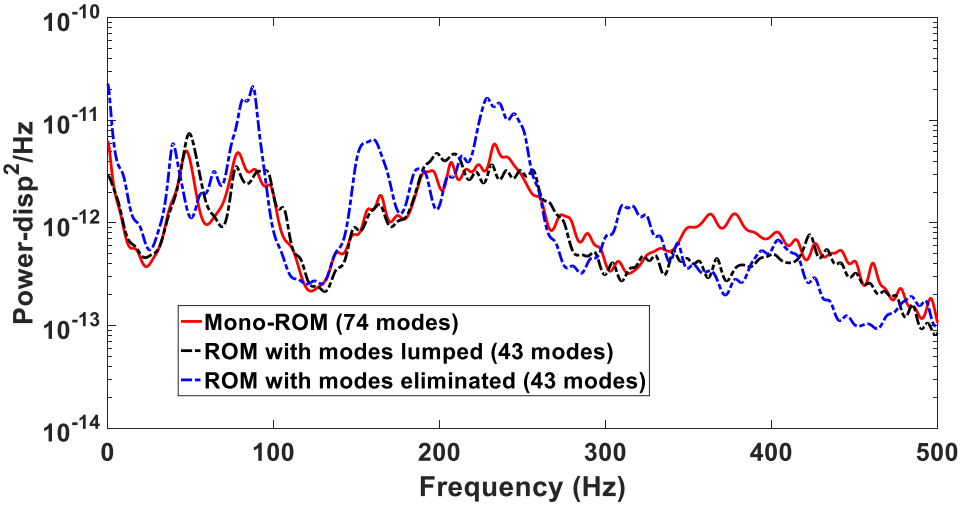

Figure 134 Power spectral densities of the in-plane (T2) responses of Panel 5 center for OASPL of 144dB obtained with the 74-mode full ROM (red), the component-centric 43-mode ROM with 13 linear modes lumped (black), the 43-mode ROM with the same linear modes eliminated (blue)

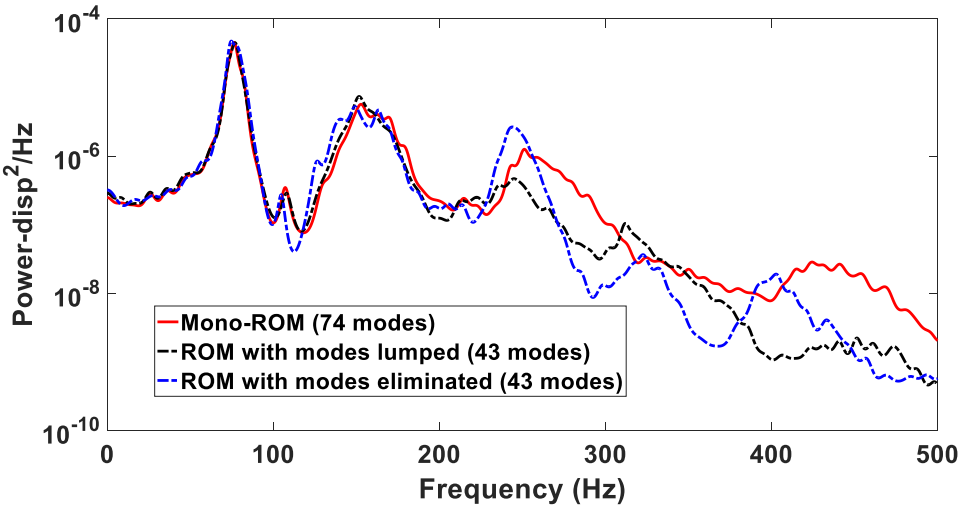

Figure 135 Power spectral densities of the transverse responses of Panel 6 center for OASPL of 144dB obtained with the 74-mode full ROM (red), the component-centric 43-mode ROM with 17 linear modes lumped (black), the 43-mode ROM with the same linear modes eliminated (blue)

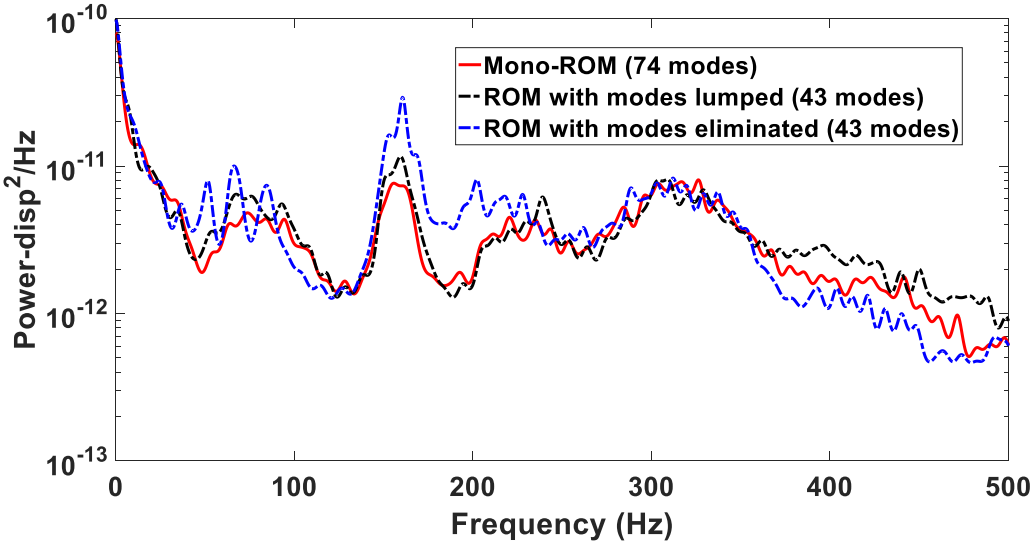

Figure 136 Power spectral densities of the in-plane (T2) responses of Panel 6 center for OASPL of 144dB obtained with the 74-mode full ROM (red), the component-centric 43-mode ROM with 17 linear modes lumped (black), the 43-mode ROM with the same linear modes eliminated (blue)

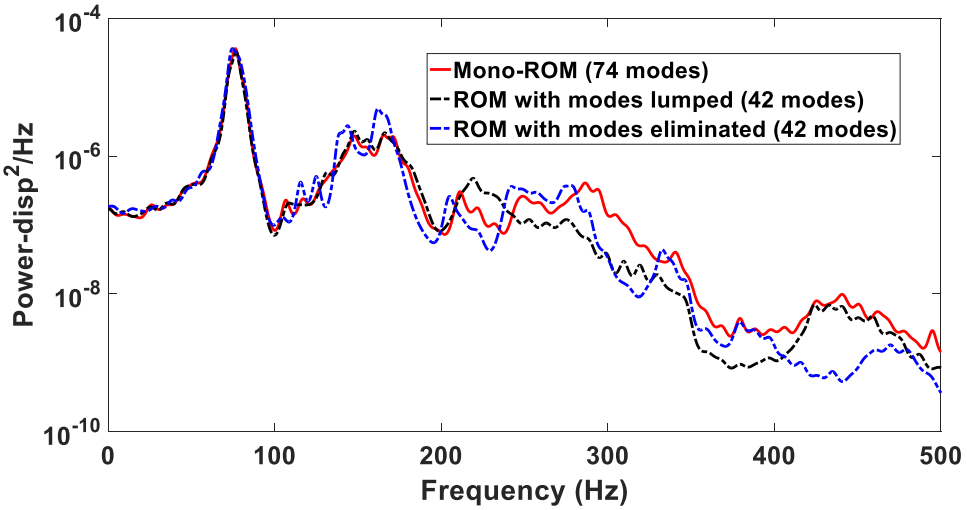

Figure 137 Power spectral densities of the transverse responses of Panel 7 center for OASPL of 144dB obtained with the 74-mode full ROM (red), the component-centric 42-mode ROM with 10 linear modes lumped (black), the 42-mode ROM with the same linear modes eliminated (blue)

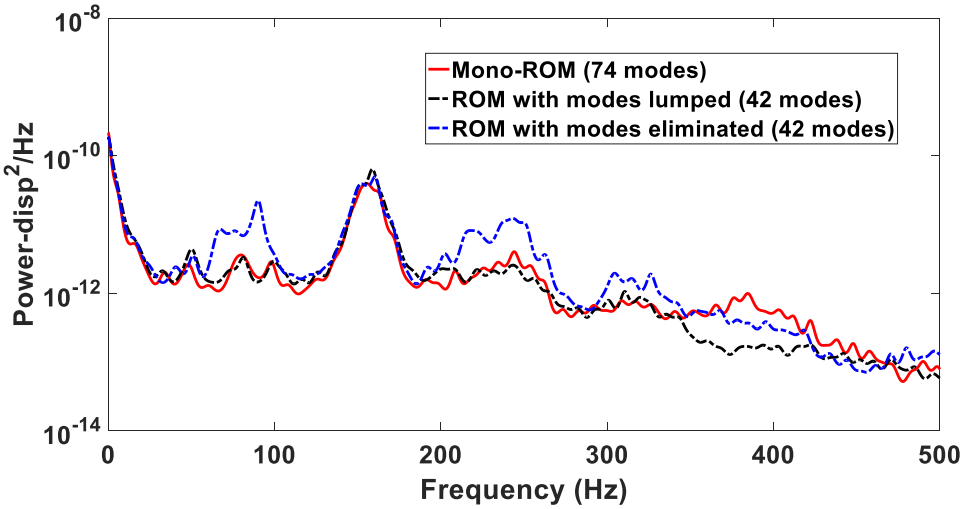

Figure 138 Power spectral densities of the in-plane (T2) responses of Panel 7 center for OASPL of 144dB obtained with the 74-mode full ROM (red), the component-centric 42-mode ROM with 10 linear modes lumped (black), the 42-mode ROM with the same linear modes eliminated (blue)

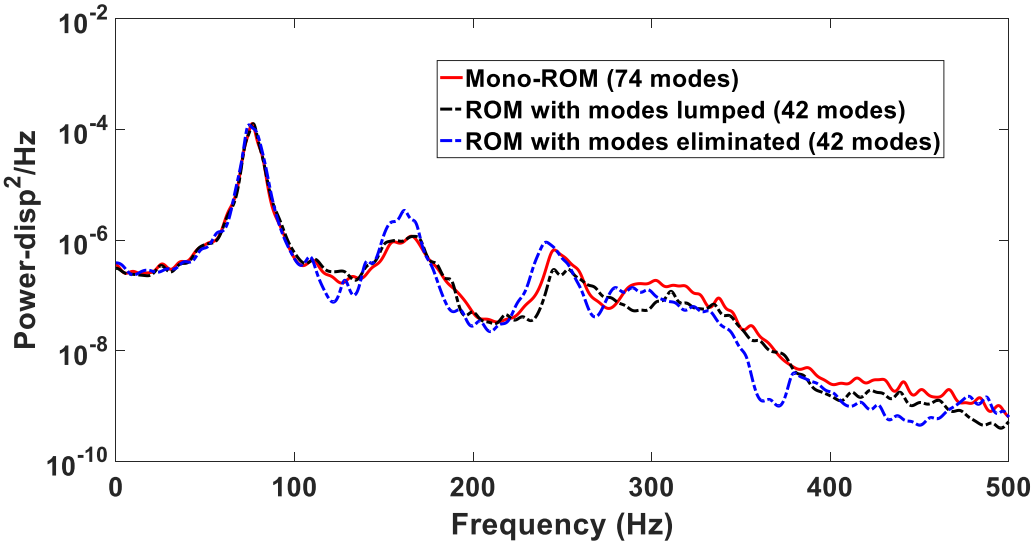

Figure 139 Power spectral densities of the transverse responses of Panel 8 center for OASPL of 144dB obtained with the 74-mode full ROM (red), the component-centric 42-mode ROM with 2 linear modes lumped (black), the 42-mode ROM with the same linear modes eliminated (blue)

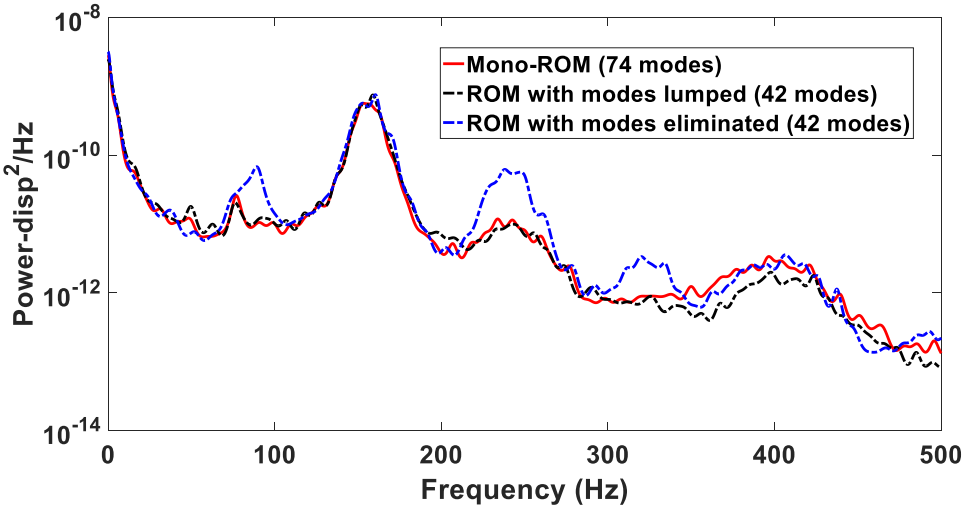

Figure 140 Power spectral densities of the in-plane (T2) responses of Panel 8 center for OASPL of 144dB obtained with the 74-mode full ROM (red), the component-centric 42-mode ROM with 2 linear modes lumped (black), the 42-mode ROM with the same linear modes eliminated (blue)

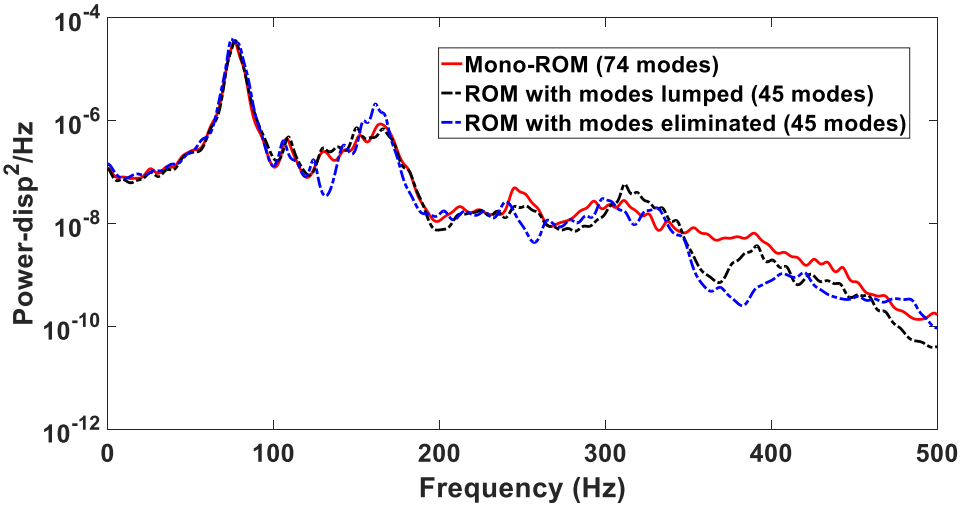

Figure 141 Power spectral densities of the transverse responses of Panel 9 center for OASPL of 144dB obtained with the 74-mode full ROM (red), the component-centric 45-mode ROM with 11 linear modes lumped (black), the 45-mode ROM with the same linear modes eliminated (blue)

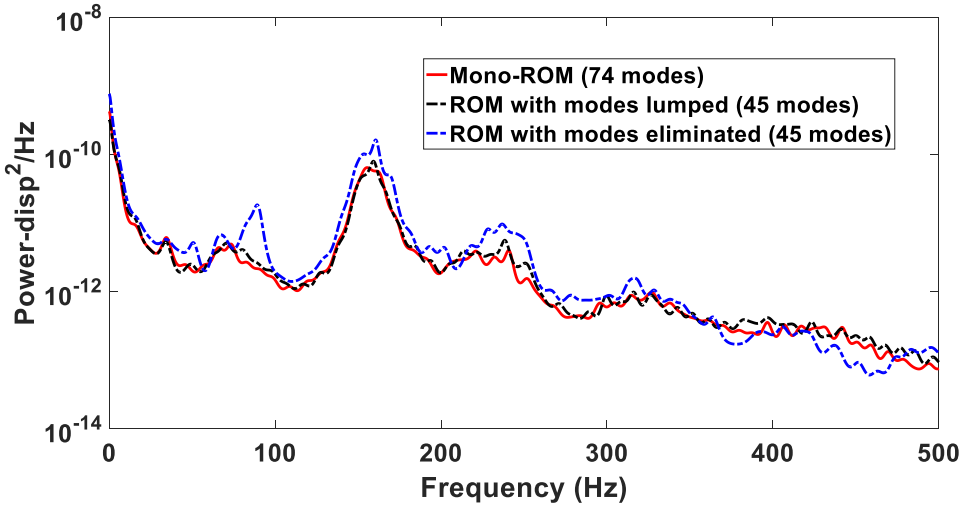

Figure 142 Power spectral densities of the in-plane (T2) responses of Panel 9 center for OASPL of 144dB obtained with the 74-mode full ROM (red), the component-centric 45-mode ROM with 11 linear modes lumped (black), the 45-mode ROM with the same linear modes eliminated (blue)

5.4 Computational Benefits

Consistently with the findings of the linear component-centric ROM investigation, their nonlinear counterparts are also much more compact than the full ROM for all choices of the component β. The reduction of the number of modes observed for all the bays, see Table 8, is about 40%. This reduction is potentially quite valuable for linear structures but it has a much larger impact for the nonlinear geometric ROMs considered here. A fair computational cost associated with ROMs should not only consider the time saving when solving the reduced system, but also the time spent on the identifying its linear, quadratic, and cubic stiffness coefficients. Denoting by N the number of modes, the former cost is proportional to the number of coefficients, i.e., approximately $N^4/6$ while the latter cost is as small as $N^2/6$ when using the tangent stiffness approach. These costs are shown in the last three columns of Table 8. These numbers clearly demonstrate the advantages of reducing the number of modes present in the model, even at the cost of some preliminary computations, i.e., those involved in the mode selection and the modal lumping processes, especially when parallel computations can be carried out to identify

and run the component-centric nonlinear geometric ROMs. A further reduction of the computational cost could potentially be achieved by performing a "lumping" of the dual modes and this issue will be addressed in the future.

Table 9

Computational Cost Estimates for Nonlinear Geometric ROMs of the Various Bays

ROM	Optimal # of modes (N)	Nonlinear ROM running cost ($\sim N^4/6$)	Nonlinear ROM identification cost ($\sim N^2/6$)
1	46	15%	39%
2	44	13%	35%
3	45	14%	37%
4	45	14%	37%
5	43	11%	34%
6	43	11%	34%
7	42	10%	32%
8	42	10%	32%
9	45	14%	37%
Mono-ROM	74	4,997,762 (100%)	913 (100%)

CHAPTER 6

SUMMARY

This thesis focused on developing “compact” (i.e., with small number of modes) ROMs that provide an accurate prediction of the response for part of the structure considered without focusing on the rest of it, referred to as component-centric ROMs. Four strategies were presented and discussed in the linear case. The first two approaches are both based on the CB substructuring technique and start with a set of modes for the component of interest (referred to as the β component). The response in the rest of the structure (referred to as the α component) induced by these modes is then determined and optimally represented using a POD strategy. The main difference between the two approaches is the set of modes used for the β component. The first approach relies as usual on the fixed interface modes of the β component while the second one adopts POD modes computed from the deflections in the β component of the linear modes in the frequency band of interest. These first two methods are effectively basis reductions techniques of the CB basis. On the test structure considered, a sizable 9-bay panel model, these methods were found to lead to accurate representations of the responses of the various bays with ROM but with sizes only slightly, 20%-25%, smaller than the number of linear modes present in the frequency band of interest. An approach based on the “global + local” method was also adopted to generate the “global” modes by “smoothing”/ “averaging” the mass property over α and β comp., respectively, to extract a “coarse” model of α and β and compute the “local” modes orthogonal to the “global” modes to add back necessary “information” for β. Even though it generally agrees with the prediction of the linear mode basis and provides better results under certain conditions, the modal reduction is not significant.

This observation led to the consideration of a fourth approach which starts from the linear modes of the structure, reducing first this set to those dominant in the β component response (the "selected modes") and then "lumping" the contributions of other modes to the ones of the dominant modes of close frequencies and similar mode shapes in the β component. This process leads to an increased accuracy for a given ROM number of modes and/or permits a decrease of this number for a given accuracy. Three variations of this modal lumping strategy were discussed and compared with the last one, the autoregressive modeling based method, providing the best compromise between computational cost and accuracy of predictions. The application of the modal lumping approaches to the various bays of the 9-bay panel led to ROM sizes equal at most to 40% of the number of linear modes of the structure in the frequency band, a potentially worthwhile saving. This reduction in ROM size is a benefit even if the response of the entire structure is required. Indeed, by modeling each critical component of the structure in turn, a single large ROM for the entire structure can be replaced by multiple smaller component-centric ROMs, which are perfectly suited to run in parallel. The computational benefits can thus be measured by the computational effort required for the most complex component. Besides, a good robustness of the ROM to changes in the β component properties (e.g., for design optimization) was demonstrated and a similar sensitivity analysis was carried out with respect to the loading under which the ROM is constructed – all of which support the usefulness of the proposed component-centric ROMs.

It was noted that the reduced ROM sizes would be particularly important for the nonlinear geometric ROMs developed within the last decade. Therefore, this approach was extended to the nonlinear geometric setting. The lumping approach followed in the linear case was recast as a rotation of the modal basis to achieve unobservable modes. In

the linear case, these modes then completely disappear from the formulation owing to the orthogonality of all modes involved. In the nonlinear case, however, the generalized coordinates of these modes are still present in the nonlinear stiffness terms of the observable modes. To remedy this issue, a “closure”-type scheme was proposed which relates linearly the generalized coordinates of the modes involved in the lumping. This final assumption permits to completely eliminate the unobserved generalized coordinates from the problem concluding the reduction of the basis. This was first demonstrated on a simple beam model and then applied to various bays of the complex 9-bay panel model considered in the linear case. This effort allowed a reduction by 40% of the number of basis functions to be considered in these nonlinear component-centric ROM as compared to a model approximating the entire structure *without any observable drop in accuracy*.

Seeking to reduce further the number of modes, one of the related future work would be to adopt the static condensation method to eliminate the “in-plane” modes from the basis, for flat structures. Moreover, while this thesis has been mainly focused on structural ROM with “zero” temperature loadings, it would be interesting to develop “multi-fidelity” structural ROMs with some thermal loadings. Along that thought, one may envision the development of “multi-fidelity” thermal ROMs under similar ideas.

REFERENCES

[1] B. Zuchowski, “Predictive capability for hypersonic structural response and life prediction, phase 1-identification of knowledge gaps,” *Aug*, 2010.

[2]B. Zuchowski, H. Shelby, J. Macguire, and P. McAuliffe, “Investigation of shortfalls in hypersonic vehicle structure combined environment analysis capability,” in *52nd AIAA/ASME/ASCE/AHS/ASC Structures, Structural Dynamics and Materials Conference 19th AIAA/ASME/AHS Adaptive Structures Conference 13t*, 2011, p. 2013.

[3]B. Zuchowski, “Predictive capability for hypersonic structural response and life prediction: phase ii detailed design of hypersonic cruise vehicle hot-structure,” *Lockheed Martin Aeronautics Company Final Report, AFRL-RQ-WP-TR-2012-0280*, 2012.

[4] M. J. Patil, D. H. Hodges, and C. E. S. Cesnik, “Nonlinear aeroelasticity and flight dynamics of high-altitude long-endurance aircraft,” *Journal of Aircraft*, vol. 38, no. 1, pp. 88–94, 2001.

[5]R. Levy and W. R. Spillers, *Analysis of geometrically nonlinear structures*. Springer Science & Business Media, 2013.

[6] R. D. Blevins, I. Holehouse, and K. R. Wentz, “Thermoacoustic loads and fatigue of hypersonic vehicle skin panels,” *Journal of aircraft*, vol. 30, no. 6, pp. 971–978, 1993.

[7]R. D. Blevins, D. Bofilios, I. Holehouse, V. W. Hwa, M. D. Tratt, A. L. Laganelli, P. Pozefsky, and M. Pierucci, “Thermo-vibro-acoustic loads and fatigue of hypersonic flight vehicle structure,” DTIC Document, Tech. Rep., 2009.

[8] T. G. Eason and S. Spottswood, “A structures perspective on the challenges associated with analyzing a reusable hypersonic platform,” in *54th AIAA/ASME/ASCE/AHS/ASC Structures, Structural Dynamics, and Materials Conference*, 2013, p. 1747.

[9] R. Bisplinghoff, “Some structural and aeroelastic considerations of high-speed flight the nineteenth wright brothers lecture,” *Journal of the Aeronautical Sciences*, vol. 23, no. 4, pp. 289–321, 1956.

[10] I. Garrick, “A survey of aerothermoelasticity,” 1963.

[11] A. J. Culler and J. J. McNamara, “Studies on fluid-thermal-structural coupling for aerothermoelasticity in hypersonic flow,” *AIAA journal*, vol. 48, no. 8, pp. 1721–1738, 2010.

[12] A. J. Culler and J. J. McNamara, “Impact of fluid-thermal-structural coupling on response prediction of hypersonic skin panels,” *AIAA journal*, vol. 49, no. 11, pp. 2393–2406, 2011.

[13] B. A. Miller, J. J. McNamara, S. Spottswood, and A. Culler, “The impact of flow induced loads on snap-through behavior of acoustically excited, thermally buckled panels,” *Journal of sound and vibration*, vol. 330, no. 23, pp. 5736–5752, 2011.

[14] J. Hollkamp and R. Gordon, “Modeling membrane displacements in the sonic fatigue response prediction problem,” in *46th AIAA/ASME/ASCE/AHS/ASC Structures, Structural Dynamics and Materials Conference*, 2005, p. 2095.

[15] B. L. Clarkson, “Review of sonic fatigue technology,” 1994.

[16] N. F. Rieger, “Relationship between finite element analysis and modal analysis.” *Sound & Vibration*, vol. 20, no. 1, pp. 16–31, 1986.

[17] B. Salimbahrami and B. Lohmann, “Order reduction of large scale second-order systems using krylov subspace methods,” *Linear Algebra and its Applications*, vol. 415, no. 2-3, pp. 385–405, 2006.

[18] P. Tiso and E. Jansen, “A finite element based reduction method for nonlinear dynamics of structures,” in *46th AIAA/ASME/ASCE/AHS/ASC Structures, Structural Dynamics and Materials Conference*, 2005, p. 1867.

[19] C. Nowakowski, J. Fehr, M. Fischer, and P. Eberhard, “Model order reduction in elastic multibody systems using the floating frame of reference formulation,” *IFAC Proceedings Volumes*, vol. 45, no. 2, pp. 40–48, 2012.

[20]C. Farhat, P. Avery, T. Chapman, and J. Cortial, “Dimensional reduction of nonlinear finite element dynamic models with finite rotations and energy-based mesh sampling and weighting for computational efficiency,” *International Journal for Numerical Methods in Engineering*, vol. 98, no. 9, pp. 625–662, 2014.

[21] D. Amsallem, M. J. Zahr, and C. Farhat, “Nonlinear model order reduction based on local reduced-order bases,” *International Journal for Numerical Methods in Engineering*, vol. 92, no. 10, pp. 891–916, 2012.

[22]R. Perez, X. Wang, and M. P. Mignolet, “Nonintrusive structural dynamic reduced order modeling for large deformations: enhancements for complex structures,” *Journal of Computational and Nonlinear Dynamics*, vol. 9, no. 3, p. 031008, 2014.

[23]X. Wang, R. A. Perez, and M. P. Mignolet, “Nonlinear reduced order modeling of complex wing models,” in *54th AIAA/ASME/ASCE/AHS/ASC Structures, Structural Dynamics, and Materials Conference*, 2013, p. 1520.

[24]R. A. Perez, B. P. Smarslok, and M. P. Mignolet, “Deterministic and stochastic partial linearization approach for nonlinear reduced order models of structures,” in *56th AIAA/ASCE/AHS/ASC Structures, Structural Dynamics, and Materials Conference*, 2015, p. 2052.

[25] A. Przekop and S. A. Rizzi, "Nonlinear reduced order random response analysis of structures with shallow curvature," *AIAA journal*, vol. 44, no. 8, pp. 1767–1778, 2006.

[26] A. A. Muravyov and S. A. Rizzi, "Determination of nonlinear stiffness with application to random vibration of geometrically nonlinear structures," *Computers & Structures*, vol. 81, no. 15, pp. 1513–1523, 2003.

[27] S. Spottswood and R. Allemang, "On the investigation of some parameter identification and experimental modal filtering issues for nonlinear reduced order models," *Experimental mechanics*, vol. 47, no. 4, pp. 511–521, 2007.

[28] J. J. Hollkamp, R. W. Gordon, and S. M. Spottswood, "Nonlinear modal models for sonic fatigue response prediction: a comparison of methods," *Journal of Sound and Vibration*, vol. 284, no. 3, pp. 1145–1163, 2005.

[29] R. W. Gordon and J. J. Hollkamp, "Reduced-order models for acoustic response prediction," DTIC Document, Tech. Rep., 2011.

[30] S. Spottswood, J. Hollkamp, and T. Eason, "On the use of reduced-order models for a shallow curved beam under combined loading," in *49th AIAA/ASME/ASCE/AHS/ASC Structures, Structural Dynamics, and Materials Conference, 16th AIAA/ASME/AHS Adaptive Structures Conference, 10th AIAA Non-Deterministic Approaches Conference, 9th AIAA Gossamer Spacecraft Forum, 4th AIAA Multidisciplinary Design Optimization Specialists Conference*, 2008, p. 2235.

[31] K. Kim, V. Khanna, X. Wang, and M. Mignolet, "Nonlinear reduced order modeling of flat cantilevered structures," in *50th AIAA/ASME/ASCE/AHS/ASC Structures, Structural Dynamics, and Materials Conference 17th AIAA/ASME/AHS Adaptive Structures Conference 11th AIAA No*, 2009, p. 2492.

[32] M. P. Mignolet, A. Przekop, S. A. Rizzi, and S. M. Spottswood, "A review of indirect/non-intrusive reduced order modeling of nonlinear geometric structures," *Journal of Sound and Vibration*, vol. 332, no. 10, pp. 2437–2460, 2013.

[33] X. Wang, M. Mignolet, T. Eason, and S. Spottswood, "Nonlinear reduced order modeling of curved beams: a comparison of methods," in *50th AIAA/ASME/ASCE/AHS/ASC Structures, Structural Dynamics, and Materials Conference 17th AIAA/ASME/AHS Adaptive Structures Conference 11th AIAA No*, 2009, p. 2433.

[34] K. Kim, A. G. Radu, X. Wang, and M. P. Mignolet, "Nonlinear reduced order modeling of isotropic and functionally graded plates," *International Journal of Non-Linear Mechanics*, vol. 49, pp. 100–110, 2013.

[35] W. C. Hurty, “Dynamic analysis of structural systems using component modes,” *AIAA journal*, vol. 3, no. 4, pp. 678–685, 1965.

[36] M. C. Bampton and R. R. CRAIG, JR, “Coupling of substructures for dynamic analyses.” *Aiaa Journal*, vol. 6, no. 7, pp. 1313–1319, 1968.

[37] M. P. Castanier, Y.-C. Tan, and C. Pierre, “Characteristic constraint modes for component mode synthesis,” *AIAA journal*, vol. 39, no. 6, pp. 1182–1187, 2001.

[38] R. CRAIG, JR, “On the use of attachment modes in substructure coupling for dynamic analysis,” in *18th Structural Dynamics and Materials Conference*, 1977, p. 405.

[39] R. H. MacNeal, “A hybrid method of component mode synthesis,” *Computers & Structures*, vol. 1, no. 4, pp. 581–601, 1971.

[40] E. Budak and H. N. Özgüven, “Iterative receptance method for determining harmonic response of structures with symmetrical non-linearities,” *Mechanical Systems and Signal Processing*, vol. 7, no. 1, pp. 75–87, 1993.

[41] F. Wenneker and P. Tiso, “A substructuring method for geometrically nonlinear structures,” in *Dynamics of Coupled Structures, Volume 1*. Springer, 2014, pp. 157–165.

[42] R. A. Perez, *Multiscale reduced order models for the geometrically nonlinear response of complex structures*, 2012.

[43] R. J. Kuether, M. S. Allen, and J. J. Hollkamp, “Modal substructuring of geometrically nonlinear finite-element models,” *AIAA Journal*, vol. 54, no. 2, pp. 691–702, 2015.

[44] R. D. Buehrle, G. A. Fleming, R. S. Pappa, and F. W. Grosveld, “Finite element model development for aircraft fuselage structures,” 2000.

[45] P. Dumir and A. Bhaskar, “Some erroneous finite element formulations of non-linear vibrations of beams and plates,” *Journal of sound and vibration*, vol. 123, no. 3, pp. 517–527, 1988.

[46] R. Wiebe, “Nonlinear dynamics of discrete and continuous mechanical systems with snap-through instabilities,” Ph.D. dissertation, Duke University, 2012.

[47] S.-K. Hong, B. I. Epureanu, and M. P. Castanier, “Next-generation parametric reduced-order models,” *Mechanical Systems and Signal Processing*, vol. 37, no. 1, pp. 403–421, 2013.

[48] G. Kerschen, J.-c. Golinval, A. F. Vakakis, and L. A. Bergman, “The method of proper orthogonal decomposition for dynamical characterization and order reduction of

mechanical systems: an overview," *Nonlinear dynamics*, vol. 41, no. 1, pp. 147–169, 2005.

[49] C. Soize and A. Batou, "Stochastic reduced-order model in low-frequency dynamics in presence of numerous local elastic modes," *Journal of Applied Mechanics*, vol. 78, no. 6, p. 061003, 2011.

[50] I. Bucher and S. Braun, "Left eigenvectors: extraction from measurements and physical interpretation," *Journal of applied mechanics*, vol. 64, no. 1, pp. 97–105, 1997.

[51] P. C. Hansen, "The truncatedsvd as a method for regularization," *BIT Numerical Mathematics*, vol. 27, no. 4, pp. 534–553, 1987.

[52] S. L. Marple, *Digital spectral analysis: with applications*. Prentice-Hall Englewood Cliffs, NJ, 1987, vol. 5.

[53] W. Gersch and J. Yonemoto, "Synthesis of multivariate random vibration systems: a two-stage least squares ar-ma model approach," *Journal of Sound and Vibration*, vol. 52, no. 4, pp. 553–565, 1977.

[54] M. Mignolet and J. Red-Horse, "Armax identification of vibrating structures-model and model order estimation," in *35th Structures, Structural Dynamics, and Materials Conference*, 1994, p. 1525.